ERCOFTAC Special Interest Group on "Dispersed Turbulent Multi-Phase Flow"

Best Practice Guidelines

Editors:

Martin Sommerfeld
Berend van Wachem
René Oliemans

Version 20-08-2007

Contents:

1 Introduction

This Best Practice Guideline on Computational Multiphase Dynamics for turbulent dispersed multiphase flows is a follow-up of the previous ERCOFTAC Best Practice Guidelines for Industrial CFD and should be used in combination with it. The potential users are Master/PhD students from Academia who are embarking on a project on CFD of (wall-bounded) turbulent dispersed multiphase flows and engineers in industry, using CFD codes for design and de-bottle necking of multiphase flow equipment.

Engineers in industry have the option of using RANS or LES as turbulence models, and an Euler/Euler or Euler/Lagrange approach. They are interested in the size distribution of the dispersed phase and the dispersion of particles in the complex turbulent flow field as function of space and time. They use the CFD code as a subroutine for their design parameter and scale-up studies, so the code should be fast and reliable. The Master/PhD students at Universities tend to use more sophisticated turbulence models (DNS and LES) for idealized flow geometries (homogeneous turbulence, channel flow, free jets, etc.) with point particles and detailed models to study the behaviour of isolated or a restricted number of particles (Interface tracking, Level set, VOF).

Ideally the newcomer in industry should obtain insight into the technique of performing the computations and the degree of sophistication required for his problem. For example if one wants to establish for a Stirred Tank Reactor design the positioning of the stirrers on the shaft a RANS model is adequate for the turbulence; if, however, one wants to know the variation of turbulence intensity to determine the size distribution of drops injected one should use at least LES for such a complex turbulent flow field.

So, this Best Practice Guideline has the aim of serving both stakeholders by supplying information on the methods that are available and their possibilities and limitations. Before embarking on the complexity of having to deal with multiphase flows the user should ensure that solutions are provided for grids and time steps, which are fine enough so that numerical errors are minimized. For the multiphase flow applications one has to realize that the spatial and temporal distribution of the dispersed phase may require local grid refinements to achieve accurate solutions.

This document starts by addressing in chapter 2, entitled Fundamentals, the classification of multiphase flows and of dispersed flows in particular. Here an important distinction is that between the dilute flows, with a small number of particles present in the turbulent flow field and the dense dispersed multiphase flows, commonly encountered in industrial applications. For the latter one will have to account for turbulence modulation due to the presence of the particles (two-way coupling) and particle collisions. Chapter 3 can be used to define the forces on bubbles, drops and particles to be accounted for in practical applications. Chapter 4 gives a survey of the Computational Multiphase Fluid Dynamics methods for turbulent dispersed flows. It ranges from very refined models to study the detailed flow around particles with sophisticated turbulence models to the Euler/Euler RANS methods that are very popular to perform industrial multiphase flow calculations with a great number of particles with a broad range of sizes flowing in a turbulent flow field in a complex geometry. Chapter 5 addresses particle-wall and inter-particle collisions and heat and mass transfer for droplets and sprays as specific phenomena and modelling approaches. Sources of errors are listed in chapter 6. Industrial examples for multiphase flows for which successful simulations have been performed are given in chapter 7. The document concludes with a checklist of Best Practice Advice, suggestions for future developments and references to the relevant literature.

An issue not treated explicitly is model validation. This certainly is very important, and should be a key element in the selection of proper models for the simulation of a practical multiphase flow situation. Of course the validation ought to be a necessary activity of the developers of commercial codes. It is recommended to use the ERCOFTAC data base on multiphase flow benchmarks, established over the years at workshops organized by ERCOFTAC's Special Interest Group on Dispersed Turbulent Two-Phase Flow for validation purposes (see www.ercoftac.org). Also the Best Practice Guidelines for CFD Code validation for Reactor-Safety Applications (Menter, 2002) is highly recommended and considered useful for other applications as well.

2 Fundamentals

The simultaneous presence of several different phases in external or internal flows such as gas, liquid and solid is found in daily life, environment and numerous industrial processes. These types of flows are termed multiphase flows, which may exist in different forms depending on the phase distribution. Examples are gas-liquid transportation, crude oil recovery, spray cans, sediment transport in rivers, pollutant transport in the atmosphere, cloud formation, fuel injection in engines, bubble column reactors and spray driers for food processing, to name only a few. This demonstrates the great importance of multiphase flows, which might occur even more frequently than single phase flows. As a result of the interaction between the different phases such flows are rather complicated and very difficult to describe theoretically. For the design and optimisation of such multiphase systems a detailed understanding of the interfacial transport phenomena is essential. For single-phase flows computational fluid dynamics (CFD) has already a long history and it is nowadays standard in the development of airplanes and cars using different commercially available CFD-tools.

Due to the complex physics involved in multiphase flow the application of CFD in this area is rather young (probably 20 – 30 years). The different methods being used for the numerical calculation of multiphase flows will be summarised below. This chapter is devoted to the classification of multiphase flows and their characterisation by integral properties.

2.1 Classification of Multi-Phase Flows

Multiphase flows may be encountered in various forms in industrial practice (see Figure 2.1), as for example, transient flows with a transition from pure liquid to a vapour flow as a result of external heating (e.g. heat pipe), separated flows (i.e. stratified flows, slug flows, or film flows), and dispersed two-phase flows where one phase is present in the form of particles, droplets, or bubbles dispersed in a continuous carrier phase (i.e. gas or liquid). In all these different types of multiphase flows also different interfacial transport mechanisms are relevant. Consequently also different numerical approaches have to be applied. Transient multiphase flows may be found in steam generators of boilers, where the heat addition results in the formation of dispersed bubbles that further grow in size and also will coalescence yielding large vapour slugs. Further evaporation results in annular two-phase flow with small droplets being dispersed in the core of the pipe. Stratified and slug flows are for example found in transportation pipes for crude oil recovery, where the observed flow regime also depends on the orientation of the pipeline, e.g. horizontal, vertical or inclined.

Dispersed two-phase flows are encountered in numerous technical and industrial processes, as for example in particle technology (i.e. production and transportation of solid particles), chemical engineering, and biotechnology. Dispersed two-phase flows may be classified in terms of the different phases being present as summarised in Table 2.1 together with some of the most important industrial processes.

Commonly dispersed two-phase flows are separated in two flow regimes. In dilute dispersed systems the spacing between the particles is rather large, so that a direct interaction between the particles is rare and fluid dynamic forces are governing particle transport. On the other hand dense dispersed systems are those where the inter-particle spacing is comparatively low (i.e. smaller than about 10 particle diameters). Under such conditions the transport of the particles is dominated by collisions between them as for example in a fluidised bed.

Additionally, numerous processes may involve more than two phases (i.e. multiphase flows),

as for example in a spray scrubber where droplets and solid particles are dispersed in a gas flow and the aim is to collect the particles by the droplets. Another example is a bubble column reactor with catalyst particles.

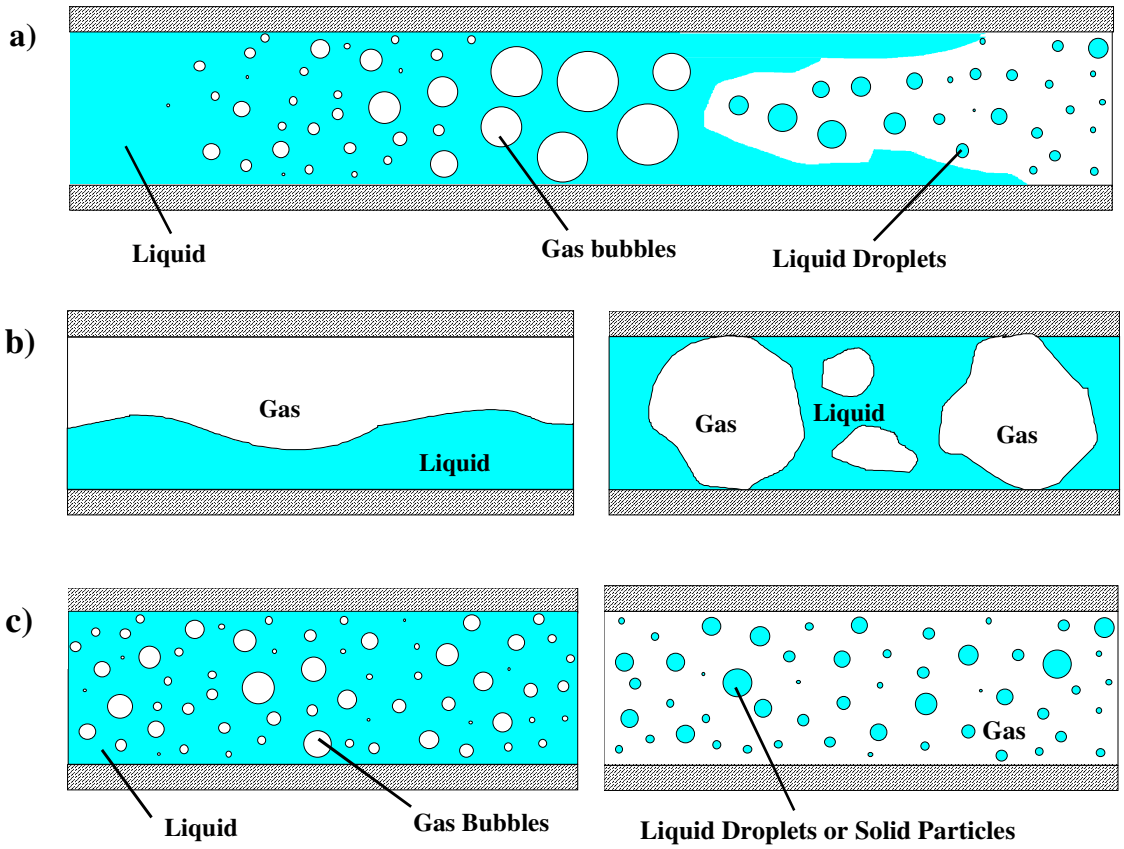

Figure 2.1: Different regimes of two-phase flows, a) transient two-phase flow, b) separated two-phase flow, c) dispersed two-phase flow.

Continuous/Dispersed Phase	industrial/technical application
Gas-solid flows	pneumatic conveying, particle separation in cyclones and filters, fluidised beds
Liquid-solid flows	hydraulic conveying, liquid-solid separation, particle dispersion in stirred vessels
Gas-droplet flows	spray drying, spray cooling, spray painting, spray scrubbers
Liquid-droplet flows	mixing of immiscible liquids, liquid-liquid extraction
Liquid-gas flows	bubble columns, aeration of sewage water, flotation

Table 2.1: Summary of two-phase flow systems and important industrial and technical processes.

2.2 Integral characterization of Multi-Phase Flows

For the characterisation of dispersed two-phase flows different integral properties are used, which are briefly summarised below. The volume fraction of the dispersed phase is the volume occupied by the particles in a unit volume. Hence this property is given by:

$$\alpha_P = \frac{\sum_i N_i \, V_{Pi}}{V}, \tag{1}$$

where N_i is the number of all particles in the size fraction i, having the particle volume $V_{pi} = D_{pi}^3 \, \pi/6$. The particle diameter D_{pi} in this context is the volume-equivalent diameter of a sphere. In case multiple phases are present one can define a volume fraction for each phase. Since the sum of the volume fraction of the dispersed phases and the continuous phase is unity, the continuous phase volume fraction is:

$$\alpha_F = \left(1 - \sum_n \alpha_{P,n} \right). \tag{2}$$

The bulk density or concentration of the dispersed phase is the mass of particles per unit volume and hence given by:

$$\rho_P^b = c_P = \alpha_P \, \rho_P. \tag{3}$$

Correspondingly, the bulk density of the continuous phase is:

$$\rho_F^b = \left(1 - \alpha_P\right) \rho_F. \tag{4}$$

The sum of both bulk densities is called mixture density:

$$\rho_m = \rho_F^b + \rho_P^b = \left(1 - \alpha_P\right) \rho_F + \alpha_P \, \rho_P. \tag{5}$$

Often the particle concentration is also expressed by the number of particles per unit volume, as for example in clean-room technology:

$$n_P = \frac{N_P}{V}. \tag{6}$$

Especially in gas-solid flows for example in pneumatic conveying the mass loading is frequently used, which is defined as the total mass flux of the dispersed phase to that of the fluid:

$$\eta = \frac{\alpha_P \, \rho_P \, U_P}{\left(1 - \alpha_P\right) \rho_F \, U_F}. \tag{7}$$

The mass flux is also quite often used and is defined as the mass of particles flowing through a unit area per unit time. It should be noted that the mass flux is a vector quantity (i.e. a mass flux can be defined for each velocity direction), which also can be defined as a local property. The proximity of particles in a two-phase flow system may be estimated from the inter-particle spacing, which however can be only determined for regular arrangements of the particles. For a cubic arrangement the inter-particle spacing, i.e. the distance between the centres of particles, is obtained from:

$$\frac{L}{D_P} = \left(\frac{\pi}{6\,\alpha_P} \right)^{1/3} . \tag{8}$$

For a volume fraction of 1 % the spacing is 3.74 diameters and for 10 % only 1.74. Hence, for such high volume fractions the particles cannot be treated to move isolated, since fluid dynamic interactions become of importance. In many practical fluid-particle systems however, the particle volume fraction is much lower. Consider for example a gas-solid flow (particle density ρ_p = 2500 kg/m^3, gas density of ρ_F = 1.18 kg/m^3) with a mass loading of one (i.e. η = 1) and assume no slip between the phases, then the volume fraction is about 0.05 % (i.e. $\alpha_p = 5 \cdot 10^{-4}$). This results in an inter-particle spacing of about 10 particle diameters, hence, under such a condition a fluid dynamic interaction may be neglected. In industrial bubble columns the gas volume fraction can have values of 40 % or even more. This yields an inter-bubble spacing of 1.1 bubble diameters. This will result in such a highly turbulent flow in a large collision rate and hence bubble coalescence will occur.

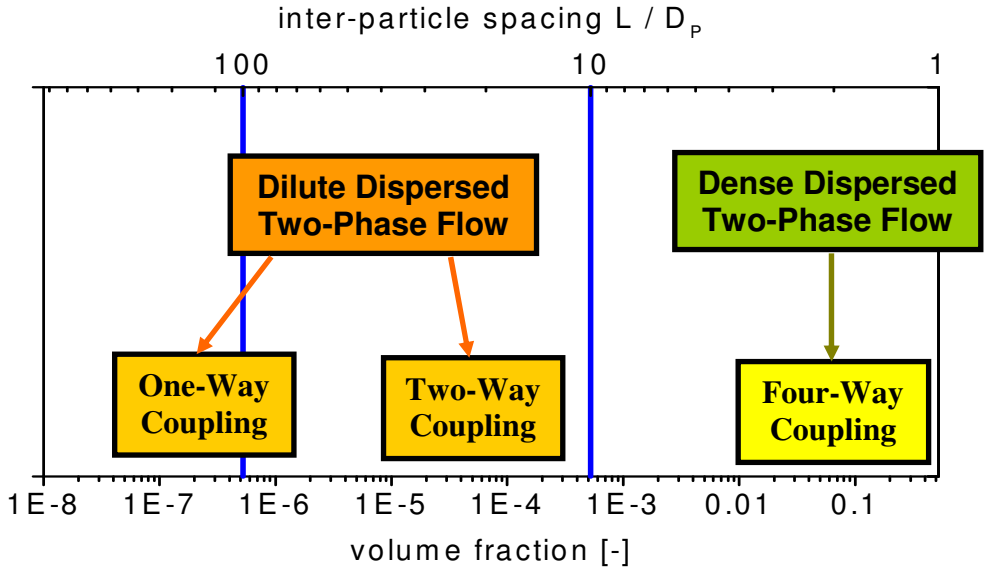

Figure 2.2: Regimes of dispersed two-phase flows as a function of particle volume fraction.

A classification of dispersed two-phase flows with regard to the importance of interaction mechanisms was provided by Elghobashi (1994). Generally it is distinguished between dilute and dense two-phase flows as mentioned above (Figure 2.2). A two-phase system may be regarded as dilute for volume fractions up to $\alpha_p = 10^{-3}$ (i.e. $L/D_p \approx 8$). In this regime the influence of the particle phase on the fluid flow may be neglected for $\alpha_p < 10^{-6}$ (i.e. $L/D_p \approx 80$). For higher volume fractions the influence of the particles on the fluid flow, which is often referred to as two-way coupling, needs to be accounted for. In the dense regime (i.e. for $\alpha_p > 10^{-3}$) additionally inter-particle interactions (i.e. collisions and fluid dynamic interactions between particles) become of importance. Hence, this regime is characterised by the so-called four-way coupling. Another interpretation for the separation between dilute and dense two-phase flow, which also accounts for particle inertia, will be introduced in chapter 5.2, when discussing the importance of inter-particle collisions.

3 Forces acting on particles, droplets and bubbles

The motion of particles in fluids is described in a Lagrangian way by solving a set of ordinary differential equations along the trajectory in order to calculate the change of particle location and the linear as well as angular components of the particle velocity. This requires the consideration of all relevant forces acting on the particle. The equation of motion for small particles in a viscous quiescent fluid (i.e. for small particle Reynolds-numbers, which is also referred to as Stokes flow) goes back to the pioneering work of Basset (1988), Boussinesq (1985) and Oseen (1927). Therefore, the equation of motion is mostly referred to as BBO-equation. Numerous publications deal with the extension of the BBO equation for turbulent flows. The thesis of Tchen (1949) was probably the first study on particle motion in turbulent flows based on the BBO equation. A rigorous derivation of the equation of motion for small particles in non-uniform flow has been performed by Maxey and Riley (1983). Neglecting the Faxen terms (for details see Crowe et al. 1998) the equation proposed by Maxey and Riley (1983) for small particle Reynolds numbers is as follows:

$$m_P \frac{d\,\vec{u}_P}{d\,t} = \frac{18\,\mu_F}{\rho_P\ D_P^2}\ m_P\ \left(\vec{u}_F - \vec{u}_P\right)\ -\ m_F \frac{D\,\vec{u}_F}{D\,t} + 0.5\,m_F \left(\frac{D\,\vec{u}_F}{D\,t} - \frac{d\,\vec{u}_P}{d\,t}\right) + 9\sqrt{\frac{\rho_F\ \mu_F}{\pi}}\ \frac{m_P}{\rho_P\ D_P}\ \int_0^t \frac{\frac{D\,\vec{u}_F}{D\,\tau} - \frac{d\,\vec{u}_P}{d\,\tau}}{\left(t-\tau\right)^{1/2}} d\,\tau + \left(m_P - m_F\right)\vec{g}. \tag{9}$$

In the following section a possible extension of the BBO-equation for higher particle Reynolds numbers will be introduced. In addition other forces which might be relevant for certain conditions, such as for example transverse lift forces, will be introduced and their relevance will be analysed. Considering spherical particles and neglecting heat and mass transfer phenomena, the calculation of particle trajectories requires the solution of three ordinary differential equations when particle rotation is accounted for. Hence, the differential equations for calculating the particle location and the linear and angular velocities in vector form are given by:

$$\frac{d\,\vec{x}_p}{dt} = \vec{u}_p, \tag{10}$$

$$m_p \frac{d\,\vec{u}_p}{dt} = \sum \vec{F}_i, \tag{11}$$

$$I_p \frac{d\,\vec{\omega}_p}{dt} = \vec{T}, \tag{12}$$

where $m_p = \rho_p\ D_p^3 \pi / 6$ is the particle mass, $I_p = 0.1\,m_p\ D_p^2$ is the moment of inertia for a sphere, $\vec{F}_i$ represents the different relevant forces acting on the particle, and $\vec{T}$ is the torque acting on a rotating particle due to the viscous interaction with the fluid.

Analytical solutions for the different forces and the torque only are available for small particle Reynolds numbers (i.e. Stokes regime). An extension to higher Reynolds numbers is generally obtained by including a coefficient *C* in front of the force, where *C* is typically based on empirical correlations, which are derived form experiments.

3.1 Drag force

In most fluid-particle systems the drag force is dominating the particle motion and consists of a friction and form drag. The extension of the drag force to higher particle Reynolds numbers is based on the introduction of a drag coefficient C_D being defined as:

$$C_D = \frac{F_D}{\frac{\rho_F}{2}\left(\vec{u}_F - \vec{u}_P\right)^2 A_P}, \tag{13}$$

where $A_P = \pi / 4\, D_P^2$ is the cross-section of a spherical particle. The drag force is then expressed by:

$$\vec{F}_D = \frac{3}{4}\,\frac{\rho_F\ m_P}{\rho_P\ D_P}\ c_D\left(\vec{u}_F - \vec{u}_P\right)\ \left|\vec{u}_F - \vec{u}_P\right|. \tag{14}$$

The drag coefficient is given as a function of the particle Reynolds number (defined as the ratio of inertial force to friction force):

$$\mathrm{Re}_P = \frac{\rho_F\ D_P\left(\vec{u}_F - \vec{u}_P\right)}{\mu_F}. \tag{15}$$

The dependence of the drag coefficient of a sphere (spherical particle) on the Reynolds number is shown in Figure 3.1 based on numerous experimental investigations (Schlichting 1965). From this dependence one may identify several regimes which are associated with the flow characteristics around the sphere:

For small Reynolds numbers (i.e. $\mathrm{Re_p} < 0.5$) viscous effects are dominating and no separation is observed. Therefore, an analytic solution for the drag coefficient is possible as proposed by Stokes (1851):

$$C_D = \frac{24}{\mathrm{Re}_p}. \tag{16}$$

This regime is often referred to as the Stokes-regime.

In the transition region (i.e. $0.5 < \mathrm{Re_p} < 1000$) inertial effects become of increasing importance. Above a Reynolds number of about 24 the flow around the particle begins to separate. Initially this separation is symmetric (Clift et al.1978). It becomes unstable and periodic above $\mathrm{Re_p} \approx 130$. For this non-linear regime numerous correlations have been proposed (Clift et al. 1978, Crowe et al. 1998) which fit the experimental data more or less accurate. A frequently used correlation is that proposed by Schiller & Naumann (1933), which fits the data up to $\mathrm{Re_p} = 1000$ reasonably well (see Figure 3.1).

$$C_D = \frac{24}{\mathrm{Re}_P}\left(1 + 0.15\,\mathrm{Re}_P^{0.687}\right) = \frac{24}{\mathrm{Re}_P} f_D. \tag{17}$$

Above $\mathrm{Re_p} \approx 1000$ the flow is fully turbulent and the drag coefficient remains almost constant up to the critical Reynolds number, since wake size and structure are not considerably

changing. This regime is referred to as Newton-regime with:

$$C_d \approx 0.44. \tag{18}$$

At the critical Reynolds number ($Re_{crit} \approx 2.5 \cdot 10^5$) a drastic decrease of the drag coefficient is observed, being caused by the transition from a laminar to a turbulent boundary layer around the particle. This results in a decrease of the particle wake size.

In the super-critical region (i.e. $Re_p > 4.0 \cdot 10^5$) the drag coefficient again increases continuously. For most practical particulate flows however this region is not relevant.

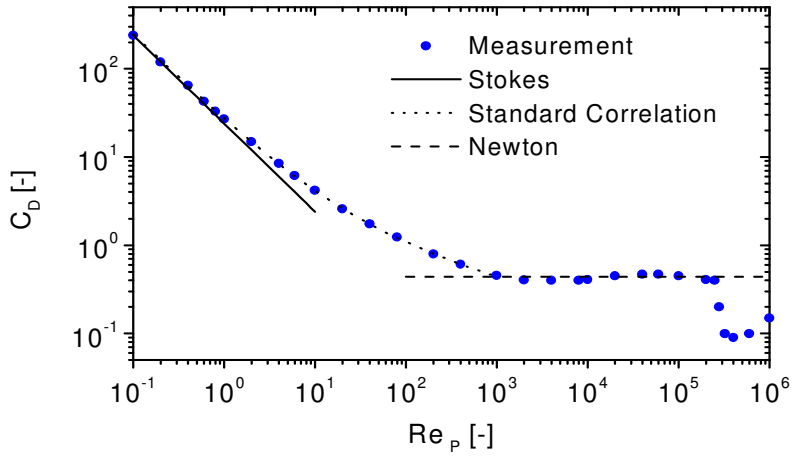

Figure 3.1: Drag coefficient as a function of particle Reynolds number. Comparison of experimental data with the correlation for the different regimes (The standard correlation corresponds to Eq. (17)).

The drag coefficient may be altered by numerous other physical effects, such as turbulence of the surrounding flow, surface roughness of the particle, particle shape, wall effects, compressibility of the fluid, rarefaction effects and particle concentration effects. All these effects can in general only be accounted for by empirical correction factors derived from detailed experiments.

The **turbulence level of the ambient flow** essentially causes a reduction of the critical Reynolds number as shown by Torobin and Gauvin (1961). With increasing turbulence intensity the transition from laminar to turbulent boundary layer is shifted towards smaller particle Reynolds numbers.

A **surface roughness** on a spherical particle also results in a reduction of the critical Reynolds number (Sawatzki 1961) since this is also associated with a modification of the boundary layer.

The consideration of the **particle shape** in the calculation of particle motion is rather difficult, since it requires the solution of additional ordinary differential equations for the particle orientation and a projection of the forces with regard to the relative motion. Such an approach was introduced by Rosendahl (1998). Most computations rely on the assumption of spherical particles. A simplified approach to consider a non-sphericity of particles may be based on the use of modified average drag coefficients, which are provided for different sphericities for example by Haider & Levenspiel (1989) and Thompson & Clark (1991). There is very little known about particle shape effects in the other forces, such as added mass and transverse lift forces.

The particle shape is important for the drag force and also for the transverse lift forces and the

moment exerted on a particle. Basically, the drag coefficient depends on the orientation of a non-spherical particle with respect to the instantaneous relative velocity vector. In order to account for the shape effect, this requires solving the particle orientation vector. In addition, data is required which describes the drag coefficient as a function of the particle orientation. Such data for the drag coefficient are very rare (Hölzer & Sommerfeld 2006). Regarding transverse lift forces almost no information is available on the particle shape effect.

For most practical computations, the calculation of the change in particle orientation is not, where the particles are considered as point-particles anyway. However, it is possible to approximately account for particle shape effects on the drag coefficient using the correlations proposed by, e.g. Haider and Levenspiel (1989) and Tompson and Clark (1991). These correlations were evaluated on the basis of numerous experimental data obtained for particles fixed in a wind tunnel or from sedimenting particles. Hence, the drag coefficient is obtained for a given particle orientation. This is also the case in a sedimentation analysis since the particles will sediment in a more or less stable orientation for which the drag coefficient is maximised, i.e. a disc will sediment horizontally aligned. The correlation proposed by Haider and Levenspiel (1989) has the form:

$$C_D = \frac{24}{\mathrm{Re}_P}\left(1 + A\,\mathrm{Re}_P^B\right) + \frac{C}{1 + \frac{D}{\mathrm{Re}_P}}. \tag{19}$$

The coefficients A to D are depending on the sphericity of the particle, which is defined as the ratio of the surface area of a volume equivalent sphere to the surface area of the considered non-spherical particle.

$$\phi = \frac{S_V}{S_{Partikel}}. \tag{20}$$

The correlation coefficients A to D are:

$$\begin{aligned} A &= \exp\left(2.3288 - 6.4581\,\phi + 2.4486\,\phi^2\right), \\ B &= 0.0964 + 0.5565\,\phi, \\ C &= \exp\left(4.905 - 13.8944\,\phi + 18.4222\,\phi^2 - 10.2599\,\phi^3\right), \\ D &= \exp\left(1.4681 + 12.2584\,\phi - 20.7322\,\phi^2 + 15.8855\,\phi^3\right). \end{aligned} \tag{21}$$

These correlations were obtained from experimental data for isometric non-spherical particles (i.e. cube octahedrons $\phi = 0.906$, octahedrons $\phi = 0.846$, cubes $\phi = 0.806$ and tetrahedrons $\phi = 0.67$) and disc-like particles with sphericities of $\phi = 0.026$, 0.043, 0.123 and 0.230. The resulting drag coefficient is plotted in Fig. 3.2 as a function of particle Reynolds number (defined with the volume equivalent diameter) with the sphericity as a parameter. This result reveals that the drag coefficient increases with decreasing sphericity. This increase is smaller in the Stokes regime compared to the Newton regime where the drag coefficient increases by several magnitudes. Moreover, the transition to the Newton regime (fully turbulent regime) is shifted to smaller particle Reynolds numbers with decreasing sphericity. Additionally, the width of the intermediate regime (i.e. between laminar and turbulent) is reduced. The concept of sphericity becomes meaningless when particles with rough surfaces are considered, whereby the sphericity approaches very small values. Therefore, also other parameters are

used for shape characterisation, such as aspect ratios, roundness and a hydrodynamic shape descriptor called scruple (Thomson and Clark, 1991). The drag correlation proposed by Ganser (1993) is based on using a Stokes- and Newton-shape factors which are combined with the particle Reynolds number to give a generalised parameter $\mathrm{Re}_p \cdot K_1 \cdot K_2$. Both shape descriptors are obtained as functions of the sphericity and the projected area in the direction of motion. Hence this correlation includes the influence of particle orientation with respect to the relative flow.

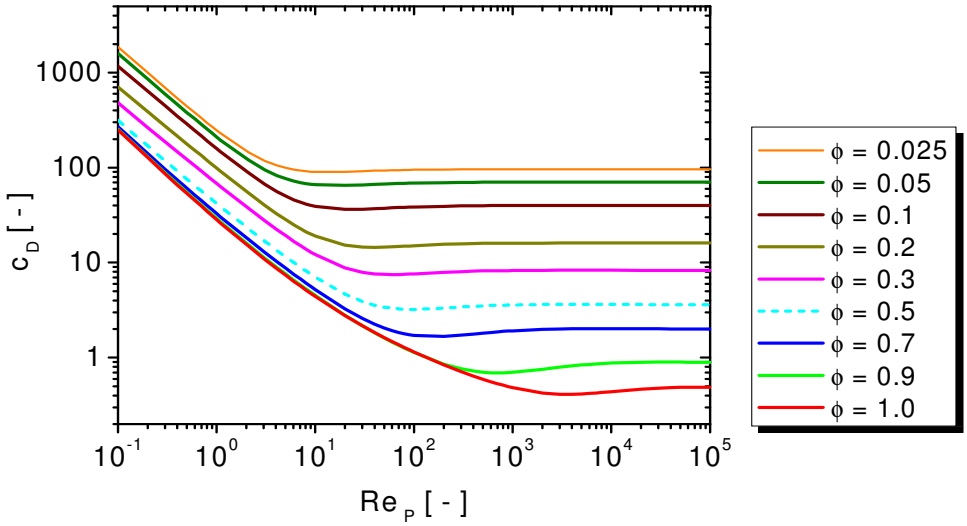

Figure 3.2: Drag coefficient of non-spherical particles as a function of particle Reynolds number with the sphericity as a parameter according to Eq.(19) (Haider and Levenspiel, 1989).

The **motion of particles in the vicinity of a rigid wall** results in an increase of the drag coefficient and is additionally associated with a transverse lift force. Analytic solutions for the wall effect are again only available for very small particle Reynolds numbers. The particle motion normal to a wall (Figure 3.3a) was for example considered by Brenner (1961) and a wall-parallel motion (Figure 3.3b) was analysed by Goldman et al. (1967). The first order solution for a particle moving towards a wall, which is valid for large distances from the wall, is given by (Brenner 1961):

$$\frac{C_D}{C_{D,Stokes}} \cong 1 + \frac{9}{8}\frac{R_P}{h}. \tag{22}$$

For a non-rotating particle moving parallel to a wall in a quiescent fluid the increase of the drag is predicted by an asymptotic solution proposed by Faxen (1923) for large distances from the wall:

$$\frac{C_D}{C_{D,Stokes}} = \left[1 - \frac{9}{16}\left(\frac{R_P}{h}\right) + \frac{1}{8}\left(\frac{R_P}{h}\right)^3 - \frac{45}{256}\left(\frac{R_P}{h}\right)^4 - \frac{1}{16}\left(\frac{R_P}{h}\right)^5\right]^{-1}. \tag{23}$$

The two results are shown in Figure 3.4 as a function of the normalised gap between particle and wall (i.e. a/R_P). For large wall distance the curves approach unity and a finite value is obtained for $a/R_P \rightarrow 0$. It should be noted that wall effects would be additionally affected by particle rotation and a shear flow in the vicinity of the wall Goldman et al. (1967).

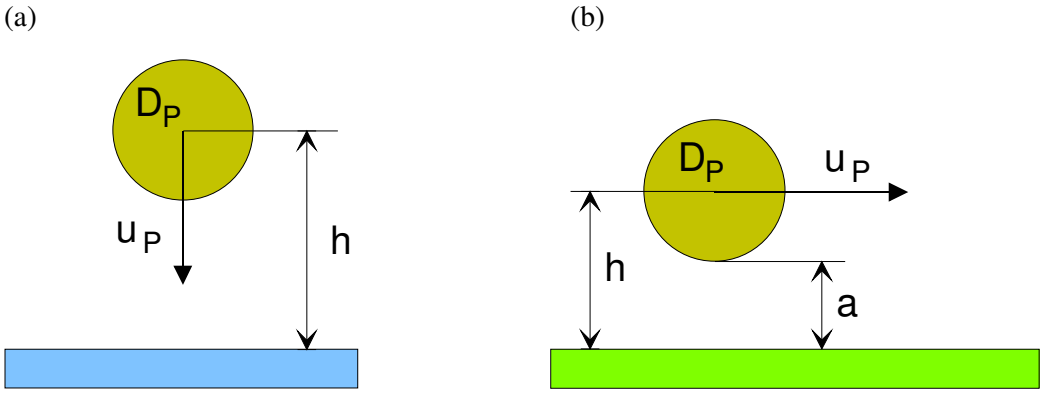

Figure 3.3: Illustration of wall effects, a) motion normal to a wall, b) motion parallel to a wall.

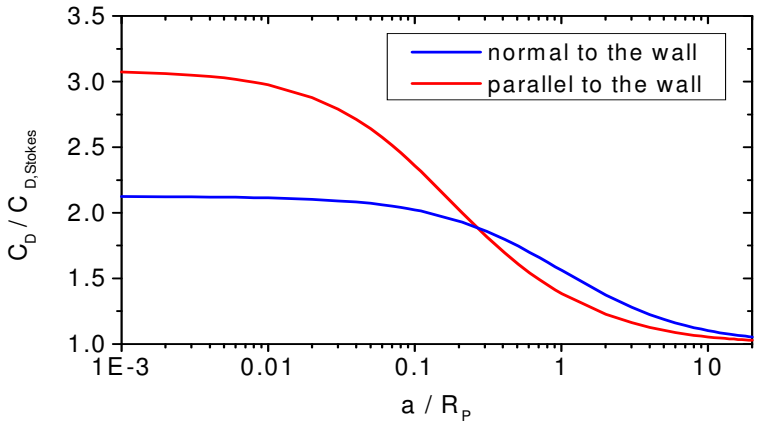

Figure 3.4: Modification of drag coefficient for a particle moving normal and parallel to a wall (Eqs. (22) and (23)).

Rarefaction effects become of importance in a low-pressure environment or when the particles are very small (e.g. nano-particles). In such a situation the gas flow around the particle cannot be regarded as a continuum, instead the particle motion is induced by collisions of gas molecules with the particle surface. This implies that the sticking condition at the particle surface is not anymore fulfilled. Rather, a partial or full slip is found at the surface. This results in a reduction of the drag coefficient. The importance of rarefaction effects may be estimated based on the ratio of the mean free path of the gas molecules to the particle diameter, which is the particle Knudsen number:

$$Kn_p = \frac{\lambda}{D_p}\sqrt{2}. \tag{24}$$

The mean free path of the gas molecules λ can be calculated according to kinetic theory of gases from:

$$\lambda = \frac{\mu_F}{0.499\,\overline{c_{Mol}}\,\rho_F}, \tag{25}$$

where $\overline{c_{Mol}}$ is the mean relative velocity between gas molecules given by:

$$\overline{c_{Mol}} = \left(\frac{8\ p}{\pi\ \rho_F} \right)^{1/2}, \tag{26}$$

and p is the pressure. For atmospheric conditions (i.e. p = 1.0 bar, T = 293 K) the mean free path is about 0.06 µm. A classification of the different flow regimes in rarefied conditions or for very small particles may be based on the Knudsen number and is summarised in Table 3.1. In the Stokes regime, which is generally valid for very small particles, the reduction of the drag coefficient may be accounted for by a correction function, the so-called Cunningham correlation, resulting in a modified drag (Davies 1945):

$$C_D = \frac{C_{D,Stokes}}{1 + Kn_P \left\{ 2.514 + 0.8\ \exp\left(-\frac{0.55}{Kn_P} \right) \right\}} = \frac{C_{D,Stokes}}{Cu}. \tag{27}$$

This correlation is valid for $0.1 < Kn_p < 1000$ and $Re_p < 0.25$ and is only applicable for low particle Mach numbers (definition see below). Therefore, it is often used in particle technology, as for example when considering the separation of fine particles from a gas stream.

Flow Regime	Range of Knudsen number
Continuum flow	$0 < Kn_P < 0.015$
Slip flow	$0.015 < Kn_P < 0.15$
Transition flow	$0.15 < Kn_P < 4.5$
Free molecular flow	$4.5 < Kn_P < \infty$

Table 3.1: Different regimes of rarefied flows with respect to particle motion.

The Cunningham correction, i.e. $1/Cu$, is plotted in Figure 3.5 as a function of the Knudsen number. It is obvious, that a considerable reduction of the drag coefficient occurs for $Kn_p >$ 0.012.

The **compressibility of the fluid** (i.e. relevant for gases as a continuum) becomes of importance when the relative velocity reaches values such that the particle Mach number increases beyond 0.3. In this situation compression waves or even shock waves (for $Ma_p > 1$) are initiated by the particle motion that causes an increase of the drag for large particle Reynolds numbers. The particle Mach number is defined as:

$$Ma_p = \frac{\left| \vec{u}_F - \vec{u}_P \right|}{a}, \tag{28}$$

where a is the speed of sound given by:

$$a = \sqrt{\gamma\, R\, T}. \tag{29}$$

In Eq. (29), γ is the ratio of the specific heat, R is the universal gas constant, and T the absolute temperature of the gas. Numerous correlations, which are mostly based on experimental studies, are proposed to account for compressibility effects, as for example the following expression proposed by Carlson and Hoglund (1964):

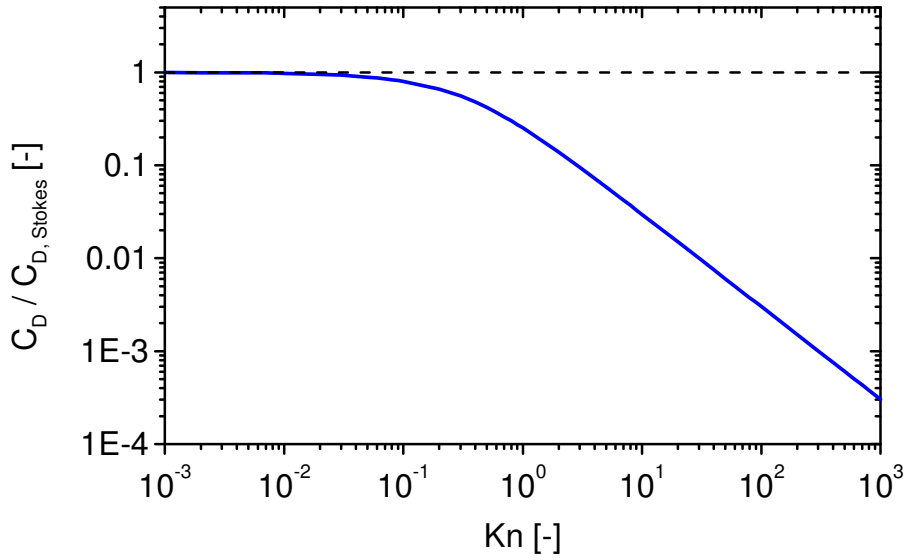

Figure 3.5: Modification of the drag coefficient due to rarefaction effects (Eq. (27)).

$$C_D = C_{D,0}\,\frac{1.0+\exp\left(-\dfrac{0.427}{Ma_P^{4.63}}-\dfrac{3.0}{\mathrm{Re}_P^{0.88}}\right)}{1.0+\dfrac{Ma_P}{\mathrm{Re}_P}\left\{3.82+1.28\,\exp\left(-1.25\,\dfrac{\mathrm{Re}_P}{Ma_P}\right)\right\}}, \qquad (30)$$

where $C_{D,0}$ is the drag coefficient given by Eqs. (17) and (19). The term in the nominator accounts for compressibility, while the denominator accounts for rarefaction effects. The drag coefficient versus Mach number is plotted in Figure 3.6 for a range of particle Reynolds number. For small particles the drag coefficient continuously is decreasing due to rarefaction effects, whereas it increases for large particles beyond a Mach number of about 0.6 due to compressibility effects. For intermediate particle Reynolds numbers a transition is observed. Other expressions for the drag coefficient including rarefaction and compressibility effects are given by Crowe et al. (1998).

At **higher volume fraction** of the dispersed phase a reduction of the sedimentation or rise velocity is observed in many technical multiphase flow processes. This phenomenon results mainly from the hydrodynamic interaction between the particles and is termed as hindered settling or rise, but also as swarm effect. A direct consideration of this phenomenon is only possible using direct numerical simulation (DNS) with resolving the flow around individual particles. For technical multiphase systems this is however not feasible and therefore, mainly empirical correlations are being used in engineering computations. A well-known correlation obtained from the sedimentation of a concentrated suspension (solids volume fraction between 1 and 20 %) is that of Richardson and Zaki (1954). The increase of the drag coefficient in a particle swarm is obtained from a correlation term being dependent on the solids volume fraction:

$$C_D = C_{D0}\cdot\left(1-\alpha_P\right)^{1-2\,K\left(\mathrm{Re}_{P0}\right)}. \qquad (31)$$

The correlation constant $K(Re_{P0})$ is a function of the single particle Reynolds number and the flow regime, i.e. laminar, transition or turbulent. The corresponding values or correlations are provided in Table 3.2.

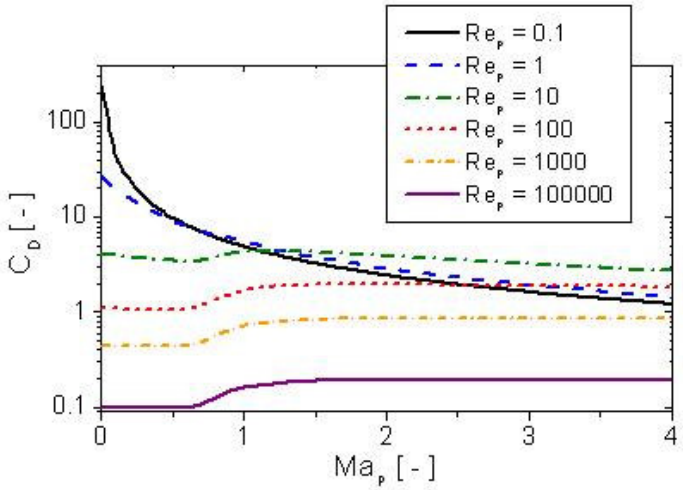

Figure 3.6: Modification of the drag coefficient due to rarefaction and compressibility effects for small and large particles(Eq. (30)); the particle Reynolds number increases from the upper to the lower line.

$K(Re_{P0})$	Reynolds number regime
4.65	$Re_p < 0.2$
$4.35\ Re_p^{-0.03}$	$0.2 < Re_p < 1$
$4.45\ Re_p^{-0.1}$	$1 < Re_p < 500$
2.39	$500 < Re_p < 5 \cdot 10^5$

Table 3.2: Correlation constant $K(Re_{P0})$ for the different ranges of single particle Reynolds number.

Another frequently used correlation for the increase of the drag coefficient with the solids volume fractions is that of Wen and Yu (1966), which is obtained from studying the sedimentation of spheres.

For solids volume fractions higher than 20 % the drag coefficient is determined from pressure drop correlations obtained for the flow through a packed bed as for example the correlation of Ergun (1952) which is valid for low and intermediate particle Reynolds numbers, hence includes a laminar and turbulent contribution:

$$\frac{\Delta p}{L} = 150\frac{(1-\varepsilon)^2}{\varepsilon^3}\frac{\mu\,\overline{w}}{d_{32}^2} + 1.75\frac{(1-\varepsilon)}{\varepsilon^3}\frac{\rho\,\overline{w}^2}{d_{32}}. \qquad (32)$$

Other more recent corrections for the drag coefficient of a particle swarm may be found in the book of Michaelides (2006).

3.2 Pressure gradient and Buoyancy force

The local pressure gradient in the flow gives rise to an additional force in the direction of the pressure gradient. Combining the pressure gradient with the shear stress in the fluid, one obtains:

$$F_p = \frac{m_p}{\rho_p}\left(-\nabla p + \nabla \vec{\tau}\right). \tag{33}$$

From the Navier-Stokes equation of the fluid the pressure gradient and the shear stress can be related to the fluid acceleration and the gravity force:

$$-\nabla p + \nabla \vec{\tau} = \rho_F \left(\frac{D\vec{u}_F}{Dt} - \vec{g} \right). \tag{34}$$

Hence the total pressure force is obtained in the following form:

$$\vec{F}_p = m_p \frac{\rho_F}{\rho_p} \left(\frac{D\vec{u}_F}{Dt} - \vec{g} \right). \tag{35}$$

The first term of Eq. (35) represents the fluid acceleration and the second one is the buoyancy force. It is obvious, that in gas-solid flows the pressure force may be neglected since $\rho_F/\rho_p \ll 1$. However, in liquid-solid flows this force is of importance since $\rho_F/\rho_p \approx 1$.

3.3 Added mass and Basset force

The acceleration/deceleration of a particle in a fluid also requires an acceleration or deceleration of a certain fraction of the surrounding fluid; this is the so-called added mass effect. The Basset force is caused by the lagging of the boundary layer development on the particle with changing relative velocity (i.e. acceleration or deceleration of the particle and/or fluid) and is often referred to as „history“ force. Analytic solutions for both forces are only possible for small particle Reynolds numbers (see Eq. (9)). An extension to higher particle Reynolds numbers is only possible by introducing empirical coefficients C_A and C_B similar to the drag coefficient. However, for the added mass and history forces, the introduction of these empirical coefficients is less successful for a general flow system.

Based on an experimental study of Odar and Hamilton (1964) who studied the motion of a sphere in simple harmonic motion, the added mass and Basset force are expressed as:

$$F_A = 0.5\, C_A \;\; \rho_F \frac{m_P}{\rho_P} \frac{d}{dt}\left(\vec{u}_F - \vec{u}_P\right), \tag{36}$$

$$F_B = 9\sqrt{\frac{\rho_F \;\mu_F}{\pi}} \frac{m_P}{\rho_P \;D_P} \;C_B \left\{ \int_0^t \frac{\frac{d}{dt}\left(\vec{u}_F - \vec{u}_P\right)}{\left(t-\tau\right)^{1/2}}\, d\tau + \frac{\left(\vec{u}_F - \vec{u}_P\right)_0}{\sqrt{t}} \right\}. \tag{37}$$

The second term in the Basset force accounts for an initial slip velocity at $t = 0$ (Reeks and McKee 1984). The coefficients C_A and C_B were obtained from the experiments of Odar and Hamilton (1964) in the following form:

$$C_A = 2.1 - \frac{0.132}{A_C^2 + 0.12}, \tag{38}$$

$$C_B = 0.48 + \frac{0.52}{\left(A_C + 1\right)^3}. \tag{39}$$

The parameter A_C is called acceleration number and is defined by:

$$A_C = \frac{\left|\vec{u}_F - \vec{u}_P\right|^2}{D_P \left|\frac{d\left|\vec{u}_F - \vec{u}_P\right|}{dt}\right|}. \tag{40}$$

It is obvious that the Basset force is quite time consuming to solve since it has to be integrated along the entire particle trajectory for each time step of the trajectory calculation. Therefore, this force is often neglected; although this is of course not a satisfying argument An approximate solution procedure for the Basset force was introduced by Michaelides (1992). Numerical calculations of Sommerfeld (1996) have shown that the consideration of the Basset force increases the computational time by a factor of about 10. An analysis of the importance of the different forces, especially added mass and Basset force, in an oscillatory flow field for different density ratios will be provided below.

3.4 Body force

Body or field forces are the gravity-buoyancy force, the Coulomb force, which arises when a particle moves in an electric field, as for example in an electrostatic precipitator or the thermophoretic force which becomes of importance when a small particle moves in a flow with a high temperature gradient.

The gravity force is:

$$\vec{F}_g = m_p \, \vec{g}. \tag{41}$$

The Coulomb force acting on a particle moving in an electric field with a field strength $\vec{E}$ is given by:

$$F_C = -q_p \, \vec{E}, \tag{42}$$

where q_p is the charge of the particle. In an electrostatic precipitator, for example, the particles are charged by an ion-bombardment created by a negative corona discharge in the vicinity of a charging wire. The charging of the particles is caused by two mechanisms: field charging and diffusion charging.

Field charging occurs due to the convective motion of the ions and is relevant for particles larger than about 0.5 to 1 µm. The saturation charge for a spherical particle is:

$$q_p = \pi \, \varepsilon_0 \, D_p^2 \, E_0 \, p, \tag{43}$$

where ε_0 is the permittivity of the free space, E_0 is the electric field strength in the charging region and $p = 3$ for conducting particles and $p = 1.5$ to 2.0 for non-conducting particles.

Diffusion charging is the result of the thermal motion of the ions and is relevant for particles with a diameter smaller than about 0.2 µm. The rate of charge increase due to diffusion charging is given by:

$$q_P(t) = 4\,\pi\,\varepsilon_0\,\frac{k\cdot T}{e}\,\frac{x}{2}\ln\left\{1+\frac{x\,c\,N_0\,e^2\,t}{8\,\varepsilon_0\,k\,T}\right\}, \qquad (44)$$

where k is the Boltzmann constant, e is the elementary charge, N_0 is the number density of the ions, c is the mean fluctuating velocity of the ions, t is the time, and T the absolute temperature of the gas. More details about particle charging and their motion in an electric field may be found in the book of White (1963).

3.5 Slip-shear lift force

Particles moving in a shear layer experience a transverse lift force, called the Saffman force, due to the non-uniform relative velocity over the particle and the resulting non-uniform pressure distribution. The lift force is acting towards the direction of higher slip velocity (Figure 3.7). An expression for the slip-shear lift force for a freely rotating particle moving at constant velocity in a two-dimensional shear flow at low Reynolds number was derived from an asymptotic expansion by Saffman (1965, 1968):

$$F^{y}_{LS,Saff} = 6.46\frac{D_p^2}{4}\left(\rho_F\;\mu_F\right)^{0.5}\left|\frac{\partial u_F}{\partial y}\right|\left(u_F - u_p\right). \qquad (45)$$

Extending this expression to a three dimensional flow and introducing a correction function for higher particle Reynolds numbers yields:

$$\vec{F}_{LS} = 1.615\;\;D_P^2\;\;\left(\rho_F\;\;\mu_F\right)^{1/2}\;\left(\frac{1}{|\vec{\omega}_F|}\right)^{0.5}\;\left\{\left(\vec{u}_F - \vec{u}_P\right)\times\vec{\omega}_F\right\}\;\;f(\mathrm{Re}_P, \mathrm{Re}_S)\,. \qquad (46)$$

Here the fluid rotation is obtained from:

$$\vec{\omega}_F = rot\;\vec{u}_F = \nabla\times\vec{u}_F\,. \qquad (47)$$

Introducing now a lift coefficient in Eq. (46) gives the following expression for the slip-shear lift force:

$$\vec{F}_{LS} = \frac{\rho_F}{2}\,\frac{\pi}{4}D_p^2\;\;C_{LS}\;\;D_P\left(\left(\vec{u}_F - \vec{u}_p\right)\times\vec{\omega}_F\right), \qquad (48)$$

with the lift coefficient:

$$C_{LS} = \frac{4.1126}{\mathrm{Re}_S^{0.5}}\;f\left(\mathrm{Re}_p, \mathrm{Re}_s\right). \qquad (49)$$

The correction function f ($\mathrm{Re_p}$, $\mathrm{Re_s}$) proposed by Mei (1992) on the basis of calculations performed by Dandy and Dwyer (1990) for a particle Reynolds number in the range $0.1 \le \mathrm{Re_p} \le 100$ is given by:

$$f\left(\mathrm{Re}_p, \mathrm{Re}_S\right) = \frac{F_{LS}}{F_{LS,Saff}}\,, \qquad (50)$$

$$\frac{F_{LS}}{F_{LS,Saff}} = \left(1 - 0.3314\ \beta^{1/2}\right)\ \exp\left(-\frac{\mathrm{Re}_P}{10}\right) + 0.3314\ \beta^{1/2} \quad for:\ \mathrm{Re}_P \le 40$$
$$\frac{F_{LS}}{F_{LS,Saff}} = 0.0524\left(\beta\ \mathrm{Re}_P\right)^{1/2} \quad for:\ \mathrm{Re}_P \ge 40 \qquad , \qquad (51)$$

with:

$$\beta = 0.5\,\frac{\mathrm{Re}_S}{\mathrm{Re}_p}. \qquad (52)$$

and the Reynolds number of the shear flow:

$$\mathrm{Re}_S = \frac{\rho_F\, D_p^2\, |\vec{\omega}_F|}{\mu_F}. \qquad (53)$$

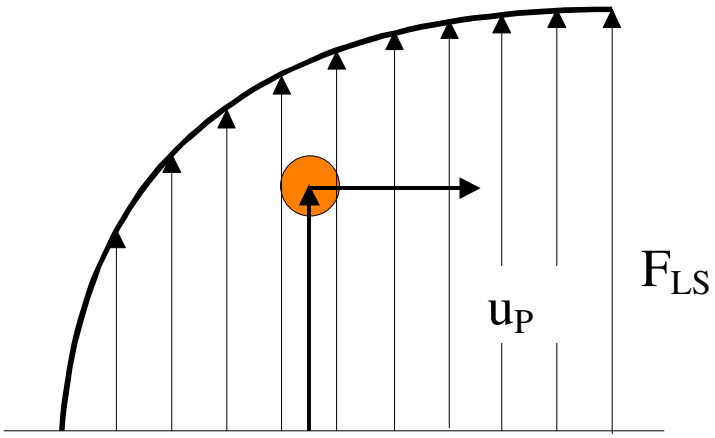

Figure 3.7: Illustration of the slip-shear lift force.

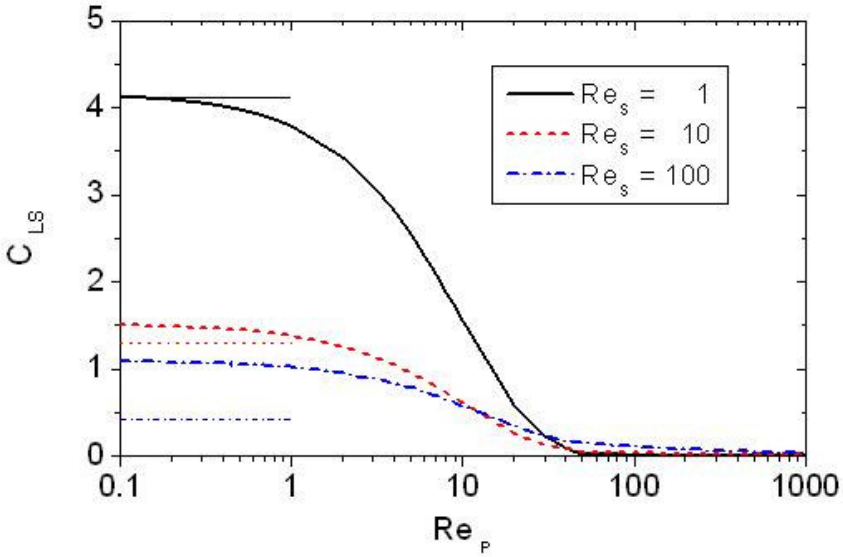

Figure 3.8: Lift coefficient as a function of particle Reynolds number with the shear Reynolds number as a parameter (The horizontal lines indicate the lift coefficients of the Saffman lift force, Eq. (49) with $f\left(\mathrm{Re}_p, \mathrm{Re}_S\right) = 1.0$).

The dependence of the lift coefficient on the particle Reynolds number with the shear Reynolds number as a parameter is shown in Figure 3.8. The horizontal lines indicate the values for the Saffman expression which are independent of particle Reynolds number and agree with the lift coefficient in Eq. (49) only for small Reynolds numbers. Although it is expected that the presence of other particles has a contribution to the lift force, there is no expression of the lift force taking the local volume fraction into account.

3.6 Slip-rotation lift force

Particles which are not freely rotating in a flow may also experience a lift force due to their rotation, the so-called Magnus force. High particle rotations may for example be induced by particle-wall collisions frequently occurring in pipe or channel flows. The rotation of the particle results in a deformation of the flow field around the particle, associated with a shift of the stagnation points and a transverse lift force (Figure 3.9). An analytic expression for the slip-rotation lift force in the case of small particle Reynolds numbers was derived by Rubinow and Keller (1961):

$$\vec{F}_{LR} = \pi\, R_p^3\, \rho_F \left\{ \vec{\Omega} \times \left(\vec{u}_F - \vec{u}_p \right) \right\}, \qquad (54)$$

where $\vec{\Omega}$ is the relative rotation given by:

$$\vec{\Omega} = \frac{1}{2} \nabla \times \vec{u}_F - \vec{\omega}_p \,. \qquad (55)$$

Also the slip-rotation lift force may be extended for higher particle Reynolds numbers by introducing a lift coefficient (Crowe et al. 1998):

$$\vec{F}_{LR} = \frac{\rho_F}{2} \frac{\pi}{4} D_p^2\, C_{LR} \left| \vec{u}_F - \vec{u}_p \right| \frac{\vec{\Omega} \times \left(\vec{u}_F - \vec{u}_p \right)}{\left| \vec{\Omega} \right|} \,. \qquad (56)$$

For small particle Reynolds numbers the lift coefficient is obtained according to Rubinow and Keller (1961) in the form:

$$C_{LR} = \frac{D_p \left| \vec{\Omega} \right|}{\left| \vec{u}_F - \vec{u}_p \right|} = \frac{\mathrm{Re}_R}{\mathrm{Re}_p}, \qquad (57)$$

with:

$$\mathrm{Re}_R = \frac{\rho_F\, D_p^2 \left| \vec{\Omega} \right|}{\mu_F}, \qquad (58)$$

being the Reynolds number of particle rotation. A lift coefficient for higher particle Reynolds numbers requires experimental information. Recently, Oesterlé and Bui Dinh (1998) introduced the following correlation based on available literature data and additional experiments for $\mathrm{Re_p} < 140$:

$$C_{LR} = 0.45 + \left(\frac{\mathrm{Re}_R}{\mathrm{Re}_P} - 0.45 \right) \exp\left(-0.05684 \cdot \mathrm{Re}_R^{0.4} \cdot \mathrm{Re}_P^{0.3} \right) \quad for: \quad \mathrm{Re}_P < 140 \,. \qquad (59)$$

The lift coefficient of particle rotation as a function of the particle Reynolds number with the Reynolds number of particle rotation as a parameter is shown in Figure 3.10. The upper and lower straight lines correspond to the result of Rubinow and Keller (1961) given by Eq. (57). It is obvious that this expression only holds for small particle Reynolds numbers.

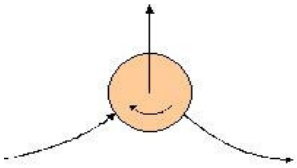

Figure 3.9: Illustration of the slip-rotation lift force acting on a stationary particle

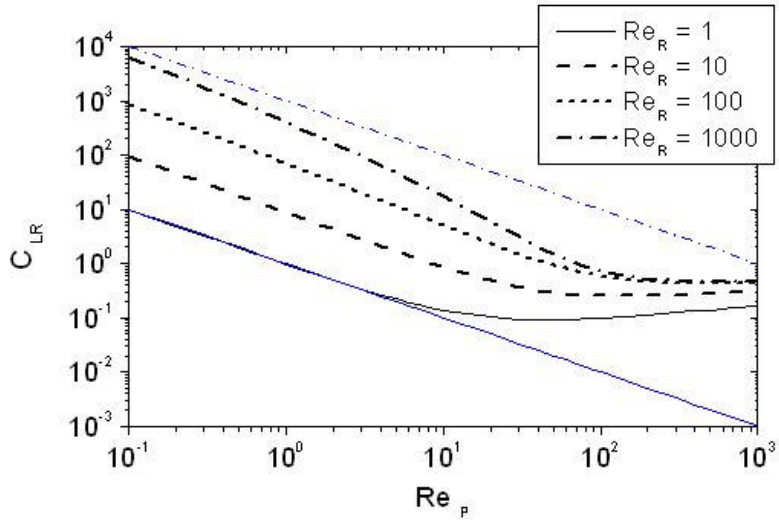

Figure 3.10: Lift coefficient of particle rotation as a function of particle Reynolds number with the Reynolds number of particle rotation as a parameter. The lower and upper straight lines correspond to the result of Rubinow and Keller (1961) for $Re_R = 1$ and $Re_R = 1000$, respectively.

3.7 Torque

The torque acting on a rotating particle due to the interaction with the fluid was also derived by Rubinow and Keller (1961) for a stagnant fluid and small particle Reynolds numbers:

$$\vec{T} = -\pi \, \mu_F \, D_p^3 \, \vec{\omega}_p \, . \qquad (60)$$

This expression may be extended for a three-dimensional flow and for higher Reynolds numbers by introducing a rotational coefficient:

$$\vec{T} = \frac{\rho_F}{2} \left(\frac{D_p}{2} \right)^5 C_R \left| \vec{\Omega} \right| \vec{\Omega} \, . \qquad (61)$$

From the numerical simulations of Dennis et al. (1980) and experimental data of Sawatzki (1970) the rotational coefficient for higher particle Reynolds numbers is found to be:

$$C_R = \frac{12.9}{\mathrm{Re}_R^{0.5}} + \frac{128.4}{\mathrm{Re}_R} \qquad for \;\; 32 < \mathrm{Re}_R < 1000 \,. \qquad (62)$$

In the case of smaller particle Reynolds numbers the result of Rubinow and Keller (1961) yields:

$$C_R = \frac{64\,\pi}{\mathrm{Re}_R} \qquad for \;\; \mathrm{Re}_R < 32 \,. \qquad (63)$$

The comparisons of the above correlations (Eqs. (62) and (63)) with the simulations (Dennis et al. 1980) and the experiments (Sawatzki 1970) give a good agreement as shown in Figure 3.11.

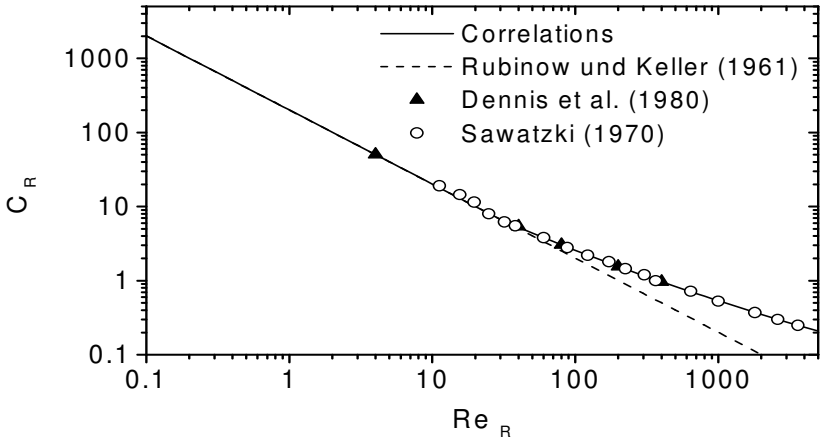

Figure 3.11: Coefficient of particle rotation as a function of particle rotational Reynolds number according to Eqs.(62) and (63), and comparison with experiments (Sawatzki 1970) and numerical calculations (Dennis et al. 1980).

3.8 Response time and Stokes number

The particle velocity or momentum response time may be used to characterise the capability of particles to follow a sudden velocity change in the flow, occurring for example in large scale vortical structures (Tang et al. 1992) or turbulent eddies. In order to derive the particle response time the equation of motion is used by only considering the drag force.

$$m_p \frac{du_p}{dt} = \frac{\rho_F}{2}\frac{\pi}{4} D_p^2 C_D \left|u_F - u_p\right| \left(u_F - u_p\right). \qquad (64)$$

Dividing by the particle mass and introducing the particle Reynolds number gives:

$$\frac{du_p}{dt} = \frac{18\,\mu_F}{\rho_p\, D_p^2}\frac{C_D\,\mathrm{Re}_p}{24}\left(u_F - u_p\right). \qquad (65)$$

The term C_D $\mathrm{Re}_p/24$ corresponds to the non-linear term in the drag coefficient f_D (Eq. (17)) and the first term of Eq. (65) has the dimension of a time, the particle response time:

$$\tau_p = \frac{\rho_p\, D_p^2}{18\,\mu_F\, f_D} \,. \qquad (66)$$

Hence the equation of motion becomes:

$$\frac{du_p}{dt} = \frac{1}{\tau_p}\left(u_F - u_p\right). \qquad (67)$$

The solution of this equation for a simplified case, namely a jump of the fluid velocity from zero to u_F and an initial particle velocity of zero is:

$$u_p = u_F\left(1 - \exp\left(-\frac{t}{\tau_p}\right)\right). \qquad (68)$$

From this equation it is obvious that τ_p is the time required for a particle, released with zero velocity into a flow with u_F, to reach 63.2 % of the flow velocity as illustrated in Figure 3.12.

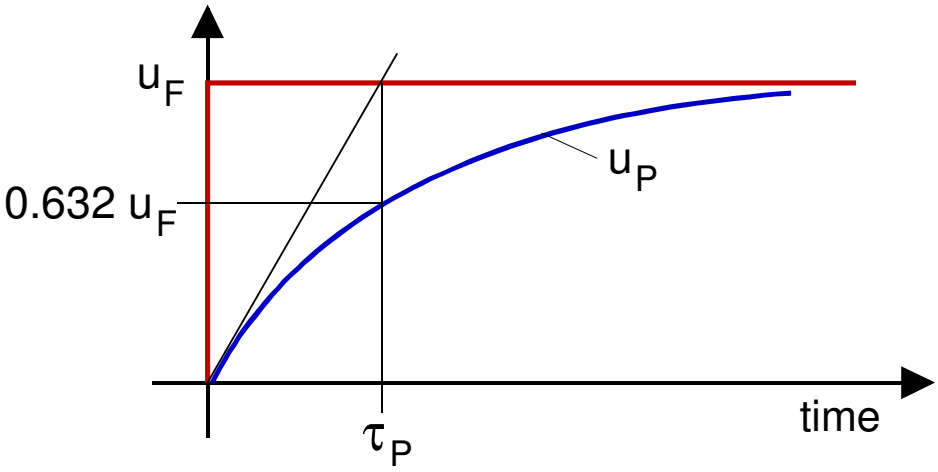

Figure 3.12: Graphical illustration of the particle response time.

In the Stokes-regime, where f_D is unity, the particle response time becomes:

$$\tau_p = \frac{\rho_p D_p^2}{18\,\mu}. \qquad (69)$$

The Stokes number is the ratio of the particle response time to a characteristic time scale of the flow:

$$St = \frac{\tau_p}{\tau_F}. \qquad (70)$$

Considering particle motion in a turbulence field the fluid flow time scale corresponds to the time scale of the energetic eddies, i.e. the integral time scale of turbulence, $T_L \approx k/\varepsilon$. In the case of particle motion in large scale vortices (occurring for example in a shear layer) the eddy passage time across a fixed point in space is the relevant fluid time scale (Tang et al. 1992).

3.9 Importance of the different forces

In order to estimate the importance of the different forces, especially the importance of added mass and Basset force, acting on a particle in a turbulent flow, Hjelmfeld & Mockros (1966) have performed an analysis for an oscillatory flow field. The starting point of their analysis

was the Stokes form of the equation of motion given by:

$$m_P \frac{d\,u_P}{d\,t} = \frac{18\,\mu_F}{\rho_P\ D_P^2}\ m_P\ (u_F - u_P)\ -\ m_F \frac{d\,u_F}{d\ t} + 0.5\,m_F \left(\frac{d\,u_F}{d\,t} - \frac{d\,u_P}{d\,t}\right) + 9\sqrt{\frac{\rho_F\ \mu_F}{\pi}}\ \frac{m_P}{\rho_P\ D_P}\ \int_{-\infty}^{t} \frac{\frac{d\ u_F}{d\ \tau} - \frac{d\ u_P}{d\ \tau}}{(t-\tau)^{1/2}}\ d\,\tau. \qquad (71)$$

Rearranging this equation results in:

$$\frac{d\,u_P}{d\,t} + a\,u_P + c\ \int_{-\infty}^{t} \frac{d\ u_P/d\ \tau}{(t-\tau)^{1/2}}\ d\,\tau = a\,u_F + b\ \frac{d\,u_F}{d\ t} +\ \ c\ \int_{-\infty}^{t} \frac{d\ u_F/d\ \tau}{(t-\tau)^{1/2}}\ d\,\tau\,, \qquad (72)$$

with the coefficients *a, b* and *c* defined by:

$$a = \frac{18\ \mu_F/\rho_F}{(\rho_P/\rho_F + 0.5)\ D_P^2}\,,\ b = \frac{3}{2\,(\rho_P/\rho_F + 0.5)}\,,\ c = \frac{9}{(\rho_P/\rho_F + 0.5)}\sqrt{\frac{\mu_F}{\pi\,\rho_F}}\,. \qquad (73)$$

The velocities of the particles and the fluid are expressed by Fourier integrals:

$$u_F = \int_0^{\infty} (\varsigma \cos \omega t + \lambda \sin \omega t)\,d\,\omega\,, \qquad u_P = \int_0^{\infty} (\sigma \cos \omega t + \phi \sin \omega t)\,d\,\omega\,, \qquad (74)$$

where ω is the frequency of oscillation. Introducing these Fourier integrals into the equation of motion of the particles (Eq. (72)) yields the amplitude ratio (i.e. amplitude of particle velocity over that of the fluid) and the phase angle (i.e. lag of particle response) in the following form:

$$\eta = \sqrt{(1+f_1)^2 + f_2^2}\,, \qquad \beta = \tan^{-1}\left\{\frac{f_2}{1+f_1}\right\}. \qquad (75)$$

The functions f_1 and f_2 are obtained as:

$$f_1 = \frac{\omega\left(\omega + c\sqrt{0.5\,\pi\,\omega}\right)(b-1)}{\left(a + c\sqrt{0.5\,\pi\,\omega}\right)^2 + \left(\omega + c\sqrt{0.5\,\pi\,\omega}\right)^2}\,, \qquad (76)$$

$$f_2 = \frac{\omega\left(a + c\sqrt{0.5\,\pi\,\omega}\right)(b\text{-}1)}{\left(a + c\sqrt{0.5\,\pi\,\omega}\right)^2 + \left(\omega + c\sqrt{0.5\,\pi\,\omega}\right)^2}\,. \qquad (77)$$

The result of this analysis is shown in for three kinds of particles, namely copper and glass particles in air and air bubbles in water, by considering the different forces. For the three cases the amplitude ratio and the phase angle is plotted versus the modified Stokes number. It is obvious that for copper particles and glass beads the added mass, the pressure force, and the Basset term have almost no effect on the amplitude ratio. However, considerable differences are observed in the phase angle for $N_s < 5$, which means for large particles or high frequencies of the oscillatory fluid motion. Only the added mass is not of great importance and may be neglected without considerable error. Considering a 100 µm particle the pressure force and the Basset term become of importance for oscillation frequencies larger than about 310 Hz.

For bubbly flows large differences in the response arise for $N_s < 1.0$. However, for this case the Basset term may be neglected without introducing very large errors. The added mass and the pressure force on the other hand are of great importance in this region, i.e. for large bubbles and high frequencies of flow oscillation. The parameter used to characterise the particle response is a modified Stokes number given by:

$$N_s = \frac{\mu_F}{\rho_F \, \omega \, D_p^2}. \tag{78}$$

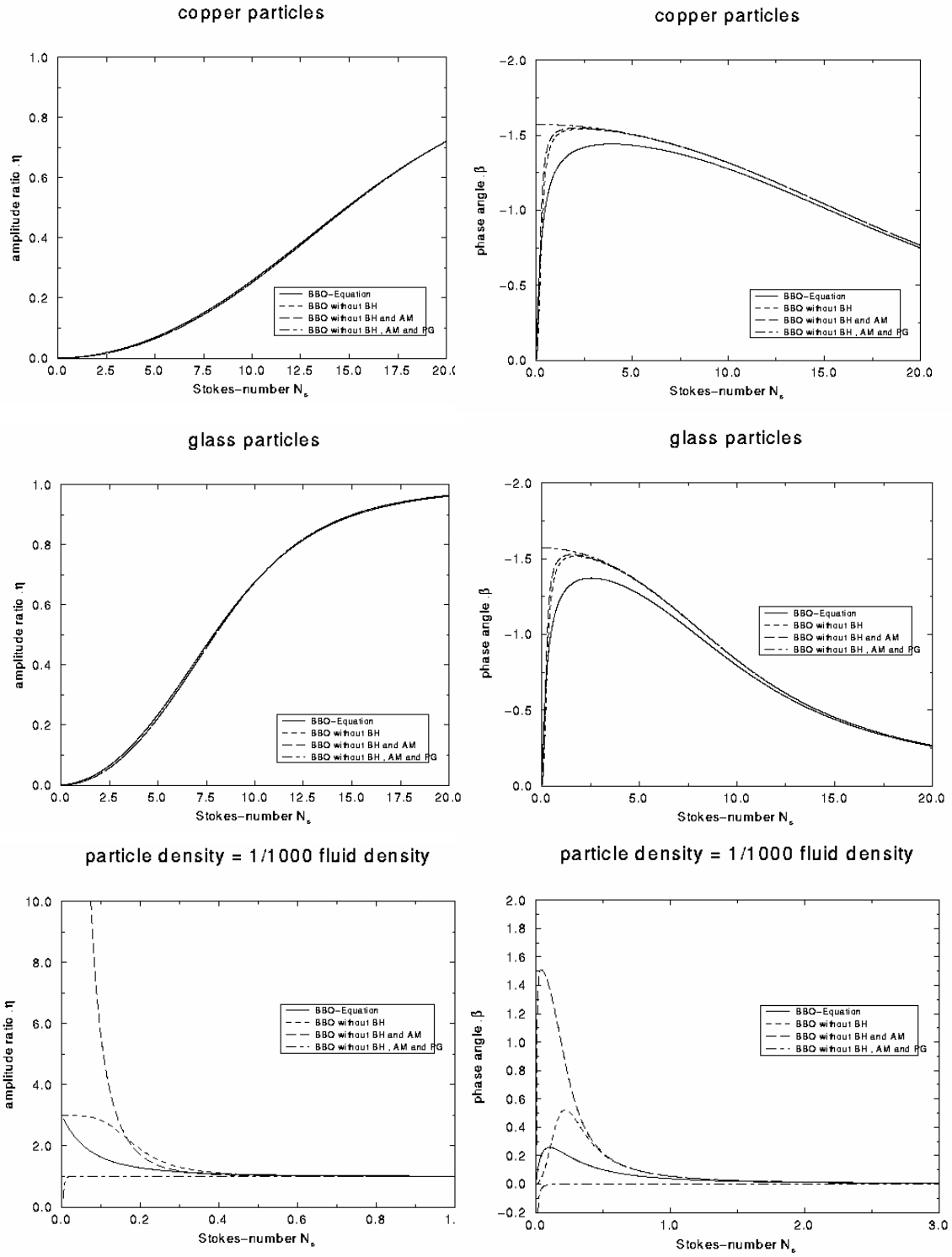

Figure 3.13: Particle response in an oscillatory flow field, influence of the different forces on the amplitude ratio (left column) and the phase angle (right column) for: a) copper particles in air, b) glass beads in air, c) air bubbles in water.

3.10 Forces acting on bubbles

The motion of bubbles in laminar or turbulent flows is much more complex than that of rigid solid particles. First of all, the interface between bubble and fluid is not rigid due to the internal flow developing inside the bubbles. This implies that the interface has a finite relative velocity. Thereby the drag coefficient is reduced compared to a solid particle which has zero relative velocity at the surface. This is depicted in the well known diagram of Clift et al. (1986) where the terminal velocity is plotted versus the volume equivalent diameter obtained from a number of experimental data (Figure 3.14). The second issue, which considerably complicates the modelling of bubble motion, is the contamination of the bubble surface by surface active substances, e.g. surfactants. This yields eventually a rigid interface and the bubble behaves like a solid particle and the drag coefficient as well as the rise velocity decreases (Figure 3.14). The third phenomenon affecting bubble motion is bubble deformation and oscillation which begins for volume equivalent bubble diameters around 1.5 mm for an air water system. Bubble oscillation is triggered by unsteady wake separation and causes the bubbles to rise in a zigzag or spiral manner.

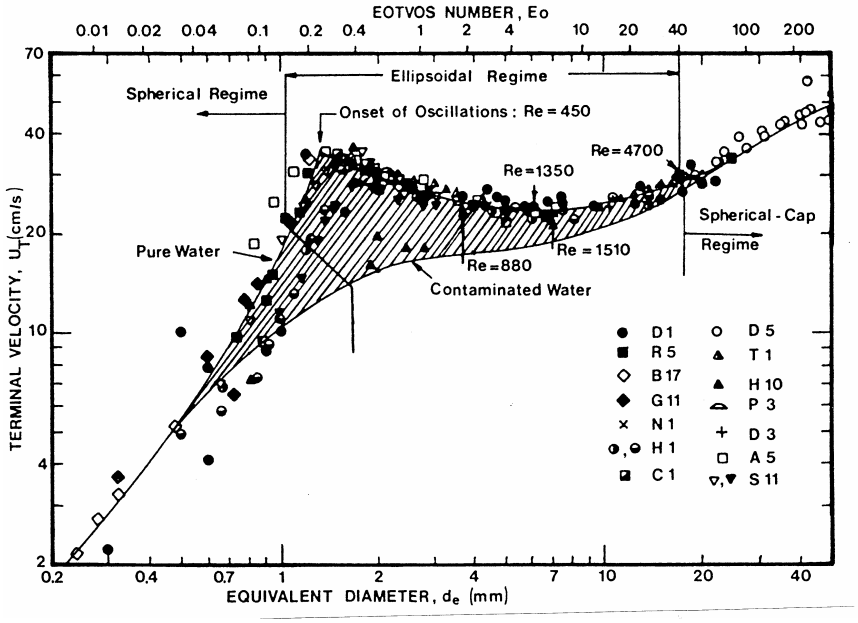

Figure 3.14: Collection of experimental data on the rise velocity of bubbles in different liquids by Clift et al. (1986) together with fitting lines for pure and contaminated liquids.

The bubble shape is determined from the relative importance of the fluid dynamic force acting on the bubble to the force due to the surface tension. This ratio yields the Weber-number given by:

$$We_B = \frac{|\rho_F - \rho_B| V_B^2 D_e}{\sigma} \qquad (79)$$

In case the Weber-number becomes large the spherical bubble shape cannot be maintained

and bubbles become ellisoidal, wobbling or spherical-cap. The different bubble shapes can be characterised by introducing two additional non-dimensional numbers, namely the Eötvös- and Morton-number:

$$Eo = \frac{We_B}{Fr_B} = \frac{\rho \left| \rho_F - \rho_B \right| D_e^2}{\sigma}, \tag{80}$$

$$Mo = \frac{g\ \mu^4 \left| \rho_F - \rho_B \right|}{\rho_F^2\ \sigma^3}, \tag{81}$$

where:

$$Fr_B = \frac{V_B^2}{g\ \ D_e}, \tag{82}$$

is the bubble Froude-number. These non-dimensional parameters are being used to obtain the well-known bubble-shape diagram as shown in Figure 3.14 (Clift et al. 1986). For the numerical calculation of bubble motion all forces have to be considered such as drag force, pressure force, added mass, Basset force, gravity force and transverse lift force. The importance of these forces was discussed above. Nevertheless, the Basset force is neglected in most computational studies due to the considerably increasing numerical effort, which is however not justified for all regimes of bubble size and oscillation frequency of the flow.

Numerous experimental studies are available for the determination of the drag coefficient for different sized bubbles rising in purified or contaminated liquids (Haberman and Morton 1953, Peeble and Garber 1953) which were also summarised by Fan and Tsushiya (1990). These data were obtained my measuring the bubble terminal velocity under quasi-steady state conditions neglecting added mass and Basset forces. In the low Reynolds number regime (including the laminar regime) a clear distinction between bubbles rising in purified and contaminated liquids can be made. In the Stokes regime (and in some cases up to bubble Reynolds numbers larger than 10) contaminated bubbles rise like rigid particles with a drag coefficient of:

$$C_D = \frac{24}{\mathrm{Re}_B}. \tag{83}$$

Whereas, in purified systems the drag coefficient is lower; namely:

$$C_D = \frac{16}{\mathrm{Re}_B}. \tag{84}$$

Most critical is the regime of ellipsoidal and wobbling bubbles where the transition of the drag coefficient is extremely affected by the type of liquid considered. In a contaminated mixture of glycerine and water for example, this transition is shifted to lower bubble Reynolds numbers if the glycerine content is increased (Fan and Tsushiya 1990).

When the bubble Reynolds number increases beyond about 1530 and the bubbles have a cap-like shape, the degree of contamination of the liquid does not play a role anymore and the drag coefficient approaches a constant value of about:

$$C_D \cong 2.61. \tag{85}$$

In the past, numerous correlations for the bubble drag coefficient as a function of bubble

Reynolds number were proposed, mainly to match the transition region most closely for the different types of liquids. A discontinuous correlation for bubbles rising in purified liquid was for example proposed by Glaeser and Brauer (1977). Here the drag coefficient in the transition region depends on the Morton number and the bubble Reynolds number with an exponent of 0.4. The beginning and the end of the transition region are given by two Reynolds numbers both depending on the Morton number. The Morton number, as given above, is only dependent on the properties of the considered media, i.e. viscosity, density and surface tension. Several correlations which are rather easy to use were proposed by Tomiyama et al. (1998):

$$\text{- purified fluids: } C_D = \max\left\{\min\left[\frac{16}{\mathrm{Re}}\left(1+0.15\,\mathrm{Re}^{0.687}\right), \frac{48}{\mathrm{Re}}\right], \frac{8}{3}\frac{Eo}{Eo+4}\right\}, \tag{86}$$

$$\text{- slightly contaminated fluids: } C_D = \max\left\{\min\left[\frac{24}{\mathrm{Re}}\left(1+0.15\,\mathrm{Re}^{0.687}\right), \frac{72}{\mathrm{Re}}\right], \frac{8}{3}\frac{Eo}{Eo+4}\right\} \tag{87}$$

$$\text{- contaminated fluids: } C_D = \max\left[\frac{24}{\mathrm{Re}}\left(1+0.15\,\mathrm{Re}^{0.687}\right), \frac{8}{3}\frac{Eo}{Eo+4}\right]. \tag{88}$$

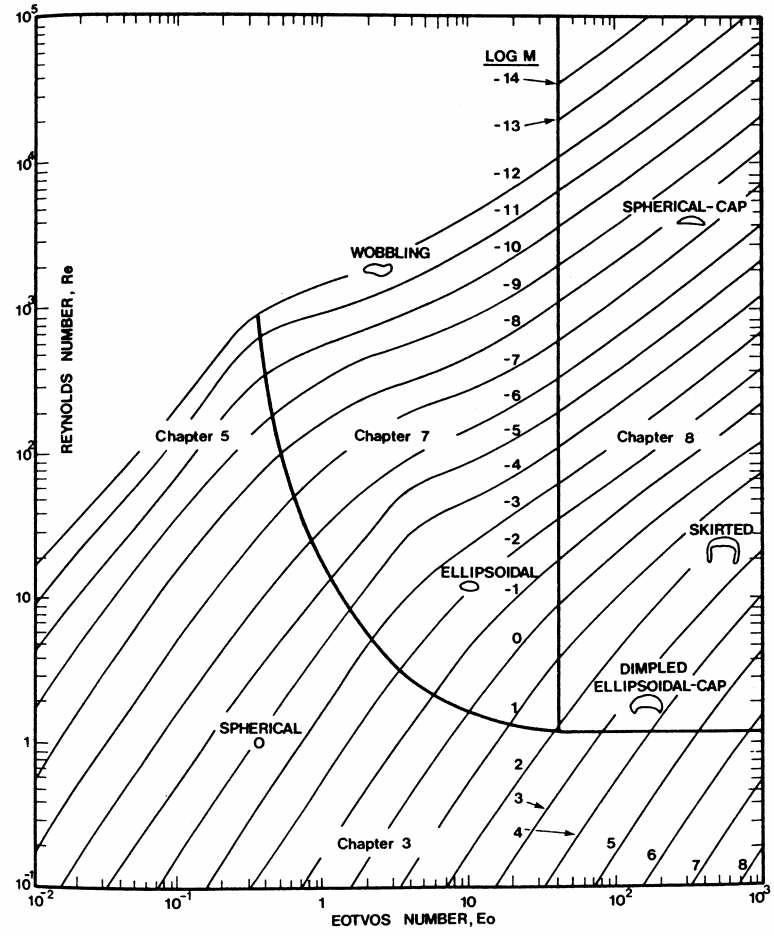

Figure 3.15: Bubble shape regimes as a function of Reynolds and Eötvös number with the Morton number as a parameter (Clift et al. 1986).

As illustrated in Figure 3.16, these correlations however do not properly describe the transition region in dependence on the degree of contamination and type of liquid considered as found in numerous experimental studies (Fan and Tsushiya 1990). Especially this region, with bubble sizes between 3 and 6 mm for an air/water system, a more accurate description is needed, since such bubble sizes are most important for industrial processes. Hence, so far no generally applicable correlation for the drag coefficient of bubbles is available. Therefore, published results on the hydrodynamics in bubble columns or loop reactors have to be very critically assessed with regard to the drag correlation applied.

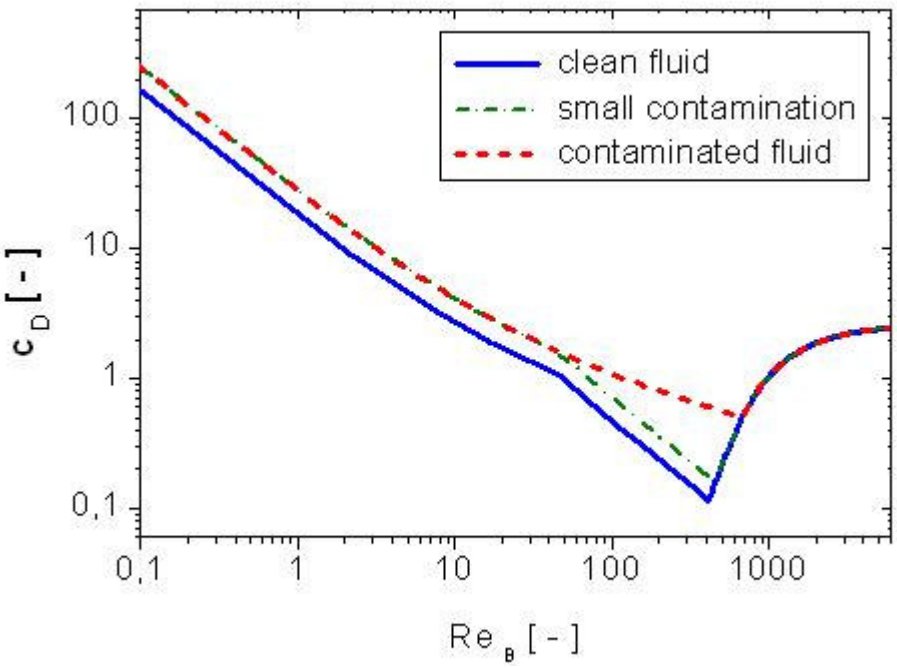

Figure 3.16: Bubble drag coefficient as a function of the bubble Reynolds number for clean and contaminated water according to the correlations of Tomiyama et al. (1998), see Eqs.(86) to (88).

In bubbly flows the added mass force is of great importance since especially wobbling bubbles never exhibit stationary rise behaviour, rather they show zigzag or helical rising paths. Additionally, the density ratio ρ_L / ρ_B is considerably larger than one. For spherical bubbles in the Stokes regime the added mass coefficient is also 0.5. In the case of ellipsoidal bubbles the added mass coefficient is a tensor of the form:

$$C_{VM} = \begin{Bmatrix} C_{vm,h} & 0 & 0 \\ 0 & C_{vm,h} & 0 \\ 0 & 0 & C_{vm;h} \end{Bmatrix}. \qquad (89)$$

For oblate bubbles an analytic solution for the coefficients in horizontal (h) and vertical (v) direction were provided by Lamb (1932) as a function of axis ratio (i.e. minor axis to major axis, $E = h/b$).

$$C_{VM,v} = \frac{E \cos^{-1} E - \sqrt{1-E^2}}{E^2 \sqrt{1-E^2} - E \cos^{-1} E} \qquad for\ E < 1, \qquad (90)$$

$$C_{VM,h} = \frac{\cos^{-1} E - E\sqrt{1-E^2}}{\left(2E^{-1} - E\right)\sqrt{1-E^2} - \cos^{-1} E} \qquad for\ E < 1. \qquad (91)$$

Moreover, transverse lift forces play an important role in the behaviour of bubbles. For example in bubble columns or pipe flows the void fraction profile shows wall peaking for smaller bubbles (i.e. D_B < 5.6 mm in an air/water system under atmospheric conditions) and core peaking is observed for larger bubbles. The latter is also the responsible mechanism for yielding a heterogeneous flow regime in a bubble column. The transverse lift force acting on bubbles may be separated in two contributions, namely due to shear flow and bubble wake effects. Combining these two effects in one lift coefficient yields the following lift force:

$$\vec{F}_L = C_L\, \rho_L \frac{\pi D_B^3}{6}\left(\vec{U}_L - \vec{U}_B\right) x\ rot\, \vec{U}_L. \qquad (92)$$

Here a positive value of C_L should yield a migration of the bubbles towards the wall. For spherical bubbles and for $Re_B >> 1$ the lift coefficient is 0.5 (Auton 1987). On the basis of experimental studies in a shear flow and simulations using the VOF (volume of fluid) method Tomiyama et al. (2002) suggest the following correlations for the lift coefficient:

$$C_A = \begin{cases} \min\left(0.288 \cdot \tan h\left(0.121\, \mathrm{Re}_B\right)\right), f\left(Eo_h\right) & für:\ Eo_h < 4 \\ f\left(Eo_h\right) & für:\ 4 \le Eo_h \end{cases}, \qquad (93)$$

with:

$$f\left(Eo_h\right) = 0.00105\, Eo_h^3 - 0.0159\, Eo_h^2 - 0.0204\, Eo_h + 0.474, \qquad (94)$$

$$Eo_h = \frac{\rho\, \Delta\rho\, D_h^2}{\sigma}; \quad D_h = 2\, b. \qquad (95)$$

For smaller bubbles the lift coefficient correlates with the bubble Reynolds number (i.e. up to $Re_B \sim 60$) and has positive values (i.e. migration towards the wall of a pipe). If medium sized and large bubbles are considered, the lift coefficient correlates with the Eötvös number based on the volume equivalent bubble diameter (Tomiyama et al. 2004). The lift coefficient changes from positive to negative values at about $Eo = 4$, corresponding to a bubble diameter of 5.6 mm in an air/water system. In both regions (Eq. (93)) the lift coefficient was found to be almost independent of the Morton number. The theoretical studies of Legendre and Magnaudet (1997) for a plane shear layer revealed that for bubble Reynolds numbers below about 3 the shear induces transverse lift is dominating and therefore, the lift coefficient will become dependent on the non-dimensional shear rate:

$$S_r = \frac{w\, D_B}{\left|U_L - U_B\right|}; \qquad w = \frac{d\, U_L}{dy}. \qquad (96)$$

The correlation for the lift coefficient obtained from these simulations is given by:

$$C_A = \sqrt{\left(\frac{6}{\pi^2}\frac{2.255}{\left(\mathrm{Re}_B\, Sr\right)^{1/2}\left(1 + 0.2\, \mathrm{Re}_B / Sr\right)^{3/2}}\right)^2 + \left(0.5\frac{1 + 16/\mathrm{Re}_B}{1 + 29/\mathrm{Re}_B}\right)^2}, \qquad (97)$$

and agrees with experiments of Tomiyama et al. (2004) up to a bubble Reynolds number of 2.0. For $Re_B > 5$ the influence of the shear rate on the lift coefficient becomes negligible and the correlation of Eq. (93) can be used.

4 Computational Multiphase Fluid Dynamics for dispersed flows

4.1 DNS resolving the particles

Multi-fluid flows in which a sharp interface exists are frequently encountered in a variety of industrial processes. It has proven particularly difficult to accurately simulate these flows which can be attributed to i) the fact that the interface separating the fluids needs to be tracked accurately without introducing excessive computational smearing ii) the necessity to account for surface tension in case of (highly) curved interfaces. In the past decade a number of techniques, each with their own particular advantages and disadvantages, have been developed to simulate complex multi-fluid flow problems. The most important techniques are summarised in Table 4.1 together with their main advantages and disadvantages. Similar to other DNS techniques the temporal and spatial resolution is such that all details of the flow fields are captured which enables a priori prediction of the drag, lift and added mass forces experienced by the dispersed elements moving either in isolation or in (dense) swarms in a continuous phase. As such it can provide vital information on the closures for the phase interactions required for either Euler-Lagrange or Euler-Euler type of models that can in principle be applied to engineering problems. Subsequently these techniques will be briefly reviewed.

Method:	Advantages	Disadvantages
Front Tracking	Extremely accurate Robust Account for substantial topology changes in interface Merging and breakage of interfaces does not occur automatically	Mapping of interface mesh onto Eulerian mesh Dynamic remeshing required Merging and breakage of interfaces requires sub-grid model
Level Set	Conceptually simple Easy to implement	Limited accuracy Loss of mass (volume)
Shock Capturing	Straightforward implementation Abundance of advection schemes are available	Numerical diffusion Fine grids required Limited to small discontinuities
Marker Particle	Extremely accurate Robust Accounts for substantial topology changes in interface	Computationally expensive Re-distribution of marker particles required
SLIC VOF	Conceptually simple Straightforward extension to	Numerical diffusion

	three dimensions	Limited accuracy Merging and breakage of interfaces occurs automatically
PLIC VOF	Relatively simple Accurate Accounts for substantial topology changes in interface	Difficult to implement in three dimensions Merging and breakage of interfaces occurs automatically
Lattice Boltzmann	Accurate Accounts for substantial topology changes in interface	Difficult to implement Merging and breakage of interfaces occurs automatically
Immersed Boundary	Accurate Conceptually simple Easy to implement	Mapping of interface mesh onto Eulerian mesh Merging and breakage of interfaces requires sub-grid model

Table 4.1 Overview of techniques for multi-fluid flows with sharp interfaces.

4.1.1 Front tracking methods

Front tracking methods (Unverdi and Tryggvason, 1992; Esmaeeli and Tryggvason, 1998a, 1998b and Tryggvason et al., 2001) make use of a markers (for instance triangles), connected to a set of points, to track the interface whereas a fixed or Eulerian grid is used to solve the Navier-Stokes equations. This method is extremely accurate but also rather complex to implement due to the fact that dynamic remeshing of the Lagrangian interface mesh is required and mapping of the Lagrangian data onto the Eulerian mesh has to be carried out. Difficulties arise when multiple interfaces interact with each other as in coalescence and breakup, which both require a proper sub-grid model. Contrary to most other methods, the automatic merging of interfaces does not occur in front tracking techniques due to the fact that a separate mesh is used to track the interface. This property is advantageous in case swarm effects in dispersed flows need to be studied. Due to this Lagrangian representation of the interface this technique offers considerable flexibility to assign different properties (e.g. the surface tension coefficient) to separate dispersed elements.

4.1.2 Level set methods

Level set methods (Sussman et al., 1994, 1999; Sethian, 1996; Chang et al., 1996; Sussman and Smereka, 1997; Sussman and Fatemi, 1999 and Fedkiw and Osher, 2001) are designed to minimize the numerical diffusion hampering shock-capturing methods and typically define the interface as the zero level set of a distance function from the interface. The advection of this distance function evolves through the solution of the following equation:

$$\frac{DF}{Dt} = \frac{\partial F}{\partial t} + (\overline{u} \cdot \nabla F) = 0, \qquad (98)$$

expressing that the interface property F is advected with the local fluid velocity u. Level set

methods are conceptually simple and relatively easy to implement and yield accurate results when the interface is advected parallel to one of the co-ordinate axis. However, in flow fields with appreciable vorticity or in cases where the interface is significantly deformed, level set methods suffer from loss of mass (volume) and hence loss of accuracy.

4.1.3 Shock capturing methods

In **shock capturing methods** (Ida, 2000) high order shock-capturing schemes are used to treat the convective terms in the governing equations. The advantage of this method is that explicit reconstruction of the interface is circumvented which offers advantages for unstructured grids. Although state-of-the-art shock capturing methods are quite sophisticated, they work less well for the sharp discontinuities usually encountered in multi-fluid flows. Moreover, they require relatively fine grids to obtain accurate solutions. Rider and Kothe (1995) used a high order Godunov method and conducted several numerical tests and concluded that "In all cases the use of shock-capturing methods was inadequate."

4.1.4 Marker particle methods

In **marker particle methods** (Welch et al., 1965; Rider and Kothe, 1995) marker particles are assigned to a particular fluid and are used to track the motion (and hence the interface) of this fluid. From the instantaneous positions of the marker particles the relevant Eulerian fluid properties, required to solve the Navier-Stokes equation, are retrieved. Marker particle methods are extremely accurate and robust and can be used successfully to predict the topology of an interface subjected to considerable shear and vorticity in the fluids sharing the interface. However, this method is computationally very expensive, especially in 3D. Moreover, difficulties arise when the interface stretches considerably which necessitates the addition of fresh marker particles during the flow simulation. Similar difficulties arise when the interface shrinks. Also merging and break-up of interfaces poses a problem; again a proper sub-grid model needs to be invoked.

4.1.5 Volume of fluid methods

Volume of fluid (VOF) methods (Hirt and Nichols, 1981; Youngs, 1982; Rudman, 1997; Rider and Kothe, 1998; Scardovelli and Zaleski, 1999; Popinet and Zaleski, 1999; Bussman et al., 1999) employ a colour function F(x,y,z,t) that indicates the fractional amount of fluid present at a certain position (x,y,z) at time t. The evolution equation for F is again equation (1.1) that is usually solved using special advection schemes (such as geometrical advection, a pseudo-Lagragian technique), in order to minimize numerical diffusion. In addition to the value of the colour function the interface orientation needs to be determined, which follows from the gradient of the colour function. Roughly two important classes of VOF methods can be distinguished with respect to the representation of the interface, namely **Simple Line Interface Calculation** (SLIC) and **Piecewise Linear Interface Calculation** (PLIC). Earlier work is generally typified by the SLIC algorithm due to Noh and Woodward (1976) and the Donor-Acceptor algorithm published by Hirt and Nichols (1981). Modern VOF techniques include the PLIC method due to Youngs (1982). The accuracy and capabilities of the modern PLIC VOF algorithms greatly exceeds that of the older VOF algorithms such as the Hirt and Nichols VOF method (Rudman, 1997). A drawback of VOF methods is the so-called artificial (or numerical) coalescence of gas bubbles which occurs when their mutual distances is less than the size of the computational cell. On the other hand when coalescence is known to prevail, the VOF method, contrary to the Front Tracking method does not require specific algorithms for the merging (or breakage) of the interface.

4.1.6 Lattice Boltzmann Methods

The **Lattice Boltzmann Method** (LBM) can be viewed as a special, particle based discretisation method to solve the Boltzmann equation. This method is particularly attractive in case multiple moving objects (particles, bubbles or droplets) have to be treated. Contrary to

the classical finite difference and finite element methods, the LBM avoids the dynamic remeshing which becomes prohibitive for a large number of moving objects.

The starting point of the LBM is a discrete system of fluid particles residing on a regular lattice (in its elementary and most-used form this is a uniform, cubic (in 3D) or square (in 2D) lattice). These fluid particles are, in a way, fictitious particles that should not be confused with real particles (solid particles, or drops, or bubbles) that are abundantly present in multiphase flows.

The LBM is inherently time-dependent. Each time step the fictitious particles move to their neighbouring sites where they collide with particles coming in from the other directions according to specific rules. Since particles are only allowed on lattice sites, there is a discrete set of allowable velocities for the particles. With a Chapman-Enskog (CE) expansion this discrete system can be written in a continuous form. With the proper lattice topology and collision rules the partial differential equations emerging from the expansion can be shown to resemble the compressible continuity and Navier-Stokes equations.

In the incompressible limit (the LBM is a compressible numerical scheme since particles only travel one lattice spacing per time step, i.e. the system has a finite speed of sound) the continuity and Navier-Stokes equations are accurately recovered by the CE expansion of the LBM. The LBM is second-order accurate in space and time. From a numerical point of view the restriction of being in the incompressible limit implies taking small time steps; typically one order of magnitude smaller than in explicit finite volume schemes.

Ladd (1994a, 1994b) has used the LBM successfully to compute the effective gas-particle drag in particulate suspensions whereas Sundaresan and co-workers (Sankaranarayanan et al., 2002a and Sankaranarayanan and Sundaresan, 2002b) recently extended this technique to deformable interfaces and applied this technique sucessfully to study the dynamics of isolated gas bubbles rising in quiescent liquids. However, similar to VOF methods in this method problems may arise due to the artificial coalescence of the dispersed elements (gas bubbles).

There are three main reasons for considering lattice-Boltzmann methods for attacking flow problems inherent parallelism numerical efficiency not hampered by geometrical complexity intuitive extension to multi-physics. The notion of fictitious particles colliding and moving to neighbouring lattice sites implies locality of the numerical operations involved. This locality makes distribution of the computational load by means of domain composition a simple task. Communication between subdomains is limited to the flow variables at the subdomain borders. By letting the particles bounce back at flow boundaries (the so-called bounce-back rule), one can introduce complexly shaped (and moving) no-slip walls without losing numerical efficiency. Finally, the intuitive, particle-based picture of the fluid helps in adding additional physics to the system. In the context of multiphase flows it is worthwhile to mention the application of immiscible fluids with surface tension.

Disadvantages of the method are the time step limitation (which is due to the compressibility of the scheme when applied in the incompressible limit), and the use of uniform grids that prohibits local grid refinement. There are various strategies for local grid refinement in LBM. These, however, have not reached a mature level yet.

4.1.7 Immersed boundary methods

A method that is particularly suited for the direct numerical simulation of solid particles suspended in a gas or a liquid is the **immersed boundary method**. One way of tackling the computation of suspended particles would be to solve the Navier-Stokes equations in the time-dependent fluid domain subject to the no-slip condition at the interfaces with the solid objects. This, however, implies adapting the mesh to the varying positions of the particles during the course of the simulation and leads to a substantial computational cost. In order to

avoid frequent re-meshing, the flow equations can instead be solved on a fixed grid while the presence of the solid bodies is imposed by means of adequately formulated source terms added to the Navier-Stokes equations. This class of techniques is termed “fictitious domain methods”. One of the precursors, the immersed boundary (IB) method of Peskin (1977), was originally conceived for flows around flexible membranes, specifically the flow in the human heart. The basic idea is to determine a singular force distribution at arbitrary (Lagrangian) positions and to apply it to the flow equations in the fixed reference frame via a regularized Dirac delta function. At the same time, the membrane is moving at the local flow velocity. The additional force term for this problem is simply a function of the deformation of the membrane and of its elastic properties. The careful design of Peskin’s delta function is vital to the efficiency of the method. This method has been adapted by Uhlmann (2005) for the simulation of flows with upto 10^3 rigid particles. A further introduction to the immersed boundary method can be found in the reviews of Peskin (2002) and Mittal and Iaccarino (2005).

Example of DNS: Oblique coalescence of two bubbles

To demonstrate the capabilities of DNS models incorporating the interface dynamics, the following example is given. This example involves the oblique coalescence of two gas bubbles in an initially quiescent liquid where the bubbles are initially spherical with their centres separated by three bubble radii in the vertical direction. The position of the lower bubble is shifted off-center to the right (x-direction) over 1.6 bubble radii. In **Error! Reference source not found.**1 the computed evolution of the bubble shapes is shown together with photographs of the experimentally observed bubbles shapes just before and after the coalescence process. The Morton and Eotvos number for this case are respectively equal to 2.10^{-4} and 16 (based on the individual bubbles) which, according to the Grace diagram, would correspond with a terminal Reynolds number of 50, which agrees reasonably well with the experimental value of 43 and the computed value of 40. The leading bubble behaves as an isolated bubble although its major (vertical) axis attains a small angle with the (vertical) z-axes when the trailing bubble enters its wake region. The trailing bubble catches up with the leading bubble and experiences considerable shape deformation when it enters the wake region of the leading bubble which is in excellent agreement with the experimental observations. The liquid phase velocity map is shown for the central (vertical) plane cutting through the column just before coalescence of the bubbles commences. In this case the velocity field is clearly asymmetrical.

t = 0.000 s t = 0.025 s t = 0.050 s

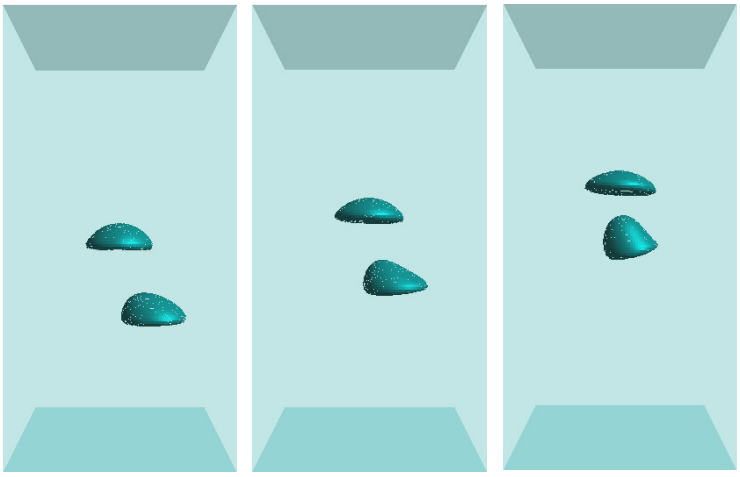

t = 0.100 s

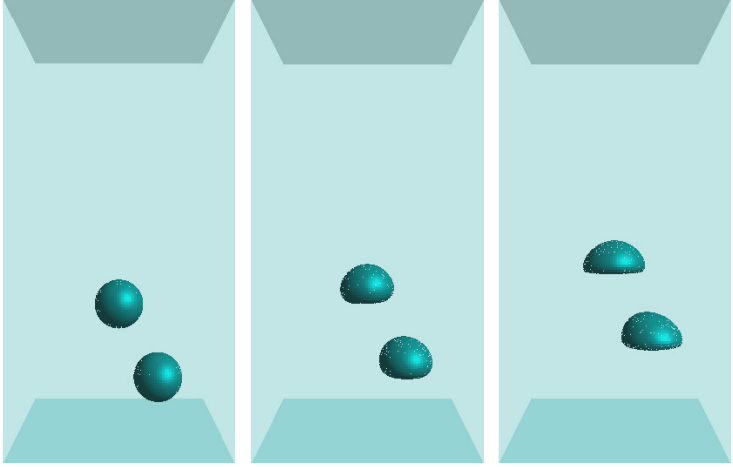

t = 0.075 s
t = 0.125 s

t = 0.150 s

t = 0.175 s

t = 0.200 s

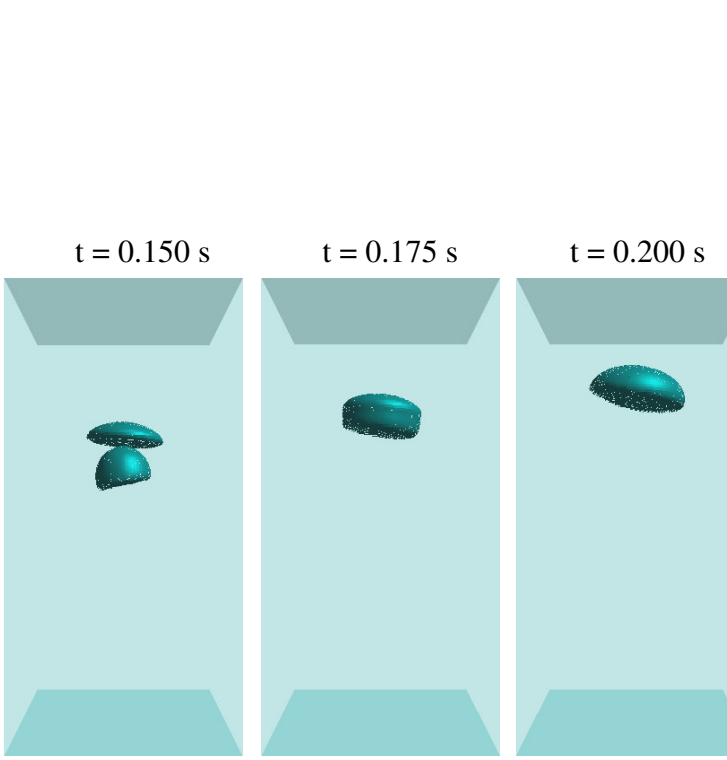

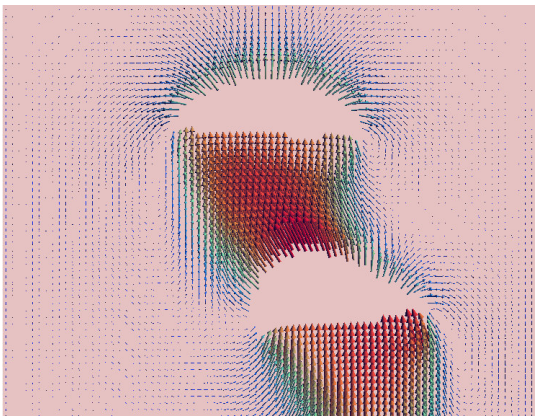

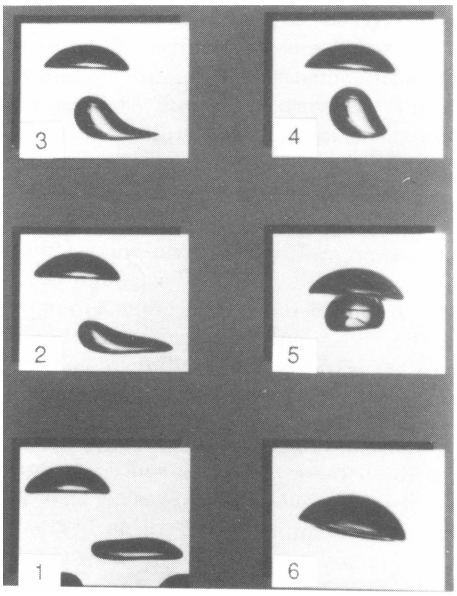

Figure 4.1: Snapshots at different times of the oblique coalescence of two initially spherical bubbles of 0.010 m diameter released from positions (0.020 m, 0.020 m, 0.025 m) and (0.028 m, 0.020 m, 0.010 m) in an initially quiescent liquid in a square column of 0.04 m x 0.04 m x 0.08 m, using a 80x80x160 grid and a time step of 5.10^{-5} s. Eo=16 and M=2.10^{-4}. Included are a liquid phase velocity map in the central vertical plane at t=0.100 s and the photographs (time difference between subsequent photographs is 0.03 s) taken from Brereton and Korotney (1991).

4.2 Discrete Phase Model (DPM)

Discrete element models (DEM) have been used for a wide range of applications involving particles (see for example the book of Ristow, 2000 and the references therein) ever since it was first proposed by Cundall and Strack (1979). A major difference with these traditional DEM models is that a detailed description of the gas phase dynamics is required, in order to describe the interaction between the particles and the surrounding fluid. The coupling of the DEM with a finite volume description of the gas phase based on the Navier Stokes equations was first reported in the open literature by Tsuji et al. (1993) and Hoomans et al. (1996) for the soft-sphere model and the hard-sphere model respectively. Discrete element models for the description of gas-particle flows is often referred to as discrete phase models (DPM).

Generally, two approaches exist in treating the interaction between discrete elements, i.e. the hard sphere and the soft sphere approach.

4.2.1 Framework of the collision model

Hard sphere approach. In a hard-sphere system the trajectories of the particles are determined by momentum-conserving binary collisions. The interactions between particles are assumed to be pair-wise additive and instantaneous. The collisions are processed one by one according to the order in which the events occur. For not too dense systems, the hard-sphere models are considerably faster than the soft-sphere models. Note that the possible occurrence of multiple collisions at the same instant cannot be accounted for.

Campbell and Brennen (1985) reported the first hard-sphere discrete particle simulation used to study granular systems. Since then, the hard-sphere models have been applied to study a wide range of complex granular systems. Hoomans et al. (1996) used the hard-sphere model, in combination with a CFD approach for the gas phase conservation equations, to study gas-solid two-phase flows in gas-fluidized beds. Effect of the gas turbulence is described in section 4.5.

Soft sphere approach. In more complex situations, the particles may interact via short or long-range forces, and the trajectories are determined by integrating the Newtonian equations of motion. The soft-sphere method originally developed by Cundall and Strack (1979) was the first granular dynamics simulation technique published in the open literature. Soft-sphere models use a fixed time step and consequently the particles are allowed to overlap slightly. The contact forces are subsequently calculated from the deformation history of the contact using a contact force scheme. The soft-sphere models allow for multiple particle overlap although the net contact force is obtained from the addition of all pair-wise interactions. The soft-sphere models are essentially time-driven, where the time step should be carefully chosen in the calculation of the contact forces. The soft-sphere models that can be found in literature mainly differ from each other with respect to the contact force scheme that is used. A review of various popular schemes for repulsive inter-particle forces is presented by Schäfer et al. (1996). Walton and Braun (1986) developed a model which uses two different spring constants to model the energy dissipation in the normal and tangential direction respectively.

In the force scheme proposed by Langston et al. (1994), a continuous potential of an exponential form is used, which contains two unknown parameters: the stiffness of the interaction and an interaction constant.

A 2-D soft-sphere approach was first applied to gas-fluidized beds by Tsuji et al. (1993), where the linear-spring/dashpot model similar to the one presented by Cundall and Strack (1979) was employed. Kawaguchi et al. (1998) extended this model to three dimensions as far as the motion of the particles is concerned. Based on the model developed by Tsuji et al. (1993), Iwadate and Horio (1998) and Mikami et al. (1998) incorporated van der Waals forces to simulate fluidization of cohesive particles. The soft-sphere model has been coupled to models describing mass transfer and chemical reactions to study the decomposition of ozone on catalyst coated particles in a 2D fluidized bed by Limtrakul et al. (2004). Kuwagi et al. (2000) coupled the soft-sphere model with a model for the description of metallic solid bridging by surface diffusion mechanisms including the effect of surface roughness.

4.2.2 Interfacial interactions

Particle-particle interaction. It is well known that the formation of heterogeneous structures in fluidized beds can be attributed to a combination of the inelasticity of the particles and the strong non-linear dependency of the drag force on the porosity (Li and Kuipers, 2005). Hoomans et al. (1996) were among the first to investigate the effect of the particle collision properties on the fluidization behaviour. They found that even for slightly inelastic particles, the dissipation of energy resulting from particle-particle collisions could give rise to heterogeneous structures. Due to the loss of energy during the collisions, the involved particles tend to cluster, forming dense regions next to dilute regions (i.e. bubbles).

As mentioned earlier, it is usually assumed that particle-particle collisions are impulsive events that do not depend on the local flow field of the continuous phase. This assumption is only true in case the inertia of the continuous phase is negligible compared to that of the dispersed phase, which is the case for most of the contributions discussed in this work, in which the continuous phase is a gas. However, Zhang et al. (1999) have shown that the collision models as presented in the previous section need to be adapted when the continuous phase is a liquid, in order to account for the drainage of the fluid between the colliding particles and the acceleration of the fluid surrounding the particles. The adaptations of the discrete particle model as proposed by Zhang et al. (1999) involve two additional forces, i.e. the virtual or added mass force and the pressure force. When these two forces are incorporated, the strong influence of the liquid surrounding the particles on the particle trajectories before and after the collision can be faithfully captured, as shown in Fig. 4.2. The closures for the close-distance interaction proposed by Zhang et al. (1999) were successfully used by Li et al. (1999, 2001) and Zhang et al. (2000a-b) in the two-dimensional VOF-DPM model for the hydrodynamic description of the particulate phase in a three-phase gas-liquid-solid flow. An extension of this approach to three dimensions was given by Chen and Fan (2004) who used a level-set method for the description of a large bubble and a discrete particle model for the description of the particles.

Gas-particle interaction. Various investigations of the closure relations for the drag force in the framework of continuum models have demonstrated that the choice of the drag closure has a significant impact on the resulting flow phenomena (see for instance Van Wachem, 2001, Ibsen, 2002, Andrews et al., 2005, Van der Hoef, 2005 and Beetstra et al., 2006). As indicated earlier, continuum models need closure models for both the drag force and the rheological properties of the particulate phase. One can only faithfully validate closure models for the drag force if and only if the rheological properties of the particulate phase are accurately known. Given the current limitations in the predictive capabilities of the two-fluid model employing the kinetic theory of granular flow (Bokkers, 2005), it is much more worthwhile to use the DPM to validate closure models for the drag force since this model

does not require closures for the rheological properties of the particles, which could give rise to anomalous behaviour.

Link et al. (2005) has tested several drag closures in the DPM to assess their suitability to describe the particle dynamics in a pseudo-2D spout-fluid bed and compared the results with detailed particle image velocimetry measurement data. They compared time-averaged particle flux profiles and pressure drop fluctuations at different operating regimes for the following drag closures:

- The most frequently used drag model in literature, i.e.the Ergun (1952) equation for $\varepsilon_g < 0.8$, and the Wen and Yu (1966) equation for $\varepsilon_g > 0.8$.

- The least value of the Ergun (1952) and Wen and Yu (1966) equations, i.e. $F = \min(F_{Ergun}, F_{Wen\&Yu})$.

- The drag relation derived from lattice Boltzmann simulations by Hill et al. (2001).

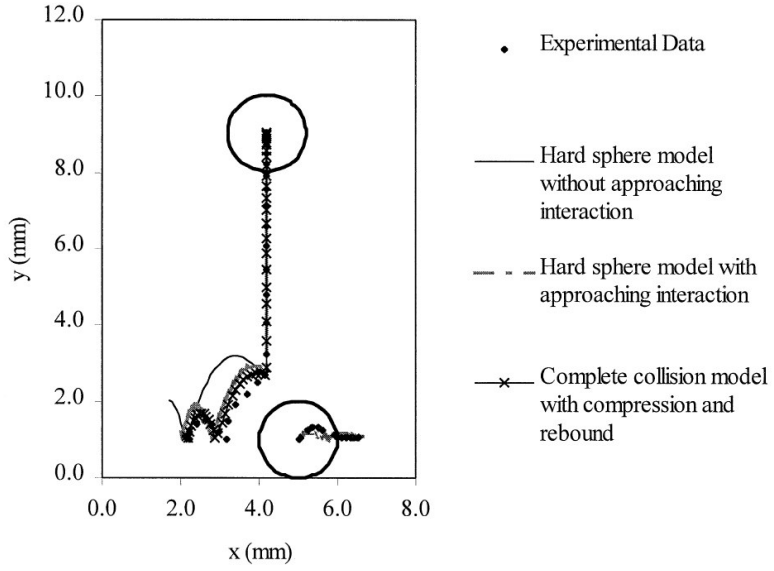

Figure 4.2: Experimental and simulation results of trajectories of two colliding particles (taken from Zhang et al., 1999).

As can be seen in Figure 4.3, the first model produces unsatisfactory results for the shape of the vertical particle flux profiles $\Phi_{p,z}$ for fluidized beds with stable high velocity jets, as encountered in spout-fluid beds. The usage of the minimum of the drag given by the relations of Ergun (1952), and Wen and Yu (1966), as well as the relation proposed by Hill et al. (2001) considerably improves the predictions of the DPM, although Link et al. (2005) found that the computed frequency of the pressure drop fluctuations is still somewhat too high.

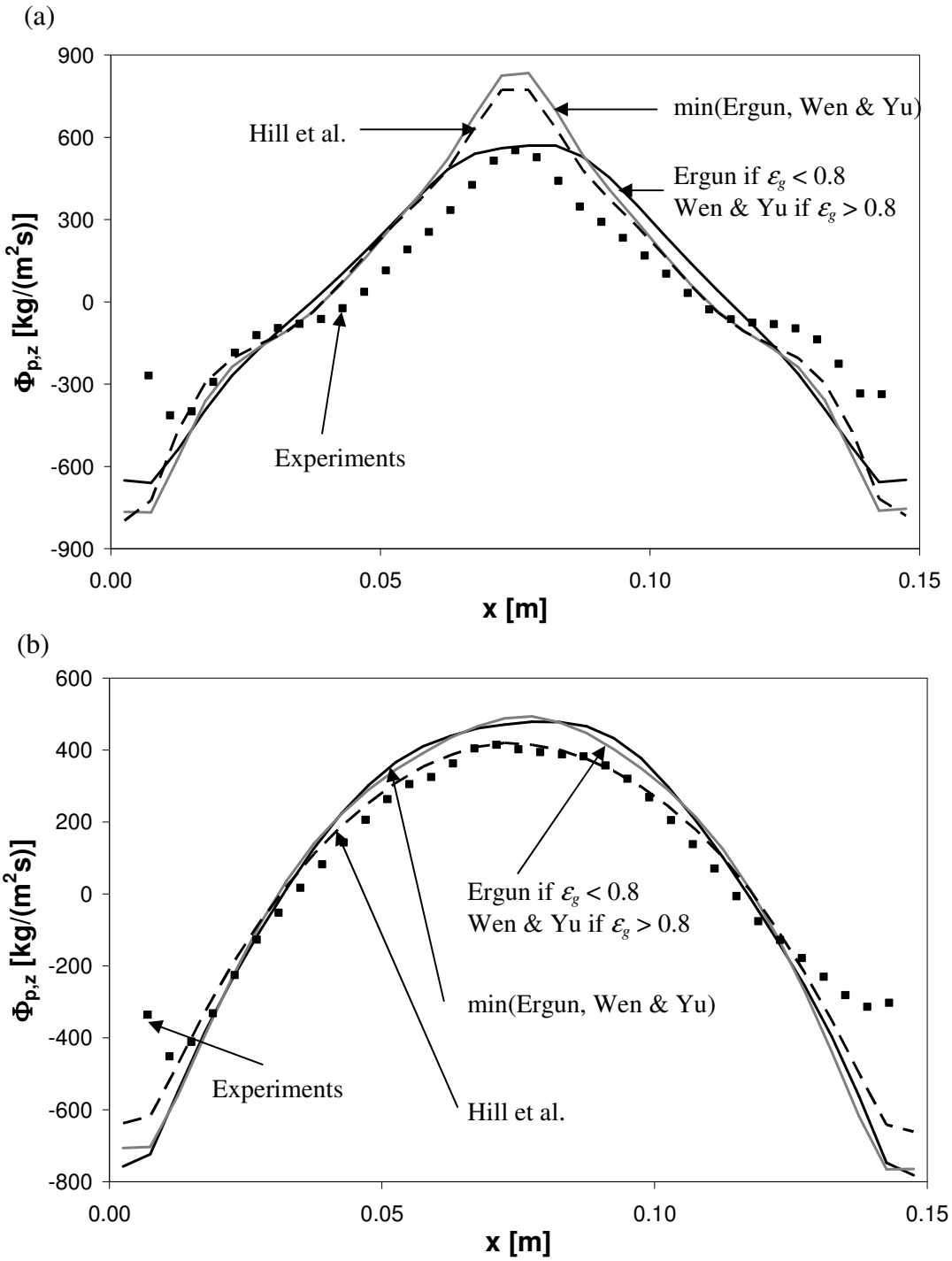

Figure 4.3: Measured and computed vertical time-averaged particle flux profiles for two different regimes using several drag closures (taken from Link et al., 2005). (a): Spout-fluidization, Ufluidization = 1.2 × Umf; Uspout = 23 × Umf , (b): Jet in fluidized bed, , Ufluidization = 2.3 × Umf; Uspout = 16 × Umf.

Examples of the Discrete Phase Model

Flow phenomena in bubble columns

Darmana et al. (2005) investigated the hydrodynamics of the gas-liquid flow in a square bubble column using a discrete bubble model. Air is injected into an initially quiescent liquid as indicated in Figure 4.1. Shortly after the bubbles are released into the column, a bubble

plume rises through the column and creates a typical mushroom like shape. Due to the gas-liquid momentum coupling, some motion is induced in the liquid phase, and after a while the entire bulk liquid starts to move. The first bubbles escape from the column after 1:5 s simulations. After some time the motion inside the bubble becomes unstable. Strong circulation patterns appear with up flow in the centre region and down flow in the corners of the column. Due to the liquid down flow, some bubbles close to the wall are dragged downwards to the lower region of the column before being dragged again to the column surface by the upward flow. The bubble plume is meandering in a random fashion. Using animation representation of our simulation results as suggested by Delnoij et al. (1997) we can see that this meandering behaviour is due to random formation of vortices close to the column surface. The vortices generate strong down flow, which pushes the bubbles near the inlet region to one side when they reach the bottom of the column. The bubble plume will then move close to one side of the column. This process is repeated, but the vortex formation appears in another location, which will make the bubble plume move in another direction. The observed behaviour is in good agreement with the experimental observations of Deen et al. (2001).

A more quantitative comparison with the experimental measurement is obtained through the long term (i.e. the statistical averaged) quantities. In the present study the time-averaged mean velocity and velocity fluctuations of the simulation are calculated during a 110 s interval. The time averaged quantities are compared with the PIV measurements of Deen et al. (2001), who also conducted two fluid simulations of this column with a two fluid model using the commercial CFD package CFX. **Error! Reference source not found.** shows the profile of the average liquid velocity in the vertical direction along with the liquid phase vertical and horizontal velocity fluctuations. As can be seen in this figure, the simulation results show good agreement with the experimental data.

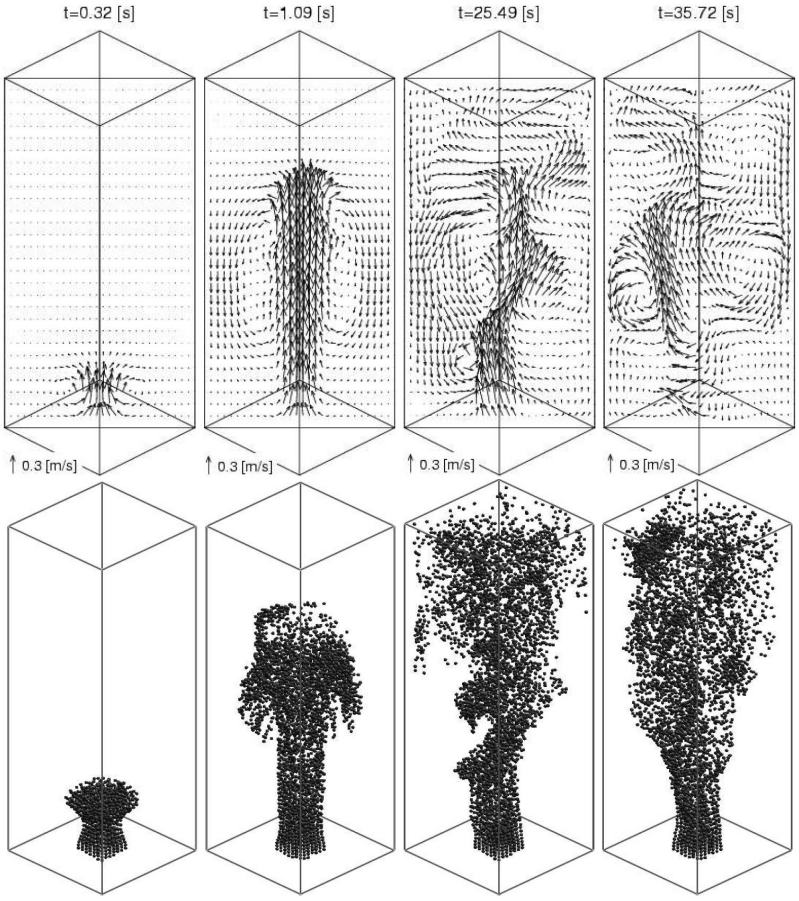

Figure 4.1.: Series of corresponding velocity fields and bubble position obtained from simulation of air-water bubble column at different time after the air was switched on. Gas superficial velocity = 4.9 mm/s.

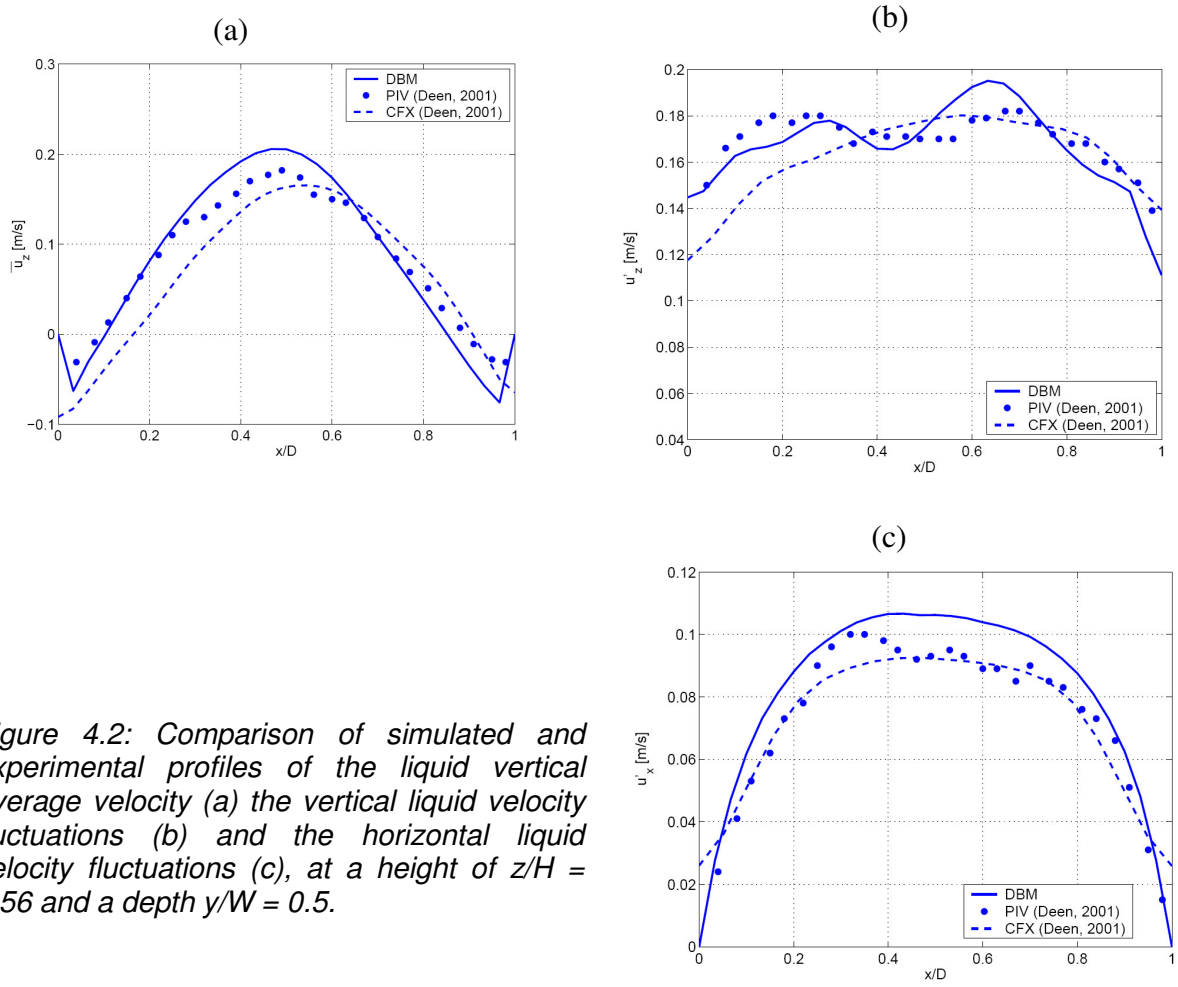

Figure 4.2: Comparison of simulated and experimental profiles of the liquid vertical average velocity (a) the vertical liquid velocity fluctuations (b) and the horizontal liquid velocity fluctuations (c), at a height of z/H = 0.56 and a depth y/W = 0.5.

Flow phenomena in fluidized beds

In this section we will discuss some of the recent applications of the DPM in the framework of research on the flow phenomena prevailing in fluidized beds. Many of the unique properties of gas-fluidized beds can be directly related to the gas bubbles behaviour and therefore it is of crucial importance to assess the capability of the Euler-Lagrange model (DPM) to predict bubble formation and propagation in dense beds. Bokkers et al. (2004) studied the evolution of the bubble size and shape in time of a single bubble injected with a central jet into a fluidized bed, kept at minimum fluidization conditions via a porous plate distributor, with the use of a high speed digital camera. Experiments were performed in a flat bed (0.30 m × 0.015 m × 1.00 m; 0.015 m jet width), with spherical glass beads of 2.5 mm diameter, fluidized with air. The initial bed height was 0.22 m, the background velocity was set at 1.25 m/s and the jet velocity and pulse duration were 20 m/s and 150 ms. Further details about the experimental set-up can be found in Bokkers et al. (2004). In Figure4.634.6 snapshots of the bed at different moments in time after bubble injection are presented and compared with simulation results obtained with the DPM using a 40×80 grid (handling the particle dynamics fully 3D, while approximating the gas phase as 2D). For the purpose of

reference, the results of a two-fluid model (TFM) based on the kinetic theory of granular flow (Goldschmidt et al., 2004) using a 60×120 grid, employing a time step of 10^{-5} s are included. The restitution coefficient for particle-particle collisions was 0.97.

Both models capture the interaction of the particles with the jet: particles in the wake of the bubble are dragged into the centre of the bubble, although this effect seems to be slightly overestimated by the TFM. Additionally, the raining of the particles through the roof of the bubble is predicted by the simulations. Both the DPM and TFM predict a slightly larger bubble size compared to the experiments for both beds, which can be attributed to the implemented equations for gas-particle drag (Ergun, 1952 and Wen and Yu, 1966 drag closures).

A somewhat better correspondence with experiments was obtained (see Bokkers et al. 2004) with new gas-particle drag closures derived from Lattice-Boltzmann simulations (Hill et al., 2001; van der Hoef et al., 2005). Similar results were obtained for systems with different particle diameters and fluidization velocities. Concluding, the bubble size and shape for a single bubble injected into a bed at minimum fluidization conditions can be well described with the DPM and TFM, which provides a good basis to apply the DPM to more complex situations. The differences between the DPM and the TFM can best be observed from **Error! Reference source not found.**4.7, which shows the particle mixing patterns induced by the passage of a single bubble through two initially completely segregated layers of particles of different colour. The DPM shows good correspondence with the experimental observations, whereas the TFM largely over predicts the mixing. This is caused by the fact that the KTGF only accounts for binary collisions between two particles, where friction between the particles is not included. Omitting friction between the particles and the corresponding additional dissipation of granular energy might result in an under-prediction of the shear viscosity of the solids phase.

.

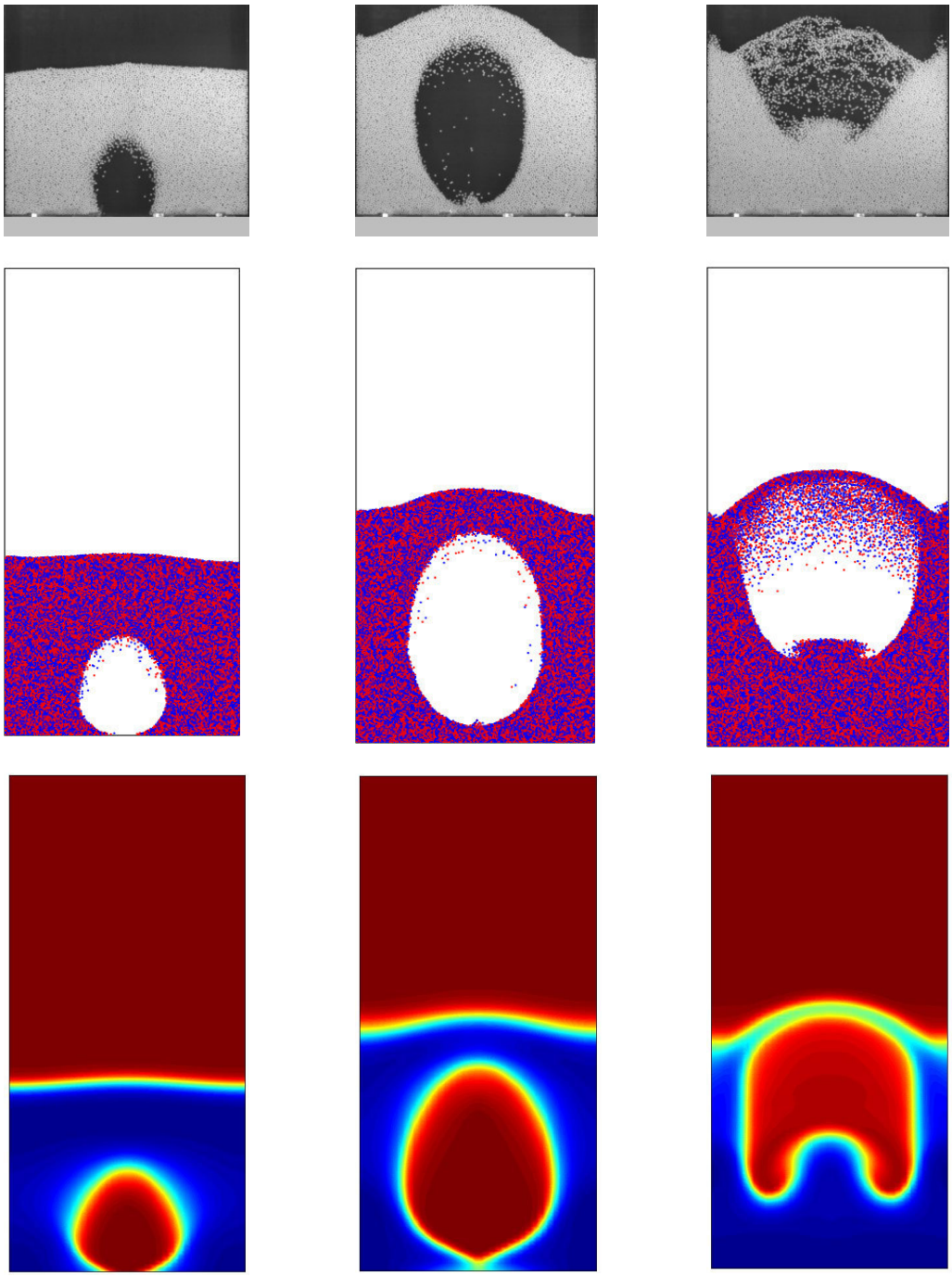

Figure4.63: Injection of a single bubble into the centre of a mono-disperse fluidized bed (bed width: 0.30 m), consisting of spherical glass beads of 2.5 mm diameter at incipient fluidization conditions. Comparison of experimental data (top) with DPM (centre) and TFM (bottom) simulation results for 0.1, 0.2, and 0.4 s after bubble injection (taken from Bokkers, 2005).

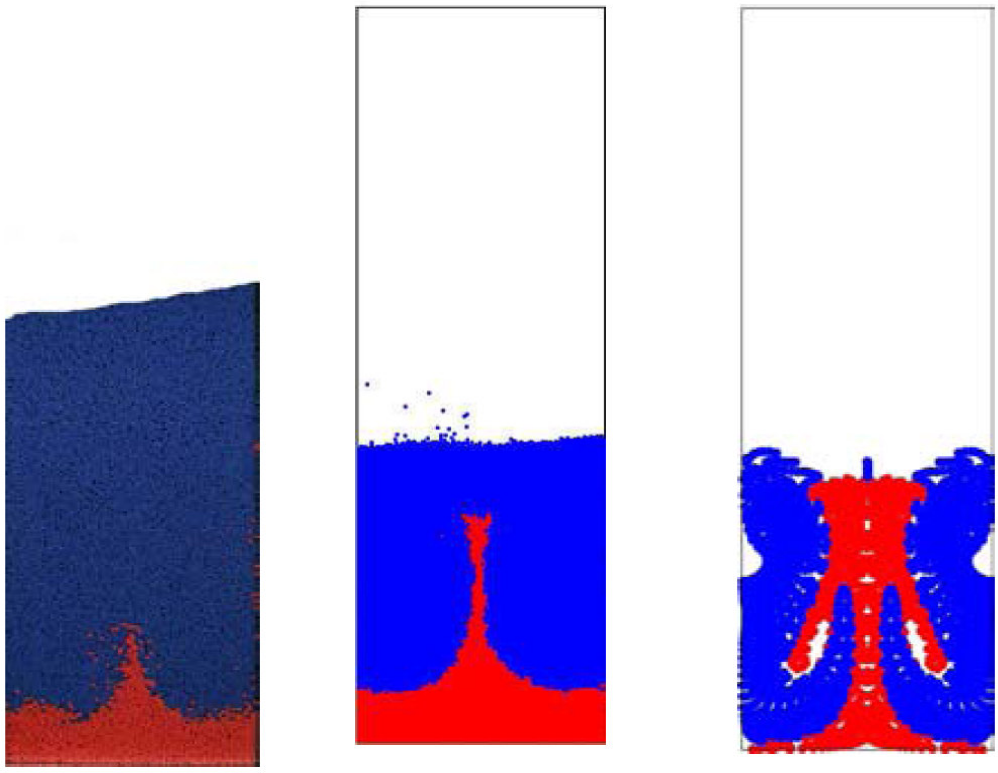

(a) (b) (c)

Figure 4.7: Mixing patterns of a colored under-layer of particles (d_p = 2.5 mm) induced by a single bubble: (a) experiment; (b) discrete particle model (c) two-fluid model

4.3 Point-particle DNS and LES

The object of Eulerian-Lagrangian numerical simulations is to accurately predict turbulent dispersed flows, for instance in channels or pipes. The accuracy of the numerical prediction strongly depends on the particle-particle interactions (collisions and hydrodynamic coupling) and on the particle-turbulence interactions (one- or two-way coupling). If the particle concentration is low enough such that these interactions can be neglected, the dilute flow condition applies. In particular, if the mass fraction of the dispersed phase is very small, then the influence of the particles on the flow can be neglected: this is known as one-way coupling.

In this section, we provide guidelines for Eulerian-Lagrangian Direct Numerical Simulation (DNS) and Large-Eddy Simulation (LES) of particle-laden dilute flow systems where collisions and hydrodynamic interactions can be neglected and a one-way coupling between the dispersed and the carrier phase can be assumed: in this type of flow, particles are simply dispersed by the carrier phase. The discussion is limited to non-reactive, isothermal and incompressible flows governed by the Navier-Stokes equations and a mono-dispersed phase of N_p small heavy particles.

4.3.1 Point-particle approach

In principle, accurate numerical simulations would require the knowledge of the detailed flow

around every particle (fully-resolved simulations, see Figure 4.4(a). In turn, this would require specific no-slip boundary conditions imposed at the surface of each particle in addition to the global initial and boundary conditions. Currently, advances in the computational power have allowed fully-resolved simulations up to $O(10^3)$ particles in simple three-dimensional geometries. Particle samples of this size, however, are still orders of magnitude below the number of particles characteristic of industrial and environmental turbulent flow fields. Fully-resolved simulations with a large-enough number of particles (say, at least $O(10^5)$ in simple reference geometries like channels or pipes) are impracticable with the computer resources available today or foreseeable in the near future. To make simulation of these flows computationally feasible, the requirement on the resolution of the flow around each particle must be relaxed; without full resolution, the forces (and the torques) required to compute the motion of the particle can not be directly computed at the particle surface. An alternative simulation strategy is to treat particles as pointwise rigid spheres and to use a Lagrangian particle equation of motion to model their interaction with the carrier phase (point-particle simulations).

Standard numerical simulations of the flow field for a Newtonian fluid one-way coupled with the particles use the continuity and Navier-Stokes equations:

$$\nabla \cdot u = 0, \tag{99}$$

$$\rho\left[\frac{\partial u}{\partial t} + (\nabla u)\cdot u\right] = -\nabla P + \mu\nabla^2 u, \tag{100}$$

where u is the fluid velocity, P is pressure, ρ and μ are fluid density and viscosity, respectively. When dealing with tracking of point-particles having constant mass, Eqs. (99) and (100) must be solved together with the Lagrangian equations for the trajectory of individual particles, labelled with subscript p :

$$\frac{dx_p}{dt} = v_p, \tag{101}$$

$$m_p \frac{dv_p}{dt} = \sum F(u, v_p, t), \tag{102}$$

where m_p is the mass of the particle and v_p is the mass of the particle. The term $\sum F$ represents the total force exerted by the fluid on the particle and includes body forces (gravitational force), surface forces from surrounding fluid (for instance, drag and lift) and impulsive forces from wall or from other particles (collisions): the reader is referred to Chapter 3 of these Guidelines for further details. Eqs. (99) and (100) are exactly the same as for the single-phase flow and Eqs. (100) and (102) are uncoupled. This means that the two-phase problem simply requires the use of an algorithm for tracking the individual particles in addition to the solution of the single-phase flow..

The point-particle approach imposes a severe restriction: the particle has to be much smaller than the grid cell. This restriction comes from the fact that the velocity u used in Eq. (102) to calculate the force F is the (undisturbed) fluid velocity at the centre of the particle. Since this velocity is obtained by interpolation of the fluid velocity in the neighbouring points, accurate estimate requires that the grid cell is significantly larger than the particle. The accuracy of the fluid flow simulation, however, requires a grid cell significantly smaller than the fluid scales one wants to solve: if the particles are much smaller than the smallest relevant

flow scales, than the point-particle restriction is satisfied (see Figure 4.4(a)). In the case of DNS, this requires particles much smaller than the Kolmogorov length-scale.

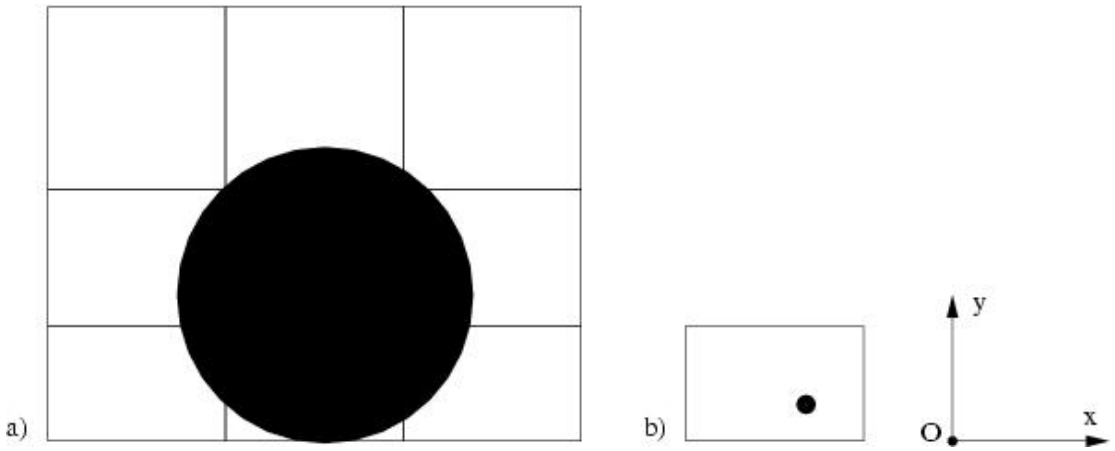

Figure 4.4: Particle size versus grid cell: (a) fully-resolved simulation, (b) point-particle simulation.

However, in most situations this is not the case. In one-way coupling simulation, where the fluid surrounding the particle is not disturbed by the particle itself, violation of the above restrictions on particle size may introduce significant errors. For heavy particles in gas flows, with a Stokes number (defined in section 3.8) much larger than one, the time scale of the particles is significantly larger than the time scale of the small scales of the fluid: due to their inertia, the particles act as low-pass filters and are driven mostly by the large scales. The error introduced by a small grid cell is not important and may be neglected; the only consequence being that the particles experience a local flow field with smaller scales than the ones that are forcing the actual particles (Portela and Oliemans, 2003).

Additional issues with point-particle LES.

DNS is limited to low Reynolds numbers, while the simulation of turbulent flows at higher Reynolds numbers can be tackled using Large-Eddy Simulation (LES). The governing equations are typically of the form:

$$\nabla \cdot \overline{u} = 0, \tag{103}$$

$$\rho\left[\frac{\partial \overline{u}}{\partial t} + (\nabla \overline{u}) \cdot \overline{u}\right] = -\nabla P + \mu \nabla^2 \overline{u} + \rho \nabla \tau, \tag{104}$$

where u is the filtered fluid velocity and τ is the Sub-Grid Scale (SGS) stress representing the effect of the sub-grid scales (SGS) on the resolved eddies (which is modelled). As for the fluid dynamic part, the closure problem of LES equations has been deeply investigated and several SGS models have been proposed and tested. However, since only u is available from LES, while the particle motion depends on the actual fluid velocity, a closure model may be needed to reintroduce the SGS velocity fluctuations, namely to reconstruct the velocity field u from the knowledge of its filtered value u.

In most simulations, the particle velocity is assumed to be driven by the resolved velocity in Eqs. (103) and (104). This assumption is justified in most applications in which particles have material density much larger than that of the carrier flow. Neglecting of the contribution of the SGS velocity fluctuations to particle transport can be an important source of error in the simulations, particularly for particles with small response time, which are more responsive to

the SGS motions occurring on smaller time scales. A measure relevant to this error is comparison of the smallest resolved time scale defined in terms of filter width $\overline{\Delta}$, typically based upon the size of the grid, and velocity scale used in specification of the eddy-viscosity $\overline{\Delta}|\overline{S}|$, i.e. $T = 1/|\overline{S}|$ (Wang and Squires, 1997). When T becomes comparable to the particle response time, the SGS velocity fluctuations are expected to have a measurable effect on deposition.

Simple models for the SGS velocity field typically solve for the particle motion equation using the resolved velocity component directly available from the LES plus a sub-grid fluctuation, u', determined by solving an additional transport equation for the SGS kinetic energy, q^2 (*e.g.* Wang and Squires, 1997). The solution of such equation yields the magnitude of q^2, from which u'^2 can be obtained. The fluctuation is than scaled by random numbers sampled from a Gaussian distribution.

4.4 Euler/Euler (Two-Fluid) method

The Euler-Euler or two-fluid modelling treats the dispersed multiphase flow as two (or more, but the discussion will be limited to only two phases for clarity) interpenetrating quasi-fluids. In this approach both phases will be present at the same place at the same time. A key-quantity is the volume fraction, which determines what the relative amount of a phase is at a given place at a given time.

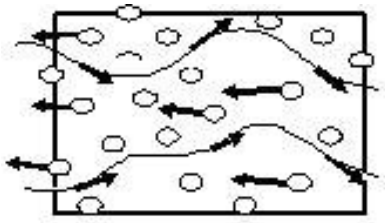

Figure 4.5: Averaging volume for two-fluid formulation.

By their very nature, Euler-Euler models provide an averaged description of the multiphase system. The equations can be constructed in a number of ways: via time-averaging, volume averaging or ensemble averaging (see e.g. Biesheuvel and Van Wijngaarden (1984), Drew (1983), Ishii (1975), Anderson and Jackson (1967)). An advantage of the formulation is that the interfacial forces are inherently present in the modelling. Moreover, the model results in a double set of conservation equations: one set for each phase. Hence, the computational load does not depend on the number of dispersed particles. This makes the two-fluid model the preferred candidate for large systems.

However, a price needs to be paid for averaging. The disadvantage of the two-fluid model is loss of details due to the averaging. This creates closure problems, similar to those in single phase RANS modelling. For the two-fluid model, not only the turbulence needs to be modelled, but also the averaged form of all types of interactions. Note that this stress is not one-to-one coupled to turbulence: it also encompasses the details of the flow around the individual particles that are lost in the averaging.

Because of the averaging procedure required to derive the two-fluid equations, a DNS of a laminar flow is not possible. The small-scale fluctuations attached to the velocity difference between the two phases are modelled in an average sense: they cannot be resolved, no matter how fine the grid is made.

Intuitively, it might be easiest to think of the two-fluid model in terms of volume averaging.

A ‘cubic control volume’ within the flow is pictured, in which both phase are present. The local, instantaneous equations, i.e. the Navier-Stokes equation for the continuous phase and the equation of motion for the particles phase (which may be another set of Navier-Stokes equations e.g. for the case of bubbles), are averaged over the control volume. It will be clear, that the averaged quantities are treated as continuous variables in the two-fluid model. This, however, does only make sense if the scale at which these quantities are defined is much larger than both the particle size and the particle-particle distance and much smaller than the size of the flow domain. Note that using ensemble averaging does relax these requirements.

When averaging the local, instantaneous equations the result is averaged quantities (subscript c and d are used for the continuous and dispersed phase, respectively). For instance, consider the local, instantaneous velocity of the continuous phase: $v_c(t,x)$. After averaging, the theory will use $\langle v_c \rangle(t,x)$. The difference between these two, is that the former only exists when continuous phase is present at (t,x), whereas the latter is a smooth, continuous function of space and time, defined over the entire flow domain. As a consequence, the difference between the two, associated to the fluctuations of the velocity of the continuous phase should be defined:

$$v_c' \equiv v_c(t,x) - \langle v_c \rangle(t,x). \qquad (105)$$

By definition, the average of this fluctuating part is zero. However, this does not hold for non-linear combinations of the fluctuations, e.g. $\langle v_c' \, v_c' \rangle \neq 0$, in general.

The two-fluid equations, for a system without chemical reactions and phase changes, read in its general form as:

$$\frac{\partial}{\partial t}\alpha_k \rho_k + \nabla \cdot \alpha_k \rho_k \vec{v}_k = 0, \qquad (106)$$

$$\frac{\partial}{\partial t}\alpha_k \rho_k \vec{v}_k + \nabla \cdot \alpha_k \rho_k \vec{v}_k \vec{v}_k = -\alpha_k \nabla p - \nabla \cdot \left(\alpha_k \vec{\vec{\tau}}_k + \alpha_k \vec{\vec{\tau}}_k^{\,\mathrm{Re}} \right) \pm \vec{F}_k + \alpha_k \rho_k \vec{g}, \qquad (107)$$

with k={c,d} denoting the continuous or dispersed phase, the brackets for mean quantities have been left out for clarity. $\vec{F}_k$ denotes the mutual interaction force between the phases (hence has a +sign in the balance of phase k and a –sign in the other). Further, $\vec{\vec{\tau}}_k^{\,\mathrm{Re}}$ denotes the (Reynolds) stress due to the fluctuations at the boundaries of the control volume.

4.4.1 Two-fluid model: closure and simplifications

A number of terms in the two-fluid model need to be closed: the Reynolds stress and the mutual interaction force. Moreover, the possibility of (turbulent) eddies effectively transporting the dispersed phase in case of a non-uniform dispersed phase distribution needs to be addressed.

Interfacial forces

A number of interaction forces are identified, apart form gravity and mean pressure, which are discussed in Chapter 3.

From the interaction forces, the drag force is usually the most important. The lift force as well as the turbulent diffusion (here seen as a force) may act in a direction perpendicular to gravity and drag. Thus, although they may be relative small, they can be important.

Turbulent diffusion

The turbulent diffusion is a consequence of the fluctuations in the continuous phase. It is

important to realize, that the drag force is usually formulated in terms of the mean slip velocity. However, for not too small a particle Reynolds number, the drag is not a linear function of the local, instantaneous velocities. Consequently, when averaging the drag, the average of the fluctuating part of the velocities shows up in non-linear combinations which are not equal to zero. Therefore, the drag force should be modelled as a part due to the mean and a part due to the correlation between fluctuations. The drag force can be written as:

$$\vec{F}_D = \alpha_d \rho_c f_D \vec{v}_s, \tag{108}$$

with $f_D = \frac{4}{3}\frac{C_D}{d_p}\left|\vec{v}_s\right|$. Loosely speaking, $\vec{v}_s$ is the slip velocity between the particles and the continuous phase. However, in a two-fluid description this would suggest that it is the difference between the velocity fields $\vec{v}_d$ and $\vec{v}_c$. However, as mentioned this ignores the correlation between the fluctuations. Therefore, the slip velocity also contains a so-called drifting velocity that takes this into account. The effects of turbulence on a non-uniform particle distribution are modelled via this part of the drag force. Bel F'dhila and Simonin (1992) and Viollet and Simonin (1994) write formally:

$$\vec{v}_s = \left[\vec{v}_2 - \vec{v}_1\right] - \vec{v}_d. \tag{109}$$

The drifting velocity needs further modelling, which in the end results in:

$$\vec{v}_d = -D_{12}^t \left[\frac{\nabla \alpha_2}{\alpha_2} - \frac{\nabla \alpha_1}{\alpha_1}\right], \tag{110}$$

with D_{12}^t a fluid turbulent diffusion. Other authors use a more heuristic approach, but arrive at similar expressions.

The lift force is still a difficulty. It can appear in the form of a Magnus type of force, for rotating rigid particles, or as a classical lift due to non-zero shear or vorticity around the particle. Tomiyama et al. (2002) have shown, that the lift coefficient for bubbles in a shear flow may change sign depending on the bubble size. This is important as the classical lift force will push the particles towards the region of low velocity with respect to the particle. A change in sign, obviously does the opposite, changing the particle fraction distribution. This is especially important in case of gravity driven flow. Nevertheless, reasonable results have been reported when neglecting the lift force all together.

Turbulence modelling

The Reynolds stresses need to be closed as well. The k-ε model, with specific multi-phase additions, is the most used model for closure:

$$\vec{\vec{\tau}}_c^{\,\mathrm{Re}} = \mu_c^{turb}\left(\nabla\vec{v}_c + \nabla\vec{v}_c^{\,T} - \frac{2}{3}\nabla\cdot\vec{v}_c\,\vec{\vec{I}}\right) - \frac{2}{3}\rho_c k_c \vec{\vec{I}} \quad \text{with } \mu_c^{turb} = C_\mu \rho_c \frac{k_c^2}{\varepsilon_c}. \tag{111}$$

For the continuous phase a k-ε model is solved, with additional production and dissipation terms that incorporate the effect of the relative velocity between the phases and of a gradient in the dispersed volume fraction (see e.g. Gosman et al. (1992), Bel F'dhila and Simonin (1992), Oey et al. (2003)).

Other options are to use a standard k-ε model, but calculate the turbulent viscosity as the sum

of a (single phase) shear induced part and a bubble-induced part: $\mu_c^{turb} = \mu_{c,SI}^{turb} + \mu_{c,BI}^{turb}$. The latter can be modelled according to Sato et al. (1981), see also Sokolichin et al. (2004).

As an alternative, a complete Reynolds stress model can be used. This is, however, not used frequently, partly because it slows down the simulations tremendously, partly because lack of data to compare the results with.

In recent literature and in some commercial CFD packages, Large Eddy Simulations (LES) have been reported using a two-fluid approach. This gave reasonable results for e.g. a bubbly flow. However, care should be taken: the use of LES in combination with a two-fluid approach requires incorporation of the LES concept right from the start. Using LES as a way to model the 'turbulence' of the continuous phase in the two-fluid framework has at least two difficulties: (1) The governing equations are averaged equations. From the volume averaging it is easily seen, that the size of the averaging 'control volume' may be rather large, i.e. the cut-off for the eddies in terms of LES is at the large to very large scales of the eddy spectrum. It is questionable whether or not the LES modelling, like the Smagorinsky sub grid model, is applicable. (2) In principle, when reducing the grid size, a Large Eddy Simulation should become a DNS simulation. Obviously, due to the averaging, the two-fluid equations do not contain the information about the smaller eddies. Hence, when using small grid sizes the 'turbulent' fluctuations will not be captured.

The turbulence in the dispersed phase can be solved using algebraic relations, that couple the fluctuations in the dispersed phase to those in the continuous phase, see e.g. Simonin (1990) and Viollet and Simonin (1994).

Volume fraction and Reynolds decomposition

Special care should be taken when dealing with the volume fractions. Consider the volume fraction of the dispersed phase, α_d. In a volume-averaged formulation, this is by definition the fraction of the control volume occupied by the dispersed phase. This means that it is defined at the scale of the control volume and is thus an averaged quantity itself. Consequently, it is unnecessary, even inconsistent, to break the volume fraction up in an averaged part and a fluctuating one. The latter does not exist. This has consequences for the mass balances. Consider the mass balance of the dispersed phase (for a system without chemical reactions or phase changes with a constant density of the dispersed phase):

$$\frac{\partial \alpha_d}{\partial t} + \nabla \alpha_d \vec{v}_d = 0. \qquad (112)$$

In this balance there is no diffusive term. In literature, this is sometimes added to account for 'mixing' of the phases due to turbulent fluctuations that act on differences in the volume fraction. To the right hand side of the mass balance a diffusive flux is then added:

$$\frac{\partial \alpha_d}{\partial t} + \nabla \alpha_d \vec{v}_d = -\nabla \left\langle \alpha_d' \vec{v}_d' \right\rangle = \nabla D \nabla \alpha_d. \qquad (113)$$

The second equality uses the well-known analogy between the effects of eddies and kinetic gas theory. However, as discussed $\alpha_d' = 0$. The effect of turbulence on the distribution of the phases shows up in the momentum balances. (see e.g. Simonin (1990), Oey et al. (2003), Sokolichin et al (2004)).

For engineering purposes, the above diffusion term can provide the right amount of 'mixing'. It has the advantage of simplifying the governing equations. This may be important, as the simulations are time consuming and using a number of simplifications may speed up the simulations considerably with sufficient accuracy. However, the use is principally wrong and

care should be taken, as there is no guarantee that the results are accurate enough.

Simplifications

Especially in gravity driven flows, like bubble columns, gravity (and/or buoyancy) and drag are dominating. This opens the possibility of model reduction. For these flows, an important 'first guess' can be made by realizing that gravity and drag are of the same order of magnitude, whereas the other forces are (much) smaller. So, if the inertia of the dispersed phase does not play a role (e.g. for bubbles in a liquid) grosso modo gravity and drag will balance each other. Thus, the velocity of the dispersed phase can to first order be approximated as the some of the continuous velocity plus a slip velocity. The latter is the result of the balancing of drag and gravity. The flow problem can now be simplified, by the following steps:

add the two momentum balances: the interaction forces drop out of the new 'total momentum balance';

replace the particle momentum balance by an algebraic slip relation for the velocity of the dispersed phase: $\vec{v}_d = \vec{v}_c + \vec{v}_s$ with $\vec{v}_s$ specified by an algebraic relation;

replace the dispersed phase velocity in the total momentum balance by the result of step 2, or ignore the contribution of the dispersed phase to the total momentum at all, apart from the influence of gravity (e.g. for bubbles with a low density);

calculate the gas fraction distribution α_d from the mass balance of the dispersed phase using step 2 for the velocity field.

The above is known as the Mixture Model. Step 2 can also be modified by calculating the slip velocity from the pressure gradient. If the flow is governed by buoyancy and drag, the momentum balance for the disperse phase can, in first order, be approximated by $\vec{v}_s = -\frac{\nabla p}{C_D}$.
This approach has been used by Bauer and Eigenberger (1999) and Bauer and Eigenberger (2001).

In many cases it is advised to first try the mixture model to get a 'quick and dirty' impression of the flow field. This approach has the advantage of being faster and providing guidance for more elaborate simulations.

One of the issues discussed above concerns the modelling of turbulent diffusion of the dispersed phase. In principle, this effect should be accounted for via forces in the momentum balances. However, an engineering approach is to ignore it in the momentum equations and mimic the effect as a true diffusion (of the dispersed fraction) in the mass balances. This simplification has been discussed by Sokolichin et al. (1997).

4.4.2 Numerical implementation

The equations of the two-fluid model comprise 2 mass balances, 2*3 momentum balances and if the flow is turbulent a set of k-ε equations or 6 Reynolds stress equations. These partial differential equations are coupled via interfacial forces and a common gas fraction field, making them difficult to solve.

Boundary conditions

Wall

For laminar simulations usually a no-slip condition for the continuous phase is used, while the dispersed phase is allowed to slip freely. If the particles of the dispersed phase are relatively large, the dispersed phase fraction can be set to zero at the walls.

For a turbulent flow, a no-slip condition can only be used if the boundary layer is sufficiently resolved. In a two-fluid approach it is questionable if this can be done: the averaging has excluded small length scales to be resolved. In combination with the use of a k-ε model, a wall function can be used to model the near wall region. Note that the first grid point needs to be outside the viscous sub layer. In single-phase flows, this means in wall units: $y^+>30$, with $y^+ \equiv \frac{y u_\tau}{\nu}$ where y denotes the actual distance from the wall, ν is the kinematic viscosity and $u_\tau \equiv \sqrt{\frac{\tau_w}{\rho}}$ is the wall shear velocity (τ_w denoting the wall shear stress and ρ the fluid density). Due to a lack of proper theory for multiphase wall functions, the standard single-phase wall functions are used. In principle, it is possible to use hybrid methods that allow the grid point closest to the wall to be closer than the above restriction. These ideas, however, rely on the development of the boundary layer as in single-phase flows. It is not known to what extent this holds for multiphase flows.

Inlet

At the inlet usually Dirichlet type of boundary conditions are used for the flow variables. This leaves still options for the velocities of the phases. Either, the local velocity and the volume fractions are specified, or the mass fluxes and the volume fraction are prescribed. This gives inlet conditions for the normal components of the velocities; the tangential ones are usually set to zero.

Outlet

In general outflows are chosen such that the applied conditions cause the least disturbance of the solution in the inner part of the flow domain. No general recipe is available and in many cases it is tried to place the outlet as far away as possible, limiting the possible influence. Neumann conditions can be used when pressure-correction schemes are used, e.g. SIMPLE (Patankar, 1980). As an alternative, for incompressible flows, specification of the normal and tangential stresses leads (according to Sani and Gresho, 1994) to a well-posed problem. For two-phase flows, the tangential velocities are chosen like for a symmetry plane, i.e. zero shear stress for both phases. Additionally, the normal stress components are made zero. The normal velocities are chosen to specify the pressure at the outlet plane. This boils down to setting as condition: $p = C + \rho_l \left(\langle v_n v_n \rangle - \langle v_t v_t \rangle \right)$, with v_n and v_t the normal and tangential component of the continuous velocity and $\langle \bullet \rangle$ denotes a Reynolds stress. Note that for isotropic models the term in brackets is zero and the pressure can be set at any constant value.

Another approach is to model the outlet as an inlet (Ranade and Tayalia, 2001). The liquid axial velocity is set to zero at this boundary and the gas phase axial liquid velocity is set equal to the slip velocity. The gas fraction is not specified, but follows from the simulations.

Symmetry

For symmetry boundaries the normal velocities are set to zero. Furthermore, Neumann conditions (zero normal gradients) are applied to the other quantities.

Free Surface

A free surface can be simulated as a symmetry boundary, provided none of the phases crosses this boundary. However, in case of a bubbly flow with a free surface, the gas phase is allowed to cross the free surface. In principle, this can be simulated by placing the gas outlet downstream of the free surface, i.e. a degassing zone is created that extends above the liquid surface. This mimics the real situation. Gravity will keep the liquid phase down, while the gas phase moves out of the system passing the free surface. Further downstream, the gas will pass an outlet that can be modelled like any single-phase outlet. However, this approach can give several problems. For instance, there is the possibility of a small drag force across the free surface, dragging the continuous phase out of the domain. Although this is usually a small effect, the continuous phase slowly disappears from the system which it does not do in real applications. Secondly, secondary flows may be created during the simulations in the headspace above the free surface. These might even cause a back flow through the free surface into the two-phase region. Obviously, this is not realistic.

To circumvent these shortcomings, the free surface is sometimes treated as a symmetry plane for the continuous phase and a kind of outlet for the dispersed one. For the latter the dispersed phase velocity is sometimes prescribed as the terminal velocity, with the argument that the normal velocity of the continuous phase is zero at the free surface so that the dispersed phase escapes with the slip velocity. Note that in this approach the start up of the simulation is delicate: gas is inputted, but cannot flow out yet as it is only present in the lower part of the domain. The continuous phase cannot escape either as this is forbidden by the free surface modelling. This makes that the mass balances cannot be fulfilled. Numerical diffusion is supposed to take care of this problem until the dispersed phase starts to flow out of the system.

4.5 Euler/Lagrange approach

General framework

Some of the modeling issues related to Euler-Lagrange simulations based on a RANS flow field for the continuous phase are the same as for Euler-Lagrange DNS and LES. Point particles are tracked based on solutions of their equations of motion. The issues of time integration of these equations, and fluid velocity interpolation to the position of the particle for determining the drag force on the particles are very similar to DNS and LES and have been discussed in section 4.4. Additional modeling in RANS-based Euler-Lagrange simulations relates to particle dispersion by the action of turbulence, and to modifications of the continuous phase flow (the average flow and its turbulence characteristics) due to the presence of the particles.

The general form of the conservation equations for an incompressible, steady and three-dimensional flow is given by:

$$\frac{\partial}{\partial x_i}\left(\rho U_i \phi\right) - \frac{\partial}{\partial x_i}\left(\Gamma_\phi \frac{\partial \phi}{\partial x_i}\right) = S_\phi + S_{\phi,\Omega} + S_{\phi,P,m} + S_{\phi,P,ev} \qquad (114)$$

The continuity equation results with $\phi = 1$ and the momentum equations with $\phi = U_i$ where U_i ($i \in [1, 2, 3]$) are the three velocity components. The fluid temperature equation is obtained with $\phi = T$ and also different species conservation equations may be considered (e.g. gas phase and vapour phase). The conservation equations for the turbulent kinetic energy k and the dissipation rate ε are obtained with $\phi = k$ and $\phi = \varepsilon$, respectively. The diffusion coefficients for all the conservation equations are given in Table 4.1 together with the fluid

phase source terms S_ϕ. The term $S_{\phi,\Omega}$ has to be considered in case calculations are performed in a rotating frame of reference and contains the Coriolis and the centrifugal force (Decker and Sommerfeld 2000). The particle phase source terms $S_{\phi,P,m}$ account for the effect of the particles on mean flow and turbulence due to interfacial momentum and heat transfer and $S_{\phi,P,ev}$ is the transfer caused by particle/droplet evaporation. The source terms for the dispersed phase are summarised in Table 4.2 for the different flow variables. The left column provides the source terms due to interfacial momentum and heat transfer and the right column those resulting from droplet evaporation, i.e. mass transfer (Grancher 1990, Sommerfeld et al. 1993). In this case two gaseous species are considered, e.g. air and water vapour. It should be noted that momentum transfer due to evaporation occurs with the particle velocity and in the case of condensation the instantaneous fluid velocity seen by the particle (see Table 4.2) has to be used. The summation of the source terms has to be performed along all particle trajectories (index k) passing through a considered control volume. The sampling procedure for obtaining these source terms from the particle trajectory calculations will be described below in more detail.

ϕ	S_ϕ	Γ
1	-	-
U_i	$\frac{\partial}{\partial x_j}\left(\Gamma_{U_i}\frac{\partial U_j}{\partial x_i}\right)-\frac{\partial p}{\partial x_i}+\rho g_i$	
T	0	
Y_k	0	$\mu/Sc+\mu_t/Sc_t$
k		
ε	$\frac{\varepsilon}{k}(C_1 G_k - C_2\rho\varepsilon)$	

$$G_k=\mu_t\left(\frac{\partial U_i}{\partial x_j}+\frac{\partial U_j}{\partial x_i}\right)\frac{\partial U_i}{\partial x_j}, \qquad \mu_t = C_\mu\ \rho\ \frac{k^2}{\varepsilon}$$

$$C_\mu = 0.09; \quad C_1 = 1.44; \quad C_2 = 1.92; \quad \sigma_k = 1.0; \quad \sigma_\varepsilon = 1.3$$

Table 4.1 Summary of the variables, ϕ, and fluid source terms, Γ, in Eq.(114) and constants of the k-ε turbulence model

ϕ	$S_{\phi,P,m}$	$S_{\phi,P,ev}$
1	0	$\sum_k \left(N_k\ \dot{m}_{k,ev}\right)/V_{CV}$

U_i	$-\sum_k \frac{\dot{m}_k N_k}{V_{CV}} \cdot \left[\left(u_{k,i}^{t+\Delta t} - u_{k,i}^{t} \right) - g_i \left(1 - \frac{\rho_F}{\rho_P} \right) \Delta t \right]$	$\sum_k \frac{N_k \, \dot{m}_{k,ev} \, u_a}{V_{CV}}$
T	$-\sum_k \frac{N_k}{V_{CV}} \left(H_{Lat} \, \dot{m}_k + Q_L \right)$	$\sum_k \frac{N_k \dot{m}_{k,ev}}{V_{CV}} C_{vap}(T_k) \, T_k$
Y_1	0	0
Y_2	0	$\sum_k \frac{N_k \, \dot{m}_{k,ev}}{V_{CV}}$
k	$\sum_i \left(\overline{U_i \, S_{U_i,P,m}} - \overline{U_i} \; \overline{S_{U_i,P,m}} \right)$	$\overline{U_i \, S_{U_i,P,ev}} - \overline{U_i} \; \overline{S_{U_i,P,ev}} + \frac{1}{2} \left(\overline{U_i} \; \overline{U_i} \; \overline{S_{\rho,P,ev}} \right.$
ε	$C_3 \frac{\varepsilon}{k} S_{k,P,m}$	$C_3 \frac{\varepsilon}{k} S_{k,P,m}$
For evaporation: u_a, v_a, w_a = u_k, v_k, w_k For condensation: u_a, v_a, w_a = u, v, w Y_1 : air ; Y_2 : water		

Table 4.2 Summary of particle phase source terms for the different fluid flow conservation equations (left column: interfacial momentum and heat transfer; right column: interfacial mass transfer)

Particle tracking routines as described earlier in this guide for Euler-Lagrange DNS and LES are used in RANS-based Euler-Lagrange-based simulations as well. The time step for the particle tracking calculation should be automatically adjusted along the trajectory by considering all relevant time scales which also are changing throughout the flow field:

the time required for a particle to cross a control volume t_{CV} ,

particle response time

the integral time scale of turbulence T_L,

the average time between inter-particle collisions τ_c.

Hence the time step Δt must be a fraction of the minimum of these time scales for accurate calculations, for example 20%:

$$\Delta t = 0.2 \cdot \min \left(t_{CV}, \tau_P, T_L, \tau_c \right) \quad . \qquad (115)$$

A limitation by the average collision time between particles is necessary in order to ensure that at most only one inter-particle collision can take place during a time step (i.e. binary collisions prevail). This time scale is estimated from the local particle number density N_p, the

maximum relative velocity between particles $\left|\Delta\vec{u}_{p\,max}\right|$ and the mean particle diameter D_{pm}:

$$\tau_c = \frac{1}{\pi\, D_{pm}^2 \left|\Delta\vec{u}_{p\,max}\right| N_p} \qquad (116)$$

The particle phase properties are sampled for each control volume by a combined time (i.e. along the particle trajectory within one control volume) and ensemble averaging in the following way:

$$\overline{f}_P = \frac{1}{t_{samp}} \sum_{k=1}^{k_{tot}} \sum_{n=1}^{n_s} f_{k,n}\, N_k\, \mathrm{D}t_n\, f_{s,n} \quad with: f_{k,n} = u_{Pi}, D_P \qquad (117)$$

and:

$$t_{samp} = \sum_{k=1}^{k_{tot}} \sum_{n=1}^{n_s} N_k\, \Delta t_n\, f_{s,n} \qquad (118)$$

Here, $N_{p,n}$ is the number of real particles in a parcel and $f_{s,n}$ is a factor which takes into account the fraction of the time step Δt_n the particle is moving in the considered control volume. If a particle crosses a cell boundary $f_{s,n}$ becomes smaller than unity. The time averaging along a particle trajectory in a given computational cell is indicated by the summation over n, whereas the sum over k is related to the total number of parcels k_{tot} crossing the considered cell.

The averaged fluctuating velocities of the dispersed phase are obtained from:

$$s_f = \sqrt{\frac{1}{t_{samp}} \sum_{k=1}^{k_{tot}} \sum_{n=1}^{n_s} \left(f_{k,n}^{\,2}\, N_k\, \mathrm{D}t_n\, f_{s,n} - \overline{f_{k,n}} \right)} \quad with: f_{k,n} = u_{Pi} \qquad (119)$$

The particle volume fraction follows from:

$$\overline{\varphi}_p = \frac{\pi}{6} \frac{1}{V_{CV}\, t_{ref}} \sum_{k=1}^{K_{tot}} \sum_{n=1}^{n_s} D_{k,n}^3\, N_k\, \Delta t_n\, f_{s,n} \qquad (120)$$

Here V_{CV} is the volume of the considered cell, and t_{ref} is the total tracking time of the particles.

Particle dispersion

In RANS simulations, information on the turbulence is only available in statistical terms (e.g. turbulent kinetic energy and energy dissipation rate in *k*-ε simulations, Reynolds stresses and dissipation for Reynolds stress models). Simulated particle dispersion in steady-state RANS is the result of random walk models: The continuous phase velocity at the particle location is the sum of the interpolated average velocity, and a random process the intensity and time-scales of which are a function of local turbulent conditions. Via the drag (and possibly other hydrodynamic forces), the continuous phase velocity drives the random walk of the particles.

Random walk models are usually subdivided into continuous and discontinuous or eddy-lifetime models. The latter have been widely used due to simplicity and modest computational demands. The instantaneous velocity of the continuous phase at the particle location is estimated by adding to the calculated mean velocity (obtained via interpolation of the surrounding grid-node velocities) a fluctuating component ($\tilde{u} = U + u$), which obeys a Gaussian probability distribution having zero mean and a variance corresponding to the local Reynolds normal stress (in k-ε modeling the latter is usually based on an isotropy assumption: $\overline{u_i u_i} = \frac{2}{3}k$). A sampled velocity fluctuation remains fixed until the local eddy lifetime has elapsed, implying that during the eddy lifetime the particle interacts with a single eddy.

The Lagrangian autocorrelation function describes how the values of the fluid velocity $\tilde{u}(t)$ are temporally related along the particle trajectory. It is characterized by a Lagrangian integral time scale T_L, which is a rough estimate of the interval over which $\tilde{u}(t)$ is correlated. In most discontinuous random walk models the eddy lifetime is taken $2T_L$, and the autocorrelation function is approximated by a straight line. An alternative way is to sample the eddy lifetime at random from a Poisson distribution based on T_L. The latter approach is more realistic.

The continuous random walk models proposed by Berlemont et al (1990) and Zhou & Leschziner (1991) employ a correlation function which comprises the covariance matrix, computed from the turbulence closure model, and an assumed shape of the temporal correlation function. Whereas the fluid velocity fluctuation in the eddy lifetime concept is taken constant during a specific time interval, the continuous random walk models calculate a new velocity fluctuation at each numerical time step based on the velocity covariance matrix of the Eulerian solution and one or more previous time steps. Although the continuous variant is more sophisticated than the eddy lifetime concept, MacInnes & Braco (1992) show that both models predict an unphysical accumulation of particles in regions with low turbulence intensity.

Langevin models employ Lagrangian stochastic differential equations to compute the instantaneous fluid velocity. The advantage of this approach is that the Langevin model for particle motion can be made consistent with the Eulerian prediction obtained with a turbulence model (Haworth & Pope, 1985). Written as a stochastic differential equation, the Langevin equation reads

$$d\tilde{u}(t) = -\frac{\tilde{u}}{T}dt + \left(\frac{2\overline{u^2}}{T}\right)^{1/2} dW(t) \tag{121}$$

where $W(t)$ is a Wiener process, and the increment in the Wiener process, $dW(t)$ can be thought of as a Gaussian random variable with zero mean and variance dt. For this model, the Lagrangian correlation function is $e^{-t/T}$ and so T is the Lagrangian integral time scale T_L. Note that Eq. (121) has been derived for homogeneous, stationary, one-dimensional situations without a mean flow (Thomson, 1987), and that it exhibits similar weaknesses as random walk models.

Random walk as well as Langevin models require an expression for T_L in terms of known flow properties. This time scale is hard to determine experimentally. It is usually suggested to take $T_L = \frac{k}{3\varepsilon}$ based on spectral similarity considerations (Tennekes & Lumley, 1972). Based on the Langevin equations, Pope (1994) proposed several modifications and extensions for inhomogeneous flows, where the time scale T is related to local mean velocity gradients, Reynolds stresses and the dissipation rate.

It is advisable to correct Lagrangian integral time-scales for the crossing-trajectory-effect. A heavy particle continuously changes its neighborhood so that its velocity correlation drops more rapidly with time than a more diffusive particle. The Lagrangian time-scale is reduced by a factor that is a function of the particle slip velocity (averaged over a few times T_L), and the turbulent kinetic energy.

There are many situations where the distribution of particles is strongly influenced by the way particles collide with bounding walls. Specifically for wall-bounded flows containing particles with significant inertia (high particle Stokes numbers) particle dispersions is strongly influenced by particle-wall collisions. Realistic situations are hardly ever modeled accurately with the "default" case of fully elastic specular reflection off smooth walls. Wall roughness and particle rotation often complicate the picture and can add strongly to the dispersion brought about by turbulence. A detailed account on particle-wall collisions can be found in section 5.1 of this guide.

Two-way coupling

In order to account for the influence of the particle phase on the fluid flow a consecutive solution of the Eulerian and Lagrangian part is required. The calculation starts with the solution of the fluid flow by not accounting for the source terms of the dispersed phase. After having reached a certain degree of convergence for the single phase flow, the particle trajectories are calculated and the particle phase properties (i.e. concentration and particle velocities) and the source terms are sampled for each control volume. In case a particle size distribution is considered also the local particle size distributions and the size-velocity correlations may be sampled.

For a stationary computation the momentum source terms of the dispersed phase are calculated from the change of the particle velocity along a trajectory within the considered control volume. Thereby, the influence of all forces considered to act on the particle is accounted for. Field forces such as gravity and buoyancy however have to be subtracted. Hence, one obtains for the sampling of the momentum source terms as an example:

$$\overline{S_{U_i,P}} = -\frac{1}{V_{CV}\ \Delta t_{ref}} \sum_{k=1}^{k_{tot}} m_k\ N_k \sum_{n=1}^{n_s} \left\{ \left(u_{P,k,i}^{n+1} - u_{P,k,i}^{n} \right) - g_i \left(1 - \frac{\rho_F}{\rho_P} \right) \Delta t \right\} \qquad (122)$$

In this equation the sum over n implies a time-space averaging along the particle trajectory and the sum over all parcels k_{tot} passing the considered CV is an ensemble averaging. Therefore, to obtain statistically reliable source terms a sufficient number of parcels need to pass the control volumes.

The source terms in the conservation equation of the turbulent kinetic energy are obtained from the Reynolds-averaging procedure (Desjonqueres 1987):

$$S_{k,P} = \sum_{i=1}^{3} \overline{u_i\ S_{U_i,P}} - \overline{u_i}\ \overline{S_{U_i,P}} \qquad (123)$$

The source term in the ε-equation is modelled following the work of Desjonqueres (1987) in the following way:

$$S_{\varepsilon,P} = C_{\varepsilon 3} \frac{\varepsilon}{k} S_{k,P} \qquad (124)$$

As demonstrated by Squires and Eaton (1993) the constant $C_{\varepsilon 3}$ is not universal, but depends

on the particle response time and concentration. For many situations a value of $C_{e3} = 1.1$ may be used.

Thereafter, the continuous phase is re-calculated by accounting for the particle phase source terms (Fig. 4.10). In order to avoid convergence problems, an under-relaxation procedure should be applied using the following equation:

$$S_{\phi,P}^{new} = (1-\gamma)\, S_{\phi,P}^{old} + \gamma\, S_{\phi,P}^{samp}, \qquad (125)$$

where $S_{\phi,P}^{new}$ are the source terms used to calculate the new flow field, $S_{f,P}^{old}$ are the source terms used in the previous Eulerian calculation and $S_{\phi,P}^{samp}$ are the new source terms sampled in the Lagrangian calculation. The under-relaxation factor depends on the degree of coupling (i.e. depending on the particle concentration and the particle size) and is selected accordingly in the range between zero and one (Kohnen et al. 1994). After a certain number of Eulerian iterations or after a certain degree of convergence is reached for the fluid flow, again the particle tracking is performed since the flow field has changed due to the two-way coupling (i.e. the influence of the particles on the flow field). With the sampled new source terms again the continuous phase is solved and so forth until convergence is reached for the coupled system (Fig. 4.10). The overall convergence is decided based on the evolution of a certain reference value (see Kohnen et al. 1994), as for example the fluid velocity at a monitoring location.

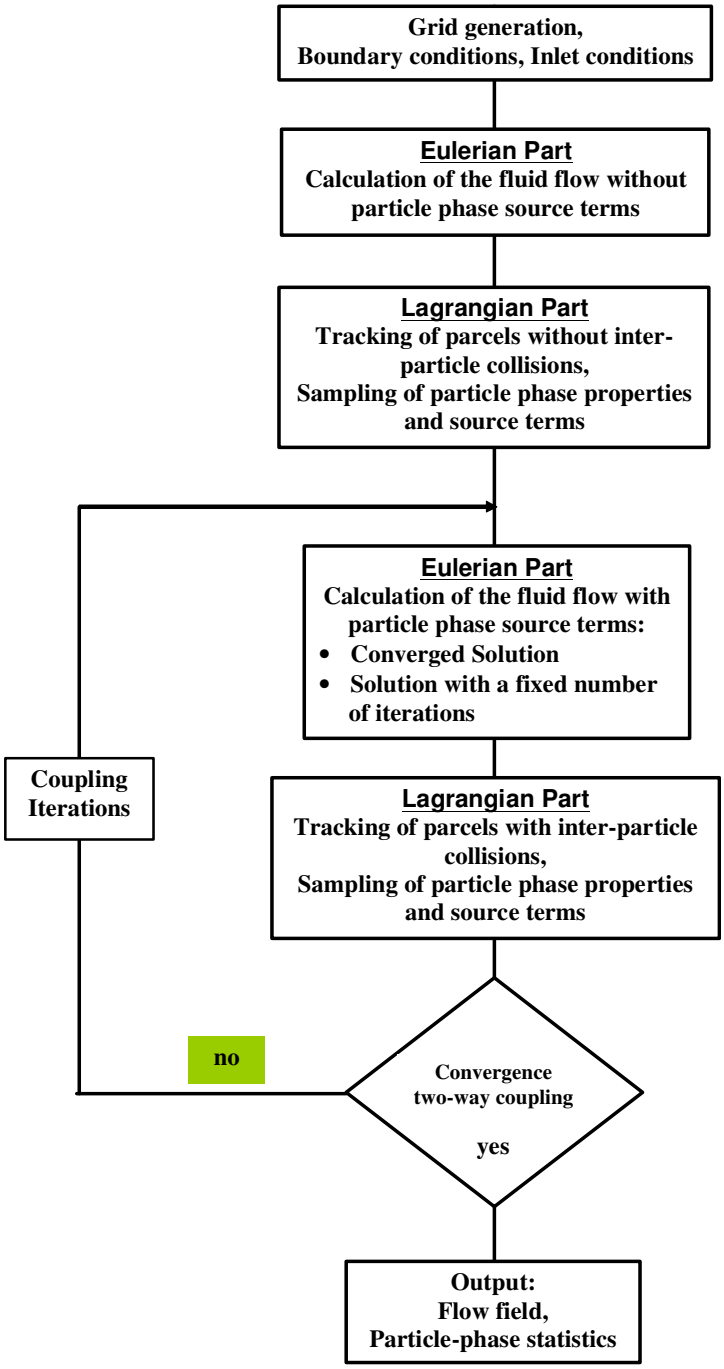

Figure 4.10 Flow chart of iteration procedure for the Euler/Lagrange approach

5 Specific Phenomena and modelling approaches

A reliable numerical prediction of multiphase flows is only possible if also the relevant elementary processes occurring on the scale of the particle are modelled properly, e.g. turbulent dispersion of particles, particle-wall collisions, inter-particle collisions and agglomeration. For the derivation of these models generally detailed micro-scale experiments are required to obtain the relevant model constants, such as the restitution ratio or the friction coefficients (e.g. Sommerfeld & Huber 1999). Nowadays also DNS and LES are increasingly used for supporting the derivation of models and closure relations. The latter is of importance especially for two-fluid approaches,,although its application within the two-fluid framework

remains difficult from a fundamental point of view, as explained earlier. After model derivation the validation of the numerical predictions is an important step. For this purpose DNS or LES might be used if turbulent transport of the particles is the considered phenomenon. In most other cases detailed experiments on not too complex multiphase flow systems are required. Here, it should be tried to select the experiments in such a way that one transport mechanism or elementary process is dominant, e.g. measurements in a narrow horizontal channel flow for validating wall collision models or interacting particle-laden jets for validating inter-particle collision models. Moreover, the measurement should be done using non-intrusive optical techniques (Sommerfeld and Tropea 1999) wherever it is possible in order not to disturb the flow.

In the following sections, several elementary processes and the derived models will be described. Moreover, it will be tried to introduce rules of thumb for deciding under which conditions the different elementary processes are important or not.

5.1 Particle-Wall Collisions

Particle-wall collisions become of importance in confined flows, such as pneumatic conveying or particle separation in cyclones. In pneumatic conveying, for example, the momentum loss of a particle caused by an inelastic wall impact is associated with a re-acceleration of the particle by the fluid after rebound. Hence, momentum is extracted from the fluid phase for this acceleration causing the additional pressure loss. This pressure loss depends on the average wall collision frequency or mean free path between subsequent particle-wall collisions. The wall collision frequency is mainly determined by the following parameters:

- particle mass loading,
- dimensions of the confinement, e.g. pipe diameter in pneumatic conveying,
- particle response time or response distance,
- conveying velocity and turbulence intensity,
- particle shape and wall roughness,
- combination of particle and wall material.

A first estimate of the importance of particle-wall collisions may be based on the ratio of the particle response distance λ_p to the dimension of the confinement, e.g. the diameter of the pipe D. The particle response distance can be estimated from the following equation:

$$\lambda_p = \frac{\rho_p \, D_p^2}{18 \, \mu_F \, f_D} \cdot w_t \,, \qquad (11426)$$

where w_t is the terminal velocity of the particle. For the case λ_p is larger than the dimension of the confinement D, the particles are not able to respond to the flow before they collide with the opposite wall, hence their motion is dominated by wall collisions. In addition to the above mentioned effects the wall collision process may be affected by hydrodynamic interaction which eventually causes a deceleration of the particle before impact (see above, the section on drag due to wall effects). This effect however is only of importance for viscous fluids and hence small particle Reynolds numbers.

5.1.1 Velocity change during wall collision

In the following the so-called hard sphere model for the wall collision will be described, which implies a negligible particle deformation during the impact process. Moreover, Coulomb's law of friction is assumed to hold for a sliding collision. For an inelastic collision

process, one may identify a compression and a recovery period. The change of the particles translational and rotational velocities during the bouncing process can be calculated from the momentum equations of classical mechanics (Crowe et al. 1998). Three types of collisions may be distinguished:

- Type 1: The particle stops sliding in the compression period.
- Type 2: The particle stops sliding in the recovery period.
- Type 3: The particle continues to slide along the wall during the whole collision process.

The type of collision is determined by the static coefficient of friction μ_0, the restitution ratio of the normal velocity components, e, and the velocity of the particle surface relative to the contact point, u_{R0}. Since the temporal evolution of the normal contact force is unknown, the integrated version of Newton's law is used to determine the change of the linear velocities from:

$$m_p \left(\vec{u}_{p2} - \vec{u}_{p0}\right) = \int_{t_0}^{t} \vec{F}_n \, dt = \vec{J} \, . \qquad (11527)$$

In a similarly way the equation for the change of the angular impulse momentum reads as:

$$\frac{I_p}{R_p}\left(\vec{w}_{p2} - \vec{w}_{p0}\right) = -\,\vec{n}\; x\; \vec{J} \, . \qquad (11628)$$

Here the collision process is separated into the compression and recovery period, respectively and the index 0 refers to the velocities before impact, 1 and 2 indicate the velocities at the end of the compression period and after rebound. In Eqs. **Error! Reference source not found.** and (11628) m_p is the particle mass, I_p the moment of inertia (i.e. $I_p = 0.1\ m_p\ D_p^2$ for a sphere), $\vec{n}$ is the unit vector and $\vec{J}$ the vector of the impulse force. The normal restitution ratio is defined the ratio of the normal impulses (i.e. recovery impulse to compression impulse):

$$e = \frac{J_{y,r}}{J_{y,c}} \, . \qquad (11729)$$

Evaluating Eqs. **Error! Reference source not found.** and (11628) in connection with the appropriate boundary conditions, two sets of equations are obtained for a sliding and non-sliding collision which allow the determination of the change of the linear and angular velocity of the particle in a wall collision process. A **non-sliding collision** (type 1 and 2) takes place when the following condition is valid:

$$\left|J_x\right| \geq \mu\, J_y \, , \qquad (11830)$$

$$\left|u_{R0}\right| \leq \frac{7}{2}\ \mu_0\ \left(1+e\right)\ v_{P0} \, , \qquad (11931)$$

$$u_{R0} = \sqrt{\left(u_{P0} + \frac{D_P}{2}\,\omega_{P0}^{z}\right)^2 + \left(w_{P0} - \frac{D_P}{2}\,\omega_{P0}^{x}\right)^2} \, , \qquad (12032)$$

where, u_P, v_P, and w_P are the translational velocity components in the x-, y- and z-direction

and ω_P^x, ω_P^y, and ω_P^z are the angular velocity components of the particle in a co-ordinate system as shown in Figure 3.13. The subscripts 1 and 2 refer to the conditions before and after collision, respectively. For the **non-sliding collision**, the change of particle velocities is obtained by:

$$\begin{aligned} u_{P2} &= \frac{5}{7}\left(u_{P0} - \frac{D_P}{5}\ \omega_{P0}^z\right) \\ v_{P2} &= -e\ v_{P0} \\ w_{P2} &= \frac{5}{7}\left(w_{P0} + \frac{D_P}{5}\ \omega_{P0}^x\right) \end{aligned} \qquad (12133)$$

$$\begin{aligned} \omega_{P2}^x &= \frac{2\ w_{P2}}{D_P} \\ \omega_{P2}^y &= \omega_{P0}^y \\ \omega_{P2}^z &= -\frac{2\ u_{P2}}{D_P} \end{aligned} \qquad (12234)$$

The collision type 3 is the so-called **sliding collision** which occurs for:

$$|u_{R0}| \geq \frac{7}{2}\ \mu_0\ (1+e)\ v_{P0}\,. \qquad (12335)$$

The change of translational and rotational velocities throughout the sliding collision is obtained by:

$$\begin{aligned} u_{P2} &= u_{P0} + \mu_d\ \varepsilon_x\ (1+e)\ v_{P0} \\ v_{P2} &= -e\ v_{P0} \\ w_{P2} &= w_{P0} + \mu_d\ \varepsilon_z\ (1+e)\ v_{P0} \end{aligned} \qquad (12436)$$

$$\begin{aligned} \omega_{P2}^x &= \omega_{P0}^x - 5\,\mu_d\ \varepsilon_z\ (1+e)\ \frac{v_{P0}}{D_P} \\ \omega_{P2}^y &= \omega_{P0}^y \\ \omega_{P2}^z &= \omega_{P0}^z + 5\,\mu_d\ \varepsilon_x\ (1+e)\ \frac{v_{P0}}{D_P} \end{aligned} \qquad (12537)$$

In Eqs. (12436) and (12537) the terms ε_x and ε_z determine the direction of the motion of the particle surface with respect to the wall:

$$\begin{aligned} \varepsilon_x &= \frac{u_{P0} + \frac{D_P}{2}\ \omega_{P0}^z}{u_{R0}} \\ \varepsilon_z &= \frac{w_{P0} - \frac{D_P}{2}\ \omega_{P0}^x}{u_{R0}} \end{aligned} \qquad (12638)$$

In the above equations e is the restitution ratio, μ_0 and μ_d are the static and dynamic coefficients of friction. Unfortunately, these parameters are not only dependent on the

material of particle and wall, but also on impact velocity and angle (see for example Sommerfeld & Huber 1999).

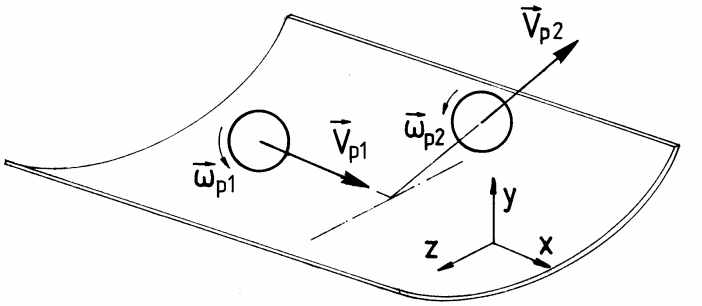

Figure 5.1: Configuration of a particle-wall collision

5.1.2 Wall roughness effect

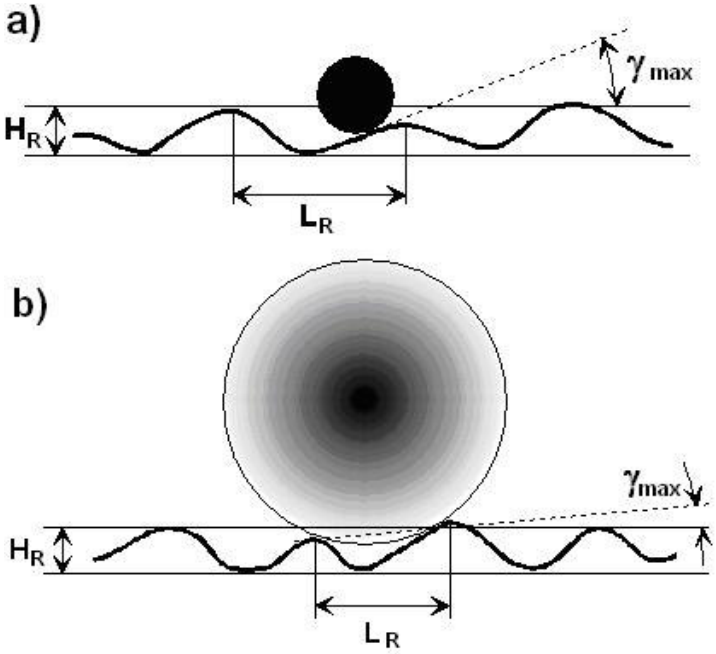

Figure 5.2: Illustration of wall roughness effect for (a) small and (b) large particles.

Several experimental studies have shown that wall roughness has a considerable impact on the particle wall collision process (Sommerfeld 1992, Huber & Sommerfeld 1998, Sommerfeld & Huber 1999). In industrial equipment, as for example pneumatic conveying lines, steel pipes are used, which have a mean roughness height between about 20 and 50 µm, depending on the way of manufacture. Experimental studies of Sommerfeld & Huber (1999) revealed that the roughness angle distribution may be represented by a normal distribution function. The standard deviation of this distribution is influenced by the roughness structure and the particle size. The dimensions of the roughness structure suggest, that the wall collision process of small particles (i.e. < 100 µm) should be strongly affected, since they will be able to experience the details of the roughness structure (Figure 5.2a). However, after rebound they will quickly adjust to the flow, so that the influence of the wall roughness effect is limited to the near wall region and will not strongly affect the particle behaviour in the bulk of the flow. On the other hand large particles may cover several roughness structures during wall impact (Figure 5.2b). This implies that they "feel" less wall roughness. However, due to

their high inertia, they will need more time to adjust to the flow after rebound. This eventually causes the wall roughness to be more important for the bulk behaviour of larger particles in a given flow (Sommerfeld 1992 and 1996). In addition, the so-called shadow effect for small impact angles results in a shift of the effective roughness angle distribution towards positive values since the particles are not able to reach the lee-side of the roughness structures (Figure 5.3). Hence, for small impact angles the effective mean impact angle is increased compared to the particle trajectory angle with respect to the plane wall (Sommerfeld & Huber 1999). This implies a transfer of momentum from the wall-parallel component to the normal component, i.e. the normal component of the rebound velocity becomes larger than the impact component for smaller impact angles (Figure 5.4). In this region the velocity ratio of the normal component does not correspond to the restitution ratio.

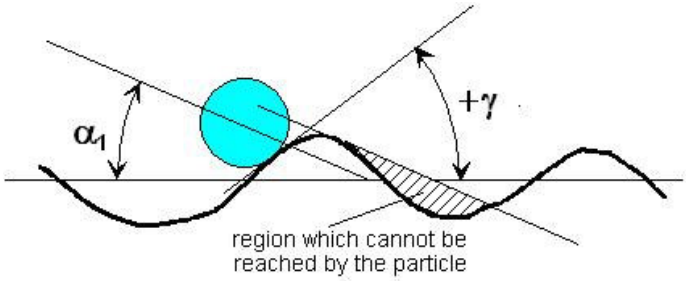

Figure 5.3: Illustration of the shadow-effect for small impact angles.

However, at larger impact angles the velocity ratio approaches the expected restitution ratio, which depends on the wall material used in the experiments. In pneumatic conveying the shadow effect causes a re-dispersion of the particles, whereby the influence of gravitational settling is reduced (Huber & Sommerfeld 1998).

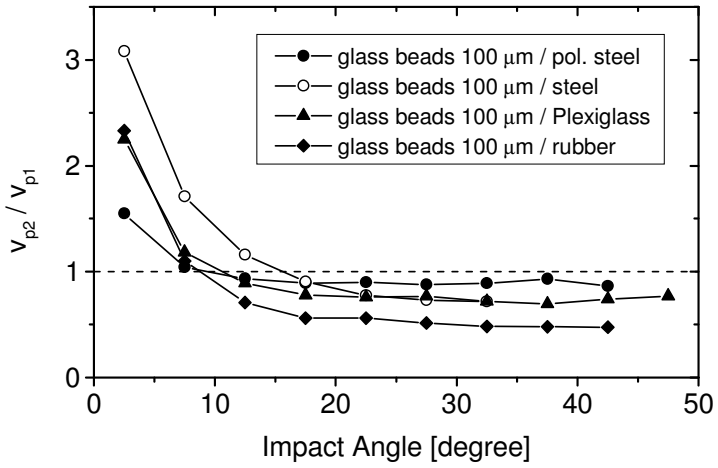

Figure 5.4: Measured dependence of the velocity ratio for the component normal to the wall on the impact angle for different wall material and 100 µm glass beads (Sommerfeld & Huber 1999)

5.1.3 Importance of wall collisions in channel and pipe flows

Here the effect of wall collisions and wall roughness on the behaviour of particles in a horizontal channel of 35 mm height and a length of 6 m is analysed. The gas flow field (i.e. mean velocity and turbulence) was prescribed according to the measurements of Laufer (1952) for a fully developed channel flow with an average velocity of 18 m/s and two-way

coupling was not considered. The gas density was given a value of 1.18 kg/m^3 and the dynamic viscosity was selected to be $18.8 \cdot 10^{-6}$ N s/m^2. The particle motion was calculated by solving the equation of motion including drag force, gravity, transverse lift forces due to shear and particle rotation, and turbulence effects (Sommerfeld et al. 1993). Wall roughness is modelled as proposed by Sommerfeld & Huber (1999), where the effective impact angle is composed of the particle trajectory angle and a stochastic normal distributed component to account for wall roughness. In Figure 5.5 the behaviour of particles with different diameters (ρ_P = 2500 kg/m^3) in a channel without and with wall roughness is illustrated. It is obvious that the wall roughness has a stronger effect on the motion of larger particles (compare Figure 5.5 b and e), whereby they bounce from wall to wall. The result of the particle trajectory calculation (Figure 5.5) may be summarised by plotting an average wall collision mean free path obtained from subsequent wall collisions (Sommerfeld 2003), over the particle size (Figure 5.6). Considering the case without wall roughness it is obvious that small particles are dispersed by turbulence (see also Figure 5.5a), whereby the wall collision frequency is relatively low (i.e. the wall collision mean free path is large). Increasing particle size results in a decrease of the wall collision mean free path and a minimum is obtained for the present flow condition and channel height for a particle size of about 100 µm. As a result of gravity these particles have a saltating motion without contacting the upper wall. With further increasing particle size the wall collision mean free path reaches a maximum since the particles perform long "jumps" and just do not reach the upper channel wall (Figure 5.5c). For particles larger than 300 µm the mean free path is again slightly reduced and they bounce from wall to wall due to their high inertia (Figure 5.6). By considering the lift forces as described above (see sections 3.5 and 3.6), the wall collision mean free path is increased over the entire particle sizes considered, since the lift forces is acting in the direction of the centre of the channel (Figure 5.6).

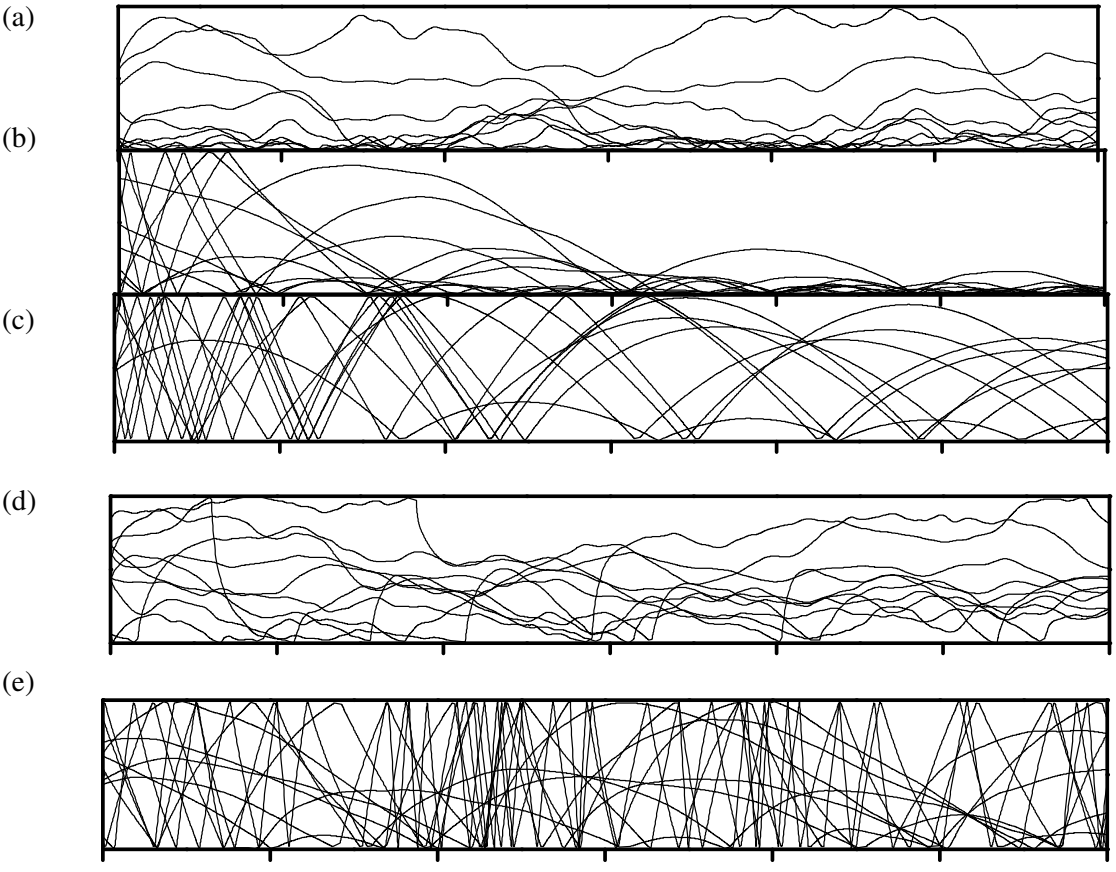

Figure 5.5: Calculated particle trajectories in a horizontal channel flow (channel height 35 mm and length 6 m), without wall roughness: a) 30 µm, b) 110 µm, c) 300 µm, with wall roughness: d) 30 µm, e) 110 µm (U_{av} = 18 m/s)

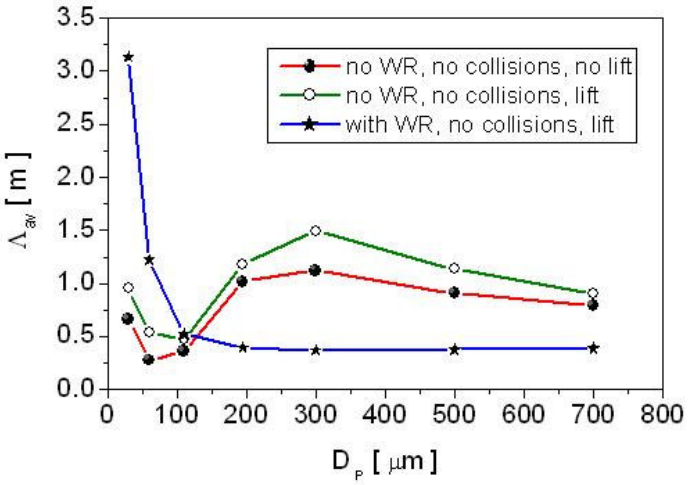

Figure 5.6: Calculated wall collision mean free path as a function of particle diameter for a horizontal channel of 35 mm height (U_{av} = 18 m/s).

The consideration of wall roughness changes the picture completely. Even small particles are considerably better suspended in the flow (Figure 5.5d). For large particles the bouncing from wall to wall is enhanced and the wall collision frequency increases. This is most pronounced for the 110 µm particles (compare Figure 5.5b and e) where due to the shadow effect the particles are almost completely dispersed over the cannel. This is also illustrated in Fig. 5.7 where the particle mass flux profiles for calculations with and without wall roughness are shown. Without wall roughness gravitational settling is observed, while with wall roughness, the particle mass flux is almost constant over the channel height. The particle bouncing from wall to wall results in an almost constant wall collision mean free path of about 0.35 m for particles above about 200 µm (Figure 5.6). For 30 µm particles the consideration of wall roughness results in a mean free path of about 2 m, which is much larger than for the case without wall roughness. Hence for such small particles (up to about 80 µm) the wall collision frequency is reduced due to wall roughness. This should actually also be associated with a reduction of the additional pressure drop by the particles in cases of rough walls in comparison to smooth walls. A detailed analysis of the wall collision process is an interesting topic of research, but eventually the process design is dominated by the operational cost, which means in case of pneumatic conveying the pressure loss is of great importance.

Figure 5.7: Calculated profiles of the particle mass flux in a horizontal channel, influence of wall roughness (U_{av} = 18 m/s, 195 µm particle).

The overall pressure loss in pneumatic conveying is dominated by the particle phase and especially wall collisions and roughness may cause a considerable momentum loss for larger particles (Sommerfeld & Kussin 2004). This is demonstrated in Fig. 5.8, where the calculated stream-wise velocity profiles of the particle phase in the horizontal channel are shown. The particle mean velocity is considerably reduced for the case with wall roughness compared to that without and the difference between these two cases is increasing with particle size. Actually, the mean velocity for the 60 µm particles increases in the near wall region, especially near the bottom wall. This is the result of the overall reduction of the wall collision frequency due to wall roughness (see Figure 5.6). The reduction of the particle velocity in the core region of the channel is associated with a stronger dispersion of the particles due to wall roughness. This discussion suggests that a considerable increase of pressure loss should result from wall roughness in the case of larger particles. A numerical computation for the horizontal channel using the Euler/Lagrange approach (Lain & Sommerfeld 2006) clearly demonstrates this effect. In this case a particle size of 130 µm and a conveying velocity of 20 m/s is considered. The computed pressure loss along the horizontal channel increases considerably with wall roughness (Figure 5.9). Moreover, the result shows the increasing additional pressure loss due to the particles with the mass loading. The predictions agree reasonably well with the experiments for all cases. This demonstrates the importance of wall roughness and that the described model (Sommerfeld & Huber 1999) captures this effect reasonably well.

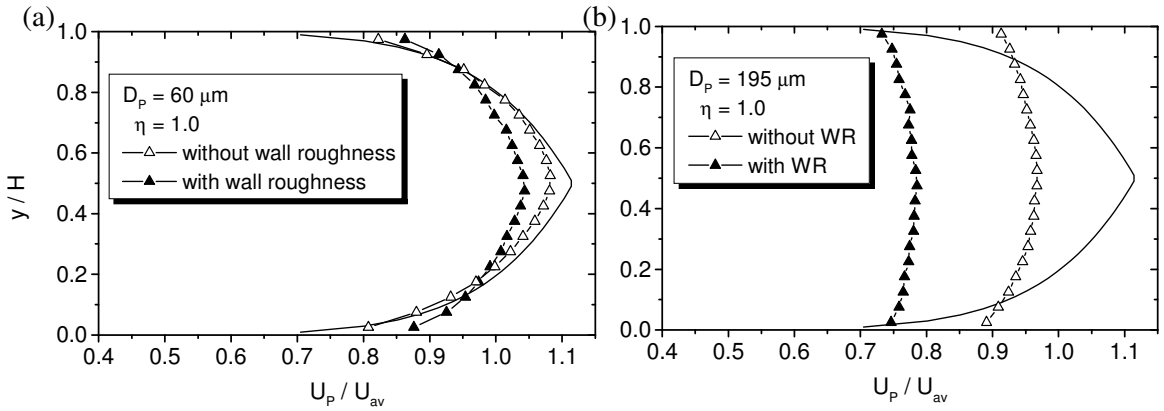

Figure 5.8: Calculated profiles of the particle velocity in a horizontal channel, influence of wall roughness (U_{av} = 18 m/s, closed line represents presumed gas velocity profile), a) 60 µm particle, b) 195 µm particle.

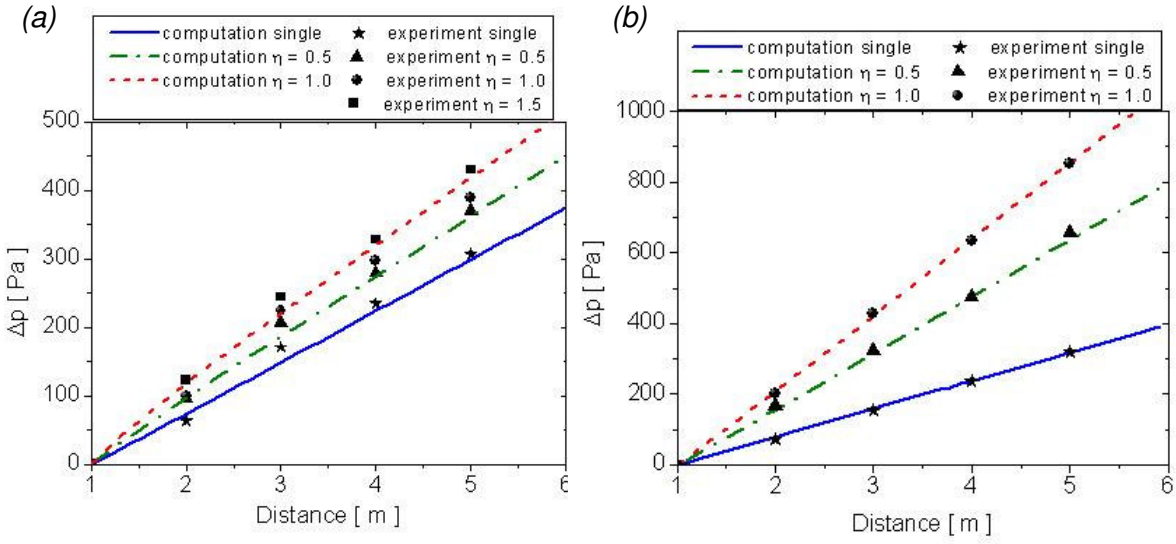

Figure 5.9: Pressure drop along the horizontal channel with a height of 35 mm, comparison of measurement and computation using the Euler/Lagrange approach (spherical glass beads with a number mean diameter of 130 µm, conveying velocity 20 m/s, variable mass loading), a) roughness 2.3 µm, b) roughness 17 µm (Lain & Sommerfeld 2006).

5.2 Inter-Particle Collisions

Inter-particle collisions may have several consequences in particle-laden flows, such as for heat and momentum transfer between particles, dispersion of particles out of regions with locally high concentration, and eventually also agglomeration of particles. Essential for inter-particle collisions to occur, is a relative motion between the particles. Such a relative motion may be caused by several mechanisms:

Brownian or thermal motion of particles,

laminar or turbulent fluid shear,

particle inertia in turbulent flow,

mean drift between particles of different size (so-called differential settling).

The collision rate (i.e. collisions per unit volume and time) between two particle fractions i and j for **Brownian motion** was given by Smoluchowski (1916) as:

$$N_{ij} = \frac{2\,k\,T}{3\,\mu_F}\, n_i\, n_j\, \frac{\left(D_i + D_j\right)^2}{D_i\, D_j}, \qquad (12739)$$

where D_i and D_j are the diameters of the considered particle classes, k is the Boltzmann constant, T is the absolute temperature, and μ_F is the dynamic viscosity of the fluid.

For particles which are small compared with the smallest scales of turbulence, i.e. the Kolmogorov length scale, and completely follow turbulence Saffman and Turner (1956) have provided an expression for the **collision rate due to turbulent shear**:

$$N_{ij} = \left(\frac{8\,\pi}{15}\right)^{1/2} n_i\, n_j \left(R_i + R_j\right)^3 \left(\frac{\varepsilon}{\nu_F}\right)^{1/2}, \qquad (12840)$$

where ε is the dissipation rate of turbulent energy and ν is the kinematic viscosity of the fluid.

The **collision rate due to particle inertia in turbulent flow** was also derived by Saffman and Turner (1956) and is given by:

$$N_{ij} = \left(\frac{\pi}{2}\right)^{1/2} \frac{1.3}{18\,\mu_F} \left(D_i + D_j\right)^2 n_i\, n_j \left(\rho_p - \rho_F\right) \left(D_i^2 - D_j^2\right)^2 \left(\frac{\varepsilon^3}{\nu_F}\right)^{1/2}. \qquad (12941)$$

The **collision rate due to a mean drift between particles** of different size may be derived from kinetic theory of gases given as:

$$N_{ij} = \frac{\pi}{4} \left(D_i + D_j\right)^2 n_i\, n_j \left|u_i - u_j\right|. \qquad (13042)$$

Introducing the terminal velocity of the particles, this is for the Stokes-regime obtained from:

$$u_t = \frac{\left(\rho_p - \rho_F\right) D_p^2}{18\,\mu_F}\, g, \qquad (13143)$$

yields the collision rate for differential settling:

$$N_{ij} = \frac{\pi\, g}{72\,\mu_F}\left(D_i + D_j\right)^2 n_i\, n_j \left(\rho_p - \rho_F\right)\cdot\left|D_i^2 - D_j^2\right|. \qquad (13244)$$

In turbulent flows the particle response and the importance of inter-particle collisions may be characterised by a turbulent Stokes number, which is the ratio of the particle response time τ_p to the relevant time scale of turbulence T_t:

$$St_t = \frac{\tau_p}{T_t}. \qquad (13345)$$

Based on the Stokes number the limiting cases for the collision rate due to turbulence may be identified. Very small particles which completely follow turbulence (i.e. $St_t \to 0$) have a highly correlated velocity and the expression of Saffman and Turner (1956), i.e. Eq. (12840), holds for the collision rate. The other limiting case is the kinetic theory for $St_t \to \infty$, where the particle motion is completely de-correlated with the fluid and hence the velocity of colliding particles is also de-correlated (i.e. granular medium). This case was analysed by Abrahamson (1975) for heavy particles in high intensity turbulence neglecting external forces, which implies that there is no mean relative velocity between the particles. The resulting collision rate between two particle fractions is given by:

$$N_{ij} = 2^{\frac{3}{2}}\,\pi^{\frac{1}{2}}\, n_i\, n_j \left(R_i + R_j\right)^2 \sqrt{\sigma_i^2 + \sigma_j^2}, \qquad (13446)$$

where σ_p is the fluctuating velocity of the particles assuming that all components are identical (i.e. isotropic fluctuating motion $\sigma_p^2 = \overline{u_p'^2} = \overline{v_p'^2} = \overline{w_p'^2}$). The expression derived by Abrahamson (1975) is strictly only valid for particles of identical size, since it does not account for a mean drift between the particles. For such a case the collision rate was provided by Gourdel et al. (1999):

$$N_{ij} = \frac{\pi}{4}\left(D_i + D_j\right)^2 n_i\, n_j \left|U_i - U_j\right| G\left(z\right), \qquad (13547)$$

with:

$$G\left(z\right) = \frac{1}{\sqrt{\pi\, z}}\exp\left(-z\right) + \left(1 + \frac{1}{2\,z}\right) erf\,\sqrt{z}, \qquad (13648)$$

and:

$$z = \frac{3}{4}\,\frac{\left(U_i - U_j\right)^2}{k_i + k_j}. \qquad (13749)$$

In this equation U_i and U_j are the mean velocities of the particle fraction i and j, and k_i and k_j are the energies of their fluctuating velocities namely:

$$k_p = \frac{1}{2}\left(\overline{u_p'^2} + \overline{v_p'^2} + \overline{w_p'^2}\right). \qquad (13850)$$

In practical two-phase flows the two limits (i.e particles completely following turbulence ($St_t \rightarrow 0$) and heavy particles ($St_t \rightarrow \infty$)) are rarely met, rather the particles may partially respond to turbulence. Hence, the velocities of colliding particles will be correlated to a certain degree, since they are transported in the same turbulent eddy upon collision. The degree of correlation depends on the turbulent Stokes number defined above (Eq. (13345)). An analysis of this effect was performed by Williams and Crane (1983) and an analytic expression for the collision rate of particles in turbulent flows covering the entire range of particle Stokes numbers and accounting for a possible correlation of the velocities of colliding particles was suggested. The expression for the collision rate is given in terms of particle concentration, particle relaxation times (i.e. Stokes numbers), turbulence intensities, and turbulent scales:

$$N_{ij} = (162\ \pi)^{\frac{1}{2}}\ n_i\ n_j\ \nu_F\ L_t \frac{\rho_F}{\rho_p}\ \frac{\overline{u_{ij}}}{\sigma_F}\left(St_i^{0.5} + St_j^{0.5}\right)^2 \cdot \frac{2}{\pi}\tan^{-1}\left\{\frac{1}{3}\frac{\rho_p}{\rho_F}\frac{\sigma_F\ L_t}{\nu_F}\left(\frac{\overline{u_{ij}}}{\sigma_F}\right)^2 \frac{St_i\ St_j}{\left(St_i^{0.5} + St_j^{0.5}\right)^2}\right\}. \qquad (13951)$$

Here L_t is the integral length scale of turbulence, $\overline{u_{ij}}$ the mean relative velocities between colliding particles, and σ_F the fluctuating velocity of the fluid assuming isotropic turbulence. The Stokes numbers of the two particle classes St_i and St_j are defined in terms of the integral time scale of turbulence.

5.2.1 Importance of Inter-Particle Collisions

In the following the importance of inter-particle collisions in turbulent fluid-particle flows is discussed. The inter-particle collision probability depends mainly on the particle concentration, the particle size, and the fluctuating motion of the particles. A classification of particle-laden flows in terms of the importance of inter-particle collisions and the boundary between dilute and dense systems may be based on the ratio of particle response time τ_p to the averaged time between collisions τ_c (Crowe 1981). In dilute two-phase flows the particle motion will be mainly governed by fluid dynamic transport effects, i.e. drag force, lift forces, and turbulence. On the other hand dense flows are characterised by high collision frequencies between particles and hence their motion is dominantly influenced by inter-particle collisions. Fluid dynamic transport effects are of minor importance. Therefore, the two regimes are characterised by the following time scale ratios:

dilute two-phase flow:

$$\tau_p < \tau_c \quad \longrightarrow \quad \frac{\tau_p}{\tau_c} < 1, \qquad (14052)$$

dense two-phase flow:

$$\tau_p > \tau_c \quad \longrightarrow \quad \frac{\tau_p}{\tau_c} > 1. \qquad (14153)$$

This implies that in dense two-phase flows the time between particle-particle collisions is smaller than the particle response time, whereby the particles are not able to completely respond to the fluid flow between successive collisions. (This regime may occur when either very large particles at a low number density are present in the flow or in the case of small particles when the number density is large.) In dilute two-phase flows collisions between particles may also occur and influence the particle motion to a certain degree, but the time

between successive inter-particle collisions is larger than the particle response time, whereby the fluid dynamic transport of the particles is the dominant transport effect.

In the following section an estimate of the boundary between the two regimes will be given for turbulent particle-laden flows by introducing some simplifications. The average time between successive inter-particle collisions results from the average collision frequency:

$$\tau_c = \frac{1}{f_c}. \qquad (14254)$$

The collision frequency of one particle (i.e. $n_i = 1$) with diameter D_i and instantaneous velocity $\vec{u}_i$ with all other particle classes (i.e. N_{class}) with diameter D_j and velocity $\vec{u}_j$ can be calculated according to kinetic theory of gases from:

$$f_c = \frac{N_{ij}}{n_i} = \sum_{j=1}^{N_{class}} \frac{\pi}{4} \left(D_i + D_j\right)^2 \left|\vec{u}_i - \vec{u}_j\right| n_j. \qquad (14355)$$

The main assumptions associated with the use of Eq. (14355) are the following:

The particle number concentration is small enough that the occurrence of binary collisions prevails.

On the other hand the particle number concentration must be large enough to allow a statistical treatment.

The velocities of the colliding particles are not correlated, for example due to turbulence.

An analytic solution of Eq. (14355) is only possible for relatively simple cases. For the estimation of the collision frequency, the derivation of Abrahamson (1975) is followed, yielding a collision rate solely determined by turbulence (Eq. (13446)). Furthermore, a mono-disperse particle phase is considered, whereby the mean fluctuating velocity is a constant. Hence the collision frequency is obtained as a function of the particle diameter, D_P, the total particle number concentration n_P and the mean fluctuating velocity of the particles σ_P:

$$f_c = 4\ \pi^{1/2}\ n_P\ D_P^2\ \sigma_P. \qquad (14456)$$

Introducing the volume fraction of the particles, $\alpha_P = \left(\pi/6\right) D_P^3\ n_P$, one obtains after some re-arrangements:

$$f_c = \frac{24}{\pi^{1/2}}\ \frac{\alpha_P\ \sigma_P}{D_P}, \qquad (14557)$$

or similarly the collision frequency can be expressed as a function of the mass loading $\eta = \dot{m}_P / \dot{m}_F$, which is often used to characterise gas-solid flows:

$$f_c = \frac{24}{\pi^{1/2}}\ \frac{\rho_F}{\rho_P}\ \frac{\eta\ \sigma_P}{D_P}. \qquad (14658)$$

By introducing now the collision frequency and the Stokesian particle response time into Eqs. (14557) and (14658), the limiting particle diameter for a dilute two-phase flow can be determined as a function of volume fraction or mass loading, respectively:

$$D_P < \frac{3}{4}\ \pi^{1/2}\ \frac{\mu_F}{\alpha_P\ \rho_P\ \sigma_P},$$
$$D_P < \frac{3}{4}\ \pi^{1/2}\ \frac{\mu_F}{\eta\ \rho_F\ \sigma_P}. \qquad (14759)$$

Considering a gas-solid flow with the properties (ρ_F = 1.15 kg/m^3, ρ_p = 2500 kg/m^3, μ_F = 18.4·10^{-6} kg/(m s)) the limiting particle diameter which separates dilute and dense two-phase flow is calculated as a function of volume fraction and mass loading with the particle velocity fluctuation as a parameter. The result is given in Figure 5.10 where dilute two phase flow is domain on the left of the individual lines and the dense flow regime is on the right hand side. With increasing particle diameter associated with higher particle inertia (larger τ_p), the range of dilute flow is shifted towards lower volume fractions and mass loading. With increasing velocity fluctuation of the particles the boundary line between dilute and dense two-phase flow is shifted to the left, i.e. to smaller mass loading of the dispersed phase. From Eq. (14456) it is obvious that the collision frequency increases with the velocity fluctuation of the particles.

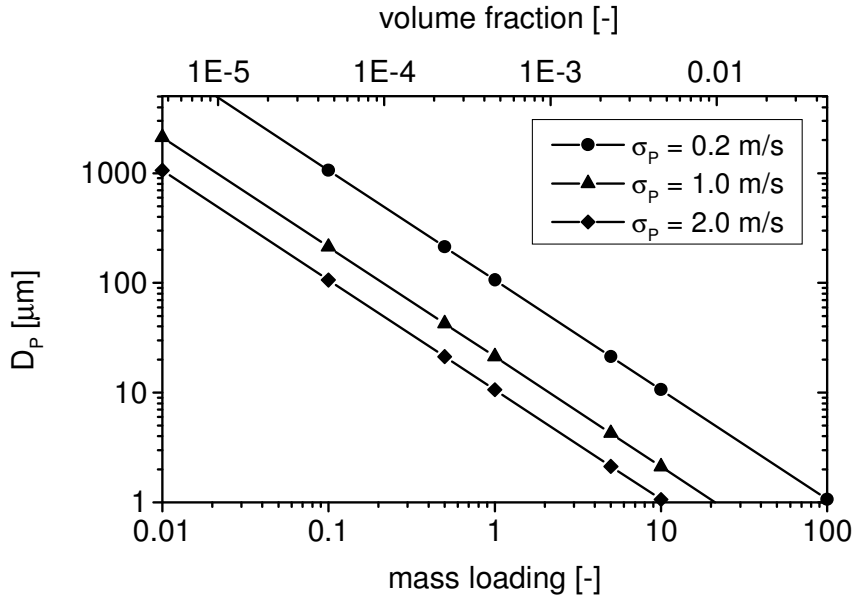

Figure 5.10: Regimes of dilute and dense gas-solid flows in dependence of mass loading (and volume fraction) and particle diameter for different particle velocity fluctuations (ρ_F = 1.15 kg/m^3, ρ_p = 2500 kg/m^3, μ_F = 18.4·10^{-6} kg/(m s))

5.2.2 Particle Velocity Change due to Inter-Particle Collisions

The calculation of the particle velocity change due to inter-particle collisions relies generally on the following assumptions:

Only binary collisions are considered, which is valid for most dispersed two-phase systems.

The deformation of the particles during the collision process is not considered explicitly, which results in the so-called hard sphere model. Hence, the dissipation of energy due to deformation is described by a normal restitution ratio.

The friction in the case of a sliding collision is described by Coulomb's law.

Hence, the change of linear and angular velocity components can be calculated by solving the

momentum equations in connection with Coulomb's law of friction, so that again relations are obtained for a sliding and non-sliding collision. The impulse equation for the change of the translational velocities is given by:

$$m_{P1}\left(\vec{u}^{*}_{P1}-\vec{u}_{P1}\right)=-m_{P2}\left(\vec{u}^{*}_{P2}-\vec{u}_{P2}\right)=\vec{J}\,, \qquad (14860)$$

and the change of particle angular velocity during collision can be calculated from:

$$\frac{I_{P1}}{R_{P1}}\left(\vec{\omega}^{*}_{P1}-\vec{\omega}_{P1}\right)=\frac{I_{P2}}{R_{P2}}\left(\vec{\omega}^{*}_{P2}-\vec{\omega}_{P2}\right)=-\vec{n}\times\vec{J}\ . \qquad (14961)$$

In these equations m_p is the particle mass, I_p the moment of inertia (i.e. $I_p = 0.1\ m_p\ D_p^2$ for a sphere), $\vec{n}$ is the unit vector and $\vec{J}$ the vector of the impulse force. By solving these equations for the three components one can calculate the change of linear and angular particle velocities dunging a collision.

The problem may be further simplified by transforming the particle velocities into a coordinate system where one of the particles is stationary, for example particle ② in Figure 5.11. For such a collision geometry, where the relative velocity vector coincides with the axis of the collision cylinder, the relations for the calculation of the post-collision properties of both particles reduce to that for an oblique central collision (Oesterle & Petitjean 1994, Sommerfeld 1995, Sommerfeld 2001). Hence, one obtains the following set of equations to calculate the new linear and angular velocity components (suffix *) of both particles in terms of the relative velocity components before collision:

$$\begin{aligned}
u^{*}_{P1} &= u_{P1}+\frac{J_x}{m_{P1}}, & u^{*}_{P2} &= -\frac{J_x}{m_{P2}}, \\
v^{*}_{P1} &= v_{P1}+\frac{J_y}{m_{P1}}, & v^{*}_{P2} &= -\frac{J_y}{m_{P2}}, \qquad (15062)\\
w^{*}_{P1} &= +\frac{J_z}{m_{P1}}, & w^{*}_{P2} &= -\frac{J_z}{m_{P2}}.
\end{aligned}$$

$$\begin{aligned}
\omega^{*x}_{P1} &= \omega^{x}_{P1}, & \omega^{*x}_{P2} &= \omega^{x}_{P2}, \\
\omega^{*y}_{P1} &= \omega^{y}_{P1}-\frac{5\ J_z}{m_{P1}\ D_{P1}}, & \omega^{*y}_{P2} &= \omega^{y}_{P2}+\frac{5\ J_z}{m_{P2}\ D_{P2}}, \qquad (15163)\\
\omega^{*z}_{P1} &= \omega^{z}_{P1}+\frac{5\ J_y}{m_{P1}\ D_{P1}}, & \omega^{*z}_{P2} &= \omega^{z}_{P2}-\frac{5\ J_y}{m_{P2}\ D_{P2}}.
\end{aligned}$$

Here, m_{P1} and m_{P2} are the masses of both particles and J_x, J_y and J_z are the components of the impulsive force. With the definition of the normal restitution ratio:

$$e=-\frac{u^{*}_{P1}-u^{*}_{P2}}{u_{P1}}, \qquad (15264)$$

and the conservation of the x-component of the momentum for particle 2:

$$J_x=-m_{P2}\ u^{*}_{P2}, \qquad (15365)$$

one finally obtains the following expression for J_x:

$$J_x = -(1+e)\ u_{P1}\ \frac{m_{P1}\ m_{P2}}{m_{P1}+m_{P2}}. \qquad (15466)$$

By applying Coulomb's law of friction one obtains furthermore the condition for a non-sliding (rolling) collision as a function of the static coefficient of friction μ_0:

$$\sqrt{J_y{}^2 + J_z^2} < \mu_0\ \left|J_x\right|. \qquad (15567)$$

Now the components of the impulse force are introduced into Eq. (15567) and the condition for a non-sliding collision is obtained in dependence on the velocities of both particles before collision:

$$\left|u_R\right| < \frac{7}{2}\ \mu_0\ (1+e)\ \left|u_{P1}\right|. \qquad (15668)$$

The relative velocity at the point of contact is determined with the linear and angular velocity components of both particles.

$$\begin{aligned} u_R &= \sqrt{u_{Ry}^2 + u_{Rz}^2}, \\ u_{Ry} &= v_{P1} + \frac{D_{P1}}{2}\ \omega_{P1}^z + \frac{D_{P2}}{2}\ \omega_{P2}^z, \\ u_{Rz} &= -\frac{D_{P1}}{2}\ \omega_{P1}^y - \frac{D_{P2}}{2}\ \omega_{P2}^y. \end{aligned} \qquad (15769)$$

The components of the impulsive force J_y and J_z are dependent on the type of collision. For a **non-sliding collision** one obtains:

$$\begin{aligned} J_y &= -\frac{2}{7}\ u_{Ry}\ \frac{m_{P1}\ m_{P2}}{m_{P1}+m_{P2}}, \\ J_z &= -\frac{2}{7}\ u_{Rz}\ \frac{m_{P1}\ m_{P2}}{m_{P1}+m_{P2}}. \end{aligned} \qquad (15870)$$

and for a **sliding collision** the components of the impulsive force are dependent on the dynamic coefficient of friction μ_d:

$$\begin{aligned} J_y &= -\mu_d\ \frac{u_{Ry}}{u_R}\left|J_x\right|, \\ J_z &= -\mu_d\ \frac{u_{Rz}}{u_R}\left|J_x\right|. \end{aligned} \qquad (15971)$$

Once the new velocities are obtained they are re-transformed into the original co-ordinate system. The above equations show that the parameters involved in the collision model are the restitution coefficient e, and the static and dynamic coefficient of friction. Modelling of inter-particle collisions in the frame of the Euler/Lagrange method for the numerical calculation of two-phase flows has been based mainly on two approaches, a direct deterministic simulation and a stochastic model based on concepts of the kinetic theory of gases. The most straight forward approach to account for inter-particle collisions is the deterministic simulation approach. This requires that all the particles (or in most cases parcels which represent a number of real particles with the same properties) are tracked simultaneously through the flow field. Thereby, the occurrence of collisions between any pair of particles can be judged based on their positions and relative motion during one time step. Once a collision occurs the

change in translational and angular particle velocities can be determined by solving the above equations. This approach is however very time consuming, since at each time step it requires to search for a possible collision partner among the surrounding particles (see for example Tanaka and Tsuji 1991). This search area needs to be properly defined in order not to miss any collisions. Therefore, based on previous work by Sommerfeld & Zivkovic (1992) and Oesterle & Petitjean (1993) a stochastic inter-particle collision model was developed, which

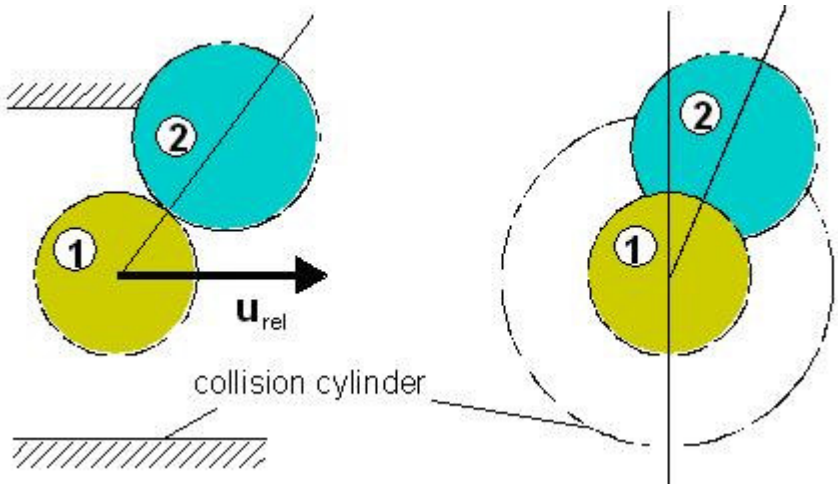

Figure 5.11:Particle-particle collision configuration in a co-ordinate system, where particle (2) is stationary and the axis of the collision cylinder is aligned with the relative velocity vector.

also accounts for the velocity correlation of colliding particles and is much more efficient (Sommerfeld 2001). This stochastic inter-particle collision model is briefly described in the following:

At each time step of the trajectory calculation a fictitious collision partner is generated from the local particle population with previously sampled properties, i.e. with size and velocity sampled from local distribution functions.

In sampling the fictitious particle velocity a possible correlation due to turbulence is respected, which depends on the particle Stokes number.

The collision probability (i.e. the product of collision frequency and time step size) is calculated on the basis of Eq. (13042). If a uniform random number in the interval between zero and one becomes smaller than this probability a collision is occurring.

By transforming the particle velocities into a coordinate system where the fictitious particle is stationary, it is possible to sample the point of impact which only can be located on the hemisphere facing the fictitious particle.

The new velocities of the considered particle are calculated based on the equations introduced above (i.e. Eqs. (15062) and (15971)).

Finally, the particle velocities are re-transformed into the original coordinate system. The fictitious particle is not of further interest.

Fluid dynamic effects during the collision process may be neglected if the duration of the collision process is negligibly small compared to the time of collisionless motion, the size of the colliding particles is not too different, and the ratio of solid particle density to the fluid density is much larger than unity. Hence under such conditions the collision efficiency may be assumed to be 100 %.

5.2.3 Inter-particle Collision Effects in Turbulent Flows

The following results were obtained with the stochastic inter-particle collision model as described above. The first case considered is a cube with homogeneous isotropic turbulence without gravity, which was analysed in detail by Lavieville et al. (1995) using large eddy simulations (LES). Information on the turbulence characteristics are provided in Sommerfeld (2001). The collision detection algorithm adopted in the LES required to consider rather large particles (i.e. $D_p = 656\ \mu m$). The variation of the particle Stokes number was achieved by considering particles with different material density.

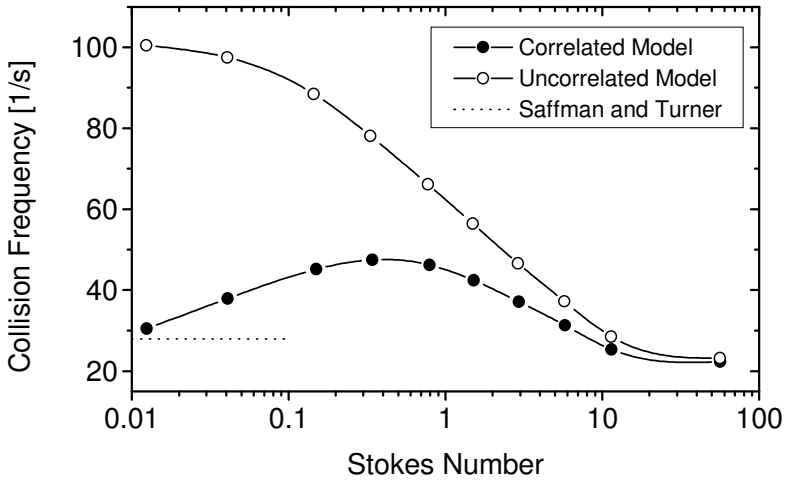

Figure 5.12: Dependence of the simulated collision frequency on the particle Stokes number, comparison of uncorrelated and correlated collision model ($\alpha_P = 0.0176$).

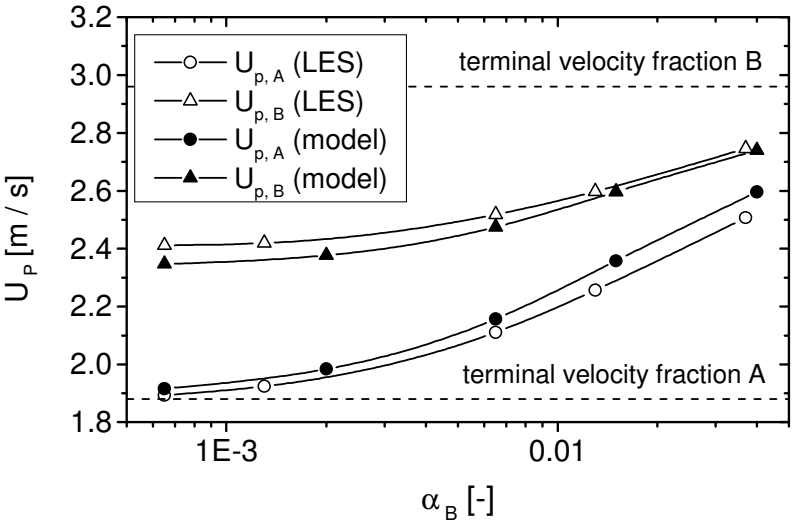

Figure 5.13: Mean particle velocities for fraction A and B, comparison of model calculations with LES data for a binary mixture settling under gravity ($\alpha_P = 0.013$).

The collisions were assumed to be fully elastic (i.e. $e = 1.0$, $\mu = 0.0$). These results served a test case for validating the stochastic collision model. Figure 5.12 shows the collision frequency obtained from the model calculations for a wider range of Stokes numbers. As expected, the uncorrelated model predicts a continuous increase of the collision frequency with decreasing Stokes number. The correlated model however, predicts a maximum in the collision frequency for a Stokes number of about 0.4.

For smaller Stokes numbers a decrease of the collision frequency is found and in the limit of

particles completely following the turbulent fluctuations (i.e. $St_t \rightarrow 0$) the value predicted by Saffman and Turner (1961) is approached. Hence, the developed correlated collision model correctly predicts the collision rates in isotropic homogeneous turbulence (see Sommerfeld 1999 and 2001 for further results).

In the second case a binary mixture of particles with the same size, but different material density, settling under the action of gravity (i. e. $g_x = 49.05\ m/s^2$) in a cube with homogeneous isotropic turbulence is considered (Sommerfeld 2001). The particle size was $650\ \mu m$ and the two material densities were $\rho_A = 117.5\ kg/m^3$ and $\rho_B = 235\ kg/m^3$, respectively. The volume fraction of class A particles was fixed with $1.3 \cdot 10^{-2}$ and that of class B particles was varied between $6.5 \cdot 10^{-4}$ and $4 \cdot 10^{-2}$. Only completely elastic collisions were considered in the simulations (i.e. $e = 1.0,\ \mu = 0$). In this test case the collisions between particles are mainly determined by the mean drift between the two particle fractions as a result of their different terminal velocity. In addition collisions are induced by the fluctuating motion of the particles, which is partly caused by turbulence. Hence, the collisions between the two particle fractions causes a momentum transfer between the two fractions, whereby the mean velocity (i.e. in the direction of gravity) of the light particles (fraction A) becomes larger than their terminal velocity and for the heavy particles the settling is hindered by collisions with the light particles (Figure 5.13).

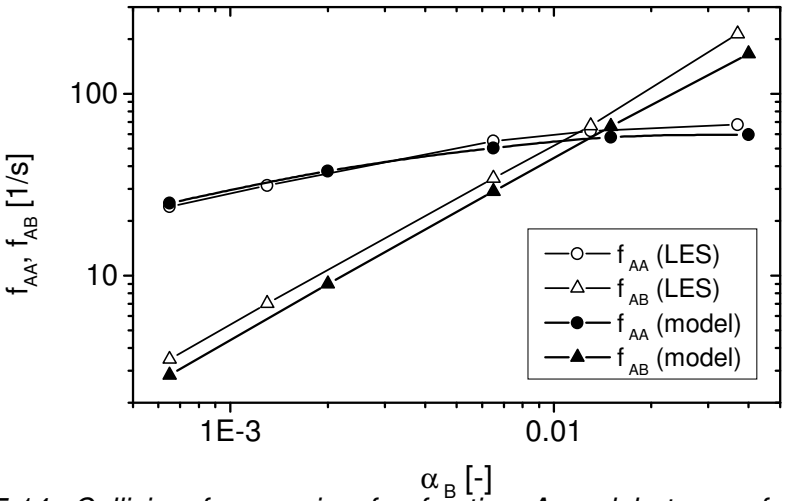

Figure 5.14: Collision frequencies for fraction A and between fraction A and B, comparison of model calculations with LES data for a binary mixture settling under gravity.

At low volume fractions of class B particles, the heavy particles are strongly hindered by the light ones and hence the heavy particle mean velocity is about 19 % smaller than their terminal velocity. With increasing volume fraction of class B, the heavy particles drag the light particles (A) and their mean velocity increases, while the mean velocity of the heavy particles also increases and approaches the expected terminal velocity. These effects are well reproduced in the model calculations and the agreement with the LES results is reasonably good. Considering the collision frequencies for this case (Figure 5.14), it is found that f_{AA} increases with the concentration of fraction B due to an increase of the fluctuating motion of fraction A. The collision frequencies between fractions A and B (i.e. f_{AB}) increase mainly due to the increase of the volume fraction of the particles fraction B. The agreement of the model calculations with the LES-results is reasonably good for this case. More details on the test cases and additional results can be found in Sommerfeld (2001).

5.3 Heat and mass transfer in droplets and sprays

Theoretical Background

Heat and mass transfer will play an important role, for instance, when liquid droplets are placed in a hot carrier gas. The liquid droplets will heat up and vaporize. The diameter and the temperature of the droplets in a spray will change and the composition and temperature of the carrier gas will change accordingly. The liquid droplet mass vaporization $\dot{m}_p = \frac{dm_p}{dt}$ for spherically symmetric droplets can be derived exactly under simplified conditions is given by the equation

$$\frac{dm_p}{dt} = \pi d_p \rho_g ID_g Sh_g \ln(1 + B_M), \qquad (16072)$$

with m_p the droplet mass and d_p the droplet diameter. ρ_g, ID_g and Sh_g are the density, binary diffusion coefficient and Sherwood number of the gas phase.

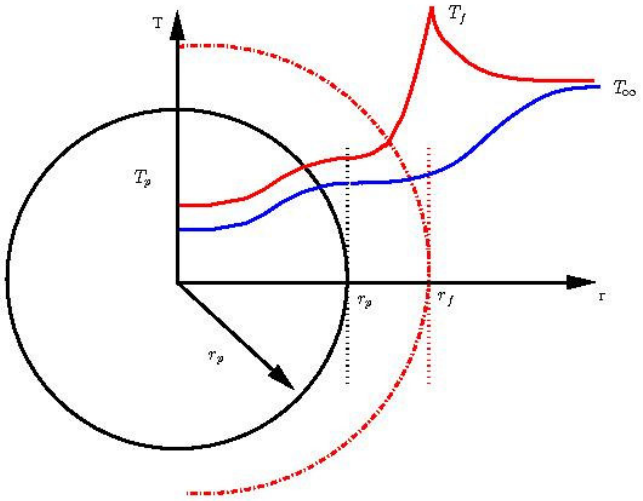

Figure 5.15: Temperature profiles for an isolated vaporizing (blue line) droplet and a burning (red line) droplet

Figure 5.15 shows a sketch of the temperature profile around a vaporizing or burning droplet. Since the vapour coming from the droplet diffuses with a finite speed, the mass fraction and temperature around the droplet is not uniform. The gas phase thermodynamic properties can be evaluated 'faraway' from the droplet, where the gas field is not affected by the presence of the droplet, or they can be evaluated at a certain reference mass fraction and temperature (Y_m, T_m). We will discuss this in more detail later. The Sherwood number, which describes the relative importance of convection compared to mass diffusion, is usually obtained using the empirical correlations of Ranz-Marshall:

$$Sh = 2 + 0.552 Re_p^{\frac{1}{2}} Sc_g^{\frac{1}{3}}, \qquad (16173)$$

where Sc_g is the Schmidt number $Sc_g = \mu_g / \rho_g ID_g$ and Re_p the droplet Reynolds number. The Spalding mass transfer number B_M is a measure for the eagerness of the droplet to evaporate. It can be defined as

$$B_M = \frac{Y_s - Y_\infty}{1 - Y_s}, \qquad (16274)$$

where Y_s is the vapor mass fraction at the surface of the droplet. If no vapour was present in the gas phase before the droplet started to evaporate, then $Y_\infty = 0$. Y_s is obtained (assuming thermodynamic equilibrium) from the saturation pressure p_{sat} determined by the Clausius-Clapeyron equation. The equation gives the surface equilibrium mole fraction:

$$X_{\text{surf}} = \frac{p_{\text{sat}}}{p_{\text{atm}}} = \exp\left[\frac{L_V}{RW_V}\left(\frac{1}{T_B} - \frac{1}{T_p}\right)\right], \qquad (16375)$$

where $R = 8.314 J \cdot K^{-1} \cdot \text{mol}^{-1}$ is the universal gas constant, W_V is the vapor molar mass and T_B is the boiling temperature of the liquid. L is the latent heat of vaporization of the liquid. The surface mass fraction Y_s can be calculated using

$$Y_s = \frac{X_s}{X_s + (1 - X_s)\frac{W_\infty}{W_V}}, \qquad (16476)$$

where W_∞ is the molecular weight far from the droplet (usually air). The equation for the vaporization rate may be rewritten into an equation for the square of the droplet diameter, which is known as the 'd^2' law. We rewrite the mass vaporization rate as

$$\frac{dm_p}{dt} = \rho_p \frac{\pi}{6}\frac{d\left(d_p^3\right)}{dt} = \rho_p \frac{\pi}{6}\frac{d\left(d_p^2\right)^{3/2}}{dt} = \rho_p \frac{\pi}{6}\frac{3}{2} d_p \frac{d\left(d_p^2\right)}{dt}, \qquad (16577)$$

such that Eq. (16072) can be written in terms of the evolution of the square of the droplet diameter:

$$\frac{d\left(d_p^2\right)}{dt} = \frac{4}{\rho_p}\rho_g I D_g^b Sh_g \ln\left(1 + B_M\right) = K. \qquad (178)$$

When all thermodynamic properties are assumed to be constant during the droplet lifetime, then K is a constant and the droplet diameter evolution can be described as

$$d_p^2(t) = d_{p,0}^2 - Kt, \qquad (179)$$

which is known as the d^2 law. The droplet lifetime follows from Eq. (179) and is $t_p = d_{p,0}^2 / K$.

Determining the reference thermodynamic properties

In the presence of evaporation, the composition of the gaseous phase immediately surrounding the droplet will change (due to the vapour mixing with the gas). So not only the temperature dependence but also the composition dependence of the gas phase properties should be considered. When we suppose that the state of the gaseous phase is fully described by (Y,T), then we have in principle:

$$\lambda_g(Y,T), \quad \rho_g(Y,T), \quad \mu_g(Y,T) \quad \text{and} \quad c_{pg}(Y,T), \qquad (180)$$

where the value of (Y,T) may vary from the droplet surface value (Y_s,T_p) to the undisturbed fluid flow value (Y_∞,T_∞). Miller *et al.*(1998) mention several works showing a

strong dependence of results obtained from numerical simulations on the choice of property values. The most popular method is an averaging method known as the '1/3' rule [?]. The vapour mass fraction and temperature (Y_m, T_m) at which the gas phase properties will be evaluated are determined using:

$$T_m = T_p + \frac{1}{3}\left(T_\infty - T_p\right) \quad \text{and} \quad Y_m = Y_s + \frac{1}{3}\left(Y_\infty - Y_s\right). \qquad (181)$$

Yuen and Chen (1974) also advocate the use of a '1/3' rule to calculate the dynamic viscosity used to determine the droplet Reynolds number:

$$\mu_m = \mu_s + \frac{1}{3}\left(\mu_\infty - \mu_s\right). \qquad (182)$$

Chen and Pereira (1996) use the 1/3-rule to evaluate μ, λ and c_p at (Y_m, T_m). However, the density ρ_g appearing in Re_p is evaluated from the undisturbed fluid flow conditions (Y_∞, T_∞), such that:

$$Re_p = \frac{\rho_\infty \left|U_p - U_\infty\right| d_p}{\mu_m}. \qquad (183)$$

The details of determining thermodynamic gas and gaseous mixture properties can be found in reference works like Poling, Prausnitz and O'Connell (2001). Tables with polynomial fits for certain thermodynamic properties like specific heat are used by the thermodynamic database of CHEMKIN, which are described in detail in their manuals Kee *et al.* (1997)a and Kee *et al.* (1997)b.

Particle heat transfer

The droplet temperature evolution is determined by a balance between conductive heating and evaporative cooling. When the liquid thermal conductivity is infinitely fast, the temperature of the droplet can be considered uniform, but time-varying. The temperature evolution of the droplet is then given by:

$$m_p c_{p,l} \frac{dT_p}{dt} = Nu\pi\lambda_g (T_\infty - T_p) - L\dot{m}_p. \qquad (184)$$

In this equation, $c_{p,l}$ is the liquid heat capacity, λ_g is the thermal conductivity of the gas phase and Nu is the Nusselt number. The Nusselt number, which tells about the relative importance of convection over heat diffusion, can also be determined with a Ranz-Marshall correlation:

$$Nu = 2 + 0.552 Re_p^{1/2} Pr_g^{1/3}, \qquad (185)$$

where the Prandtl number is defined as

$$Pr_g = \frac{\mu_g c_{pg}}{\lambda_g}, \qquad (186)$$

The droplet temperature equation can be solved exactly for small timesteps Δt, in which all properties are assumed to be constant during the timestep. The general solution of an equation of the form

$$\frac{dT_p}{dt} = \omega(T_\infty - T_p) - C, \qquad (187)$$

with known initial conditions $T_p(t)$ is given by

$$T_p(t+\Delta t) = T_p(t) + (T_\infty - T_p(t))(1 - e^{-\omega\Delta t}) - C(1 - e^{-\omega\Delta t}). \qquad (188)$$

Due to the balance between heating and cooling, liquid droplets usually do not reach the boiling point of the liquid when they are heated. Instead, the temperature evolves towards the wet-bulb temperature. An estimation of the wet-bulb temperature can be obtained by setting the left-hand side of Eq. (184) to zero (Crowe, Sommerfeld, and Tsuji 1998). When droplets are placed in a very hot carrier gas, they will reach the wet-bulb temperature quickly. The wet-bulb temperature can then be used instead of the evolution equation of the droplet temperature. When the carrier gas is hot and the boiling point of the liquid is low, the wet-bulb temperature will be close to the boiling temperature of the liquid. The standard d^2 law together with an infinite conductivity model for the droplet temperature typically overpredicts the vaporization rate, leading to shorter droplet lifetimes. Some corrections have been proposed in the literature Abramzon and Sirignano (1989), Miller, Harstad and Bellan (1998), Sazhin (2006). We will consider two of them, the model of Abramzon and Sirignano and the model of Miller, Harstad and Bellan.

Model of Abramzon and Sirignano

In Abramzon and Sirignano (1989), the effect of Stefan flow (which is the flow of vapour coming from the droplet in the outward radial direction) is taken into account and the Sherwood and Nusselt numbers are corrected using

$$Sh^{\text{å}} = 2 + \frac{Sh - 2}{F_M}, F_M = \frac{(1+B_M)^{0.7}}{B_M}\ln(1+B_M), \qquad (189)$$

$$Nu^{\text{å}} = 2 + \frac{Nu - 2}{F_T}, F_T = \frac{(1+B_T)^{0.7}}{B_T}\ln(1+B_T), \qquad (190)$$

with

$$B_T = (1+B_M)^{\phi}, \phi = \frac{c_{p,v}}{c_{p,g}}\frac{Sh^{\text{å}}}{Nu^{\text{å}}}\frac{1}{Le}, \qquad (191)$$

with $c_{p,v}$ the specific heat of the vapour and $c_{p,g}$ the specific heat of the gas (air) determined using the 1/3 rule for temperature and mass fraction. Equations (190) and (191) are solved iteratively by first determining the $Le = \frac{\lambda_g}{\rho_g ID_g c_{p,g}}$, F_M and Sh, and then use an initial guess for B_T (e.g. $B_T = B_M$) to subsequently determine F_T, Nu, ϕ and B_T. When $|B_{T_{\text{old}}} - B_{T_{\text{new}}}| > \varepsilon$ with ε a small value, we replace the initial guess for B_T with our new B_T and continue until B_T has converged. B_T is then used in the temperature equation as:

$$m_p c_{p,l}\frac{dT_p}{dt} = \frac{c_{p,v}(T_\infty - T_p)\dot{m}_p}{B_T} - L\dot{m}_p. \qquad (192)$$

Model of Miller, Harstad and Bellan

In Miller *et al.*(1998), a modification to the heat transfer equation, termed the Langmuir-Knudsen model by Harstad *et al.*, was used. The first term on the right-hand side of Eq. (184) is corrected by a factor G,

$$G = \frac{\beta}{e^{\beta} - 1}, \qquad (193)$$

where β is the nondimensional evaporation parameter:

$$\beta = -\frac{3 Pr_g \tau_p}{2} \frac{\dot{m}_p}{m_p}, \qquad (194)$$

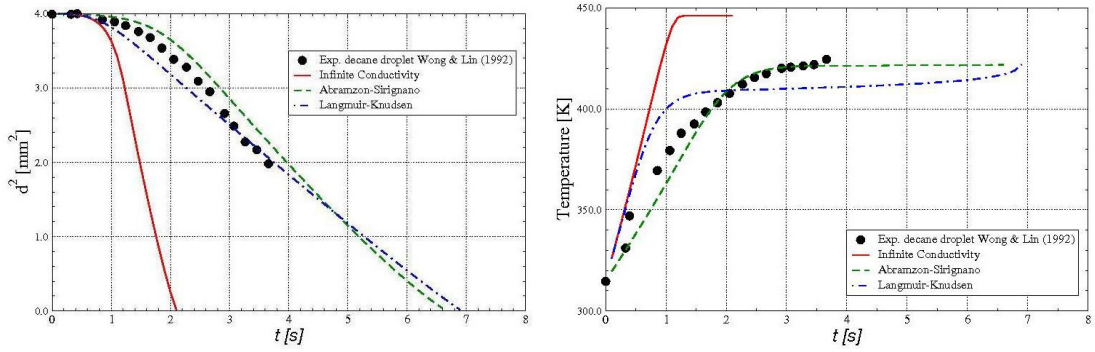

Figure 5.16: Temporal evolution of the droplet diameter squared and the droplet temperature for a $d_p = 4.0$ mm decane droplet vaporizing in a $T_\infty = 1000$ K environment with an initial Reynolds number of $Re_p = 17.0$. Experimental results from Wong and Lin (1992). Reference conditions used for the simulations are the $'1/3'$ rule.

\with τ_p the droplet relaxation time in Stokes flow, $\tau_p = \frac{\rho_p d_p^2}{18 \mu_g}$. This correction yielded good results for several single droplet simulations. Some typical results for the diameter and temperature evolution of a vaporising droplet can be seen in Figure 5.16.

Guidelines for droplet and spray modeling with heat and mass transfer.

Before doing a spray simulation including heat and mass transfer, it is advised to first do some calculations on single droplets. Check if the predictions of the temperature and diameter evolution of a single droplet correspond with experimental data. Check how sensitive it is to the chosen reference conditions.

Attention should be paid to the balance between heat and mass transfer in the dispersed phase and in the gas phase. When droplets heat up, the same amount of heat should be subtracted from the gas phase. When droplets vaporize, the corresponding amount ofmass vapour should be added to the gas phase.

Because a lot of thermodynamic data or correlations are available in different units (Joules or Calories, meters or feet), it is advised to recast all data into your preferred units before using it. Unit conversions in a computer code may be very confusing and distractive.

In burning hydrocarbon sprays, it is seldom observed that droplets burn with an individual flame surrounding the droplet. Droplets can therefore be assumed to vaporize in a hot environment.

6 Sources of errors

It is advised to read the "source of errors" section in the BPG for single phase flows prior to reading the BPG of multiphase flow modeling. If a procedure is adopted which leads to unsatisfying results for a single phase flow computation, this generally leads to errors in a multiphase flow computation as well. Discretisation errors, round-off errors and modeling errors have the same type of impact on multiphase flow computations as on single phase flow computations. However, there is a much broader spectrum for sources of errors for multiphase flow computations, of which a number of major ones are listed below.

- Not knowing the most important physical mechanisms

Although the last 30 years or so, there has been an enormous development of multiphase flow models, the field of research is certainly not finished or complete. Because of its complexity there is not one "generic" model for multiphase flows or a generally applicable closure model. Before undertaking an attempt to model a multiphase flow system, it is vital to understand the physics of the flow system. This includes understanding the most important forces and mechanisms occurring in the flow, the properties of the fluid(s) and/or solids, as well as a good estimate of the length and time scales of the processes carried out. Only by knowing this, a good selection of governing models and closure models can be made.

- Closure models

Probably the major sources of errors in multiphase flow computations are due to shortcomings of the closure models. Most industrial multiphase flow calculations will require a number of closure models, for instance to model forces and interactions between phases. Such closure models are most often empirically determined, which makes them applicable only under similar conditions as the data they are built from. It is important to select closure models which are applicable to the specific phenomena occurring in the flow to be modeled, and which are valid for similar conditions (in terms of Re, St, We, …) as the real flow.

- Time and length scale separation

In the derivation of single-phase turbulence models, almost always a separation between the time and length scales of the eddies carrying the energy (large eddies) and the eddies at which energy is dissipated (small eddies) is assumed. Without this assumption, most closure models for turbulence do not hold. A similar assumption is required for the derivation of governing equations and a number of closures. Most closures for turbulent multiphase flow require a separation between the scale of the energy carrying eddies and the scale of the dissipation. Only then does the Boussinesq assumption, employed for instance in deriving the popular kinetic theory of granular flow hold. Another example lies in the derivation of the two-fluid or Eulerian-Eulerian model; as the parameter for volume fraction is an averaged quantity, the fluctuations of the volume fraction have a different meaning then the fluctuations of velocity.

As specified under the first point, it is important to have an understanding of the time and length scales of the physical mechanisms occurring in the multiphase flow, as this can have consequences for the governing equations as well as choice of closure models.

- Governing equations

Although there is no dispute regarding the governing equations describing single phase flow, there is still no general agreement on the exact form of the governing equations describing multiphase flow. For instance, there exist at least 4 different types of the popular "two-fluid" model, where the most employed ones are called "A" and "B". Most arguments regarding this discrepancy are regarding the stability of the model; it is said by a number of researchers that the classical two-fluid model as proposed by Ishii (1975) can exhibit exponential growth under specific conditions, and this is not acceptable. Moreover, it is generally known that there is a (too) large dependency upon the grid spacing and the time-step for such models.

It is advised to employ the selected governing equations on one or a number of cases which have a known solution. This solution can be of the same system and carefully validated by experiments, or by a similar system from the Ercoftac database.

- Numerical errors

Multiphase flow calculations can have the same type of numerical errors as single phase calculations; it is therefore advised to check the BPG for single phase flow as well.

However, there may be additional problems. Most multiphase flow solving algorithms are based upon single-phase ideas. Examples of these are pressure correction methods (SIMPLE, PISO), discretisation schemes (such as shock capturing, flux splitting). Although many of these ideas seem to work for a number of multiphase flows as well, there is little fundamental research supporting this in general. Solving the equations describing multiphase flows is generally a much more difficult task then solving the single phase counterpart, and errors may arise from the shortcomings of today's algorithms.

7 Industrial examples for multiphase flows

7.1 Bubble column

The bubble column is a frequently used chemical reactor. It is in most cases a cylindrical vessel (with the symmetry axis vertically) in which a liquid is in batch. Gas is fed in the form of jets or bubbles into the liquid in the lower part of the reactor, via e.g. a ring sparger or a perforated plate. Various levels of sophistication of dealing with these reactors exist.

The coarsest level is the mixture model with a constant bubble size and a constant slip velocity. This computation is 'fast' and can provide a first estimate of the flow field. It is useful when not only the flow field needs to be solved, but also additional mixing, mass & heat transfer and chemical reaction need to be simulated. Subsequently, the bubble size may

change or the slip velocity may be model more realistic. A good example of this approach is given in Bauer and Eigenberger (1999) and Bauer and Eigenberger (2001).

To speed up simulations one could assume cylinder symmetry and run computations in 2D rather than 3D. This gives of course, results at much lower computational costs. However, care should be taken with the results as it is well known that the 2D simulations significantly dampen the possible natural fluctuations occurring in bubble columns (Ranade and Tayalia, 2001). It has been show for a bubble plume in a flat rectangular column (Becker et al. 1994, Sokolichin and Eigenberger 1999, Mudde and Simonin 1999) that the oscillations present in the real experiment can only be captured in 3D simulations: 2D simulations over predict the turbulent viscosity damping completely the fluctuations and structures in the flow. 2D simulation should be used with care and considered mainly for a first impression of the flow field.

Example 1: Influence of the sparger.

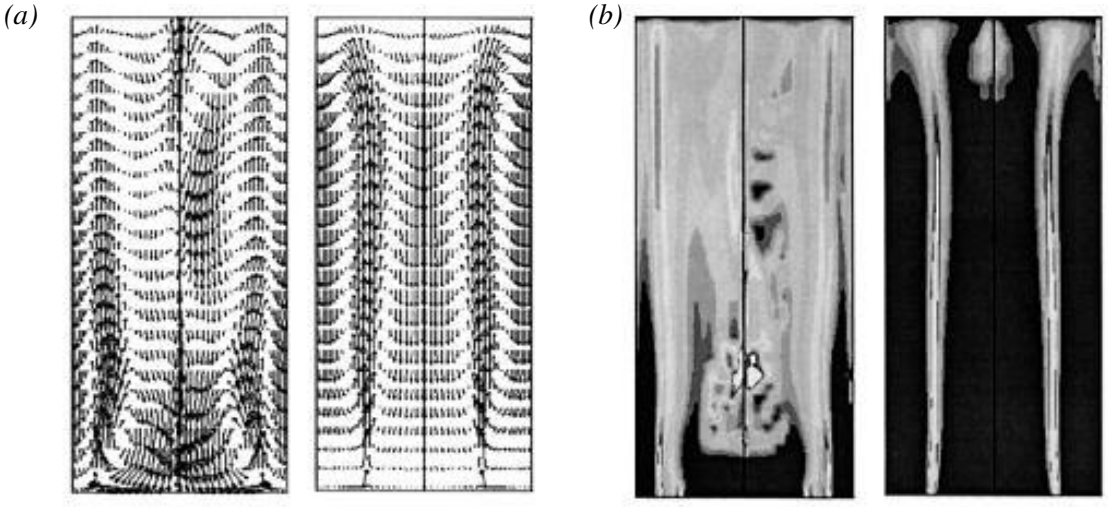

Figure 7.1: (a) - Instantaneous flow field for a superficial gas velocity of 1cm/s. left: double ring sparger, right: single ring (Ranade and Tayalia, 2001), (b) - Instantaneous gas fraction for a superficial gas velocity of 1cm/s. left: double ring sparger, right: single ring (Ranade and Tayalia, 2001).

Ranade and Tayalia (2001) used CFD to investigate the influence of the gas sparger design on the flow properties of a shallow bubble column. The flow was described via a two-fluid approach with a standard k-ε turbulence model. For the interaction force between the phases, the drag relation of Schwarz and Turner (1988) was taken $F_D = -5\times10^4\,\alpha(1-\alpha)\left(U_g - U_l\right)$, with U_g and U_l the gas phase and liquid phase velocity, respectively. The geometry modelled is a shallow column with a diameter of 1m and a height of 2m. Two different spargers were tested, located in the bottom: a single ring and a double ring (diameters 0.48 and 0.78m, respectively). The bubble size in the simulations was 4.5mm. The finest grid used had 194304 cells, whereas the coarsest only 24288. The simulations were carried out with the commercial package FLUENT 4.5.

Example 2: The Eulerian-Eulerian model versus the mixture model

Dudukovic and co-workers investigated the difference between simulations of a bubble column using a full two-fluid and a mixture model. In Sanyal et al. 1999 two-dimensional simulations are reported for a superficial gas velocity of 2.0cm/s and 12.0cm/s. The results are compared with data from the CARPT technique in the group of Dudukovic. Especially, for the higher gas velocity, industrial flow rates are approached.

The simulations show, that reasonable quantitative agreement between the simulations and the experiments are found. According to the authors, the simulations provide good engineering descriptions, and can de used reliably for approximately predicting the time-averaged flow and hold up patterns in bubble columns; see Figure 7.2 and Figure 7.3 respectively.

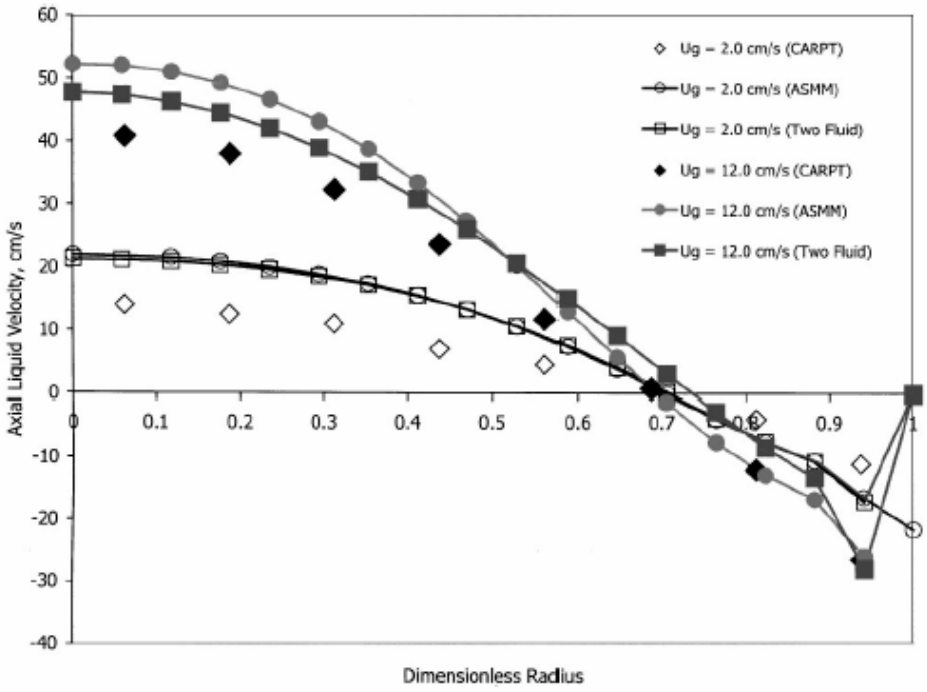

Figure 7.2: Axial time-averaged liquid velocity: comparison between experiment and simulation (from Sanyal et al. 1999).

The results show further, that even for the high gas velocity case (i.e. U_{sup} = 12.0 cm/s the predictions of the simulations are reasonable. Note that for this case the bubble column is in the heterogeneous regime: at these high velocities significant break up and coalescence should occur and thus a wide bubble size distribution is expected. The above described simulations do not consider this and work with a fixed bubble size.

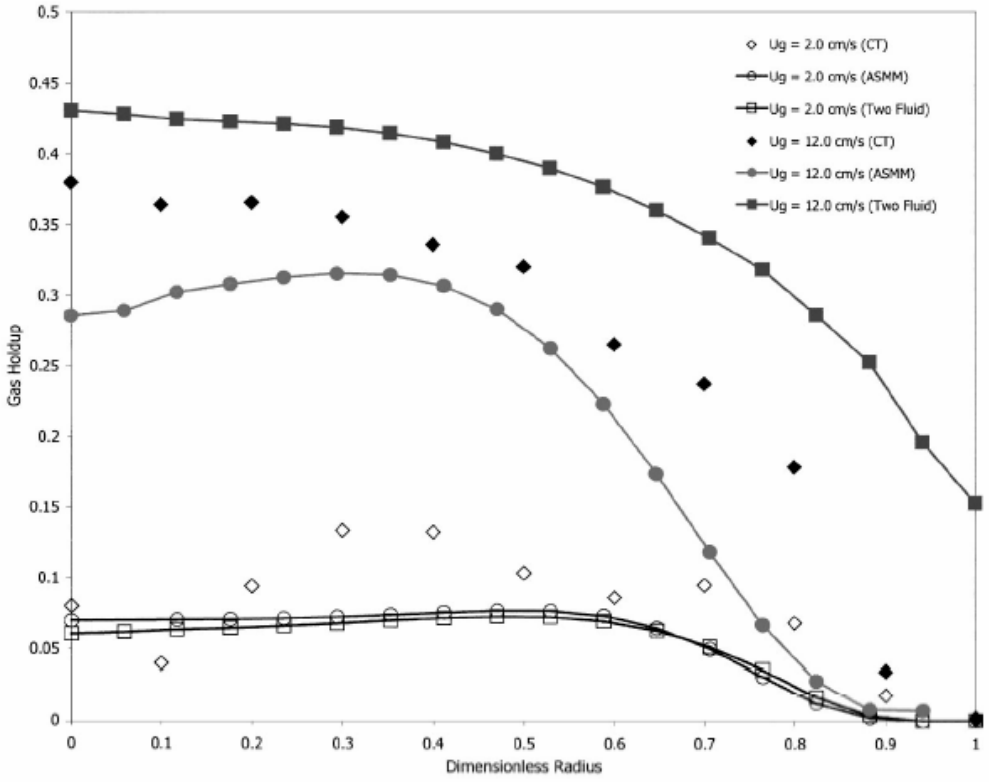

Figure 7.3: Gas fraction profiles: comparison between experiment and simulation (from Sanyal et al. 1999).

Coalescence & break up. Bubbly flows like in a bubble column show a narrow bubble size distribution only for special conditions, usually found in laboratory equipment. Many of the industrial applications operate with ring sparger or a few wholes in bottom plate. This way bubbles are formed from a jet that is broken up. Moreover at higher gas fractions and higher superficial gas velocities bubbles coalesce and might break up do to the turbulence present in the flow. In principle, this should be incorporated into the simulations. In the Euler-Euler description this is done by modelling the gas phase as existing of a finite number of bubbles of different size. For each of these bubbles a mass and momentum balance is set up and solved simultaneously with those of the liquid phase. Bubble coalescence and break up is incorporated leading to a dynamic system in which a so-called bubble population balance is tracked. Several models for coalescence and break up exist. Amongst the most often used are those from Prince & Blanch (1990) and Luo and Svendsen (1996), and Andersson et al (2006).

Further modelling is required for the gas phase velocity: each bubble size can have its own field, making the computations expensive. However, assuming a mean bubble velocity will reduce the required computational load at the expense of accuracy. The same holds for invoking mixture models in which a slip velocity can be defined for each bubble class or for all bubbles.

The general expression for the bubble population balance, i.e. the bubble size distribution, reads as:

$$\frac{\partial}{\partial t} f(\vec{x},t,v) + \nabla \cdot \left[\vec{u}_b(\vec{x},t,v) f(\vec{x},t,v) \right] = S(\vec{x},t,v), \qquad (195)$$

with $f(\vec{x},t,v)$ the bubble number density function representing the probability of finding a

bubble with volume between {v,v+dv} at a given time t at position { $\vec{x}, \vec{x} + d\vec{x}$ }. The velocity $\vec{u}_b(\vec{x}, t, v)$ is the local velocity of bubbles with volume between {v,v+dv}. $S(\vec{x}, t, v)$ acts as a source term and describes the change of the number density due to coalescence and break up.

This source term involved birth and death integral for various bubble sizes, for which theoretical models are available. However, these models have not been tested rigorously. Various techniques exist to solve the population balance. The continuous population balance can be discretised, only n subclasses of bubble size are tracked, or only the moments of the distribution are calculated (see e.g. Sanyal et al. 2005).

In Chen et al. 2005 a comparison is made between experiments and CFD simulations of a bubble column including coalescence and break-up. Three different modelling approaches are compared: a two-fluid model with all bubbles moving at the ensemble averaged mean velocity of the dispersed phase; a mixture model with all bubbles moving at the ensemble averaged mean velocity of the dispersed phase; a mixture model with N+1 phases and different bubble size moving with different velocities. The results are compared to experimental data of the time-averaged liquid velocity and the hold up. It was found that the two fluid model gives the best results, followed by the mixture model with different velocities. There was reasonable agreement as a function of system pressure (up to 10 bar) and for different gas-liquid systems.

Krishna and co-workers (e.g. Van Baten and Krishna 2001) take an engineering approach to the above problem: they divide the bubbles into two classes: small and large and provide engineering rules for the population of these two classes. However, this is an approximation that can not deal with the dynamics of coalescence and break up.

7.2 Air Lift

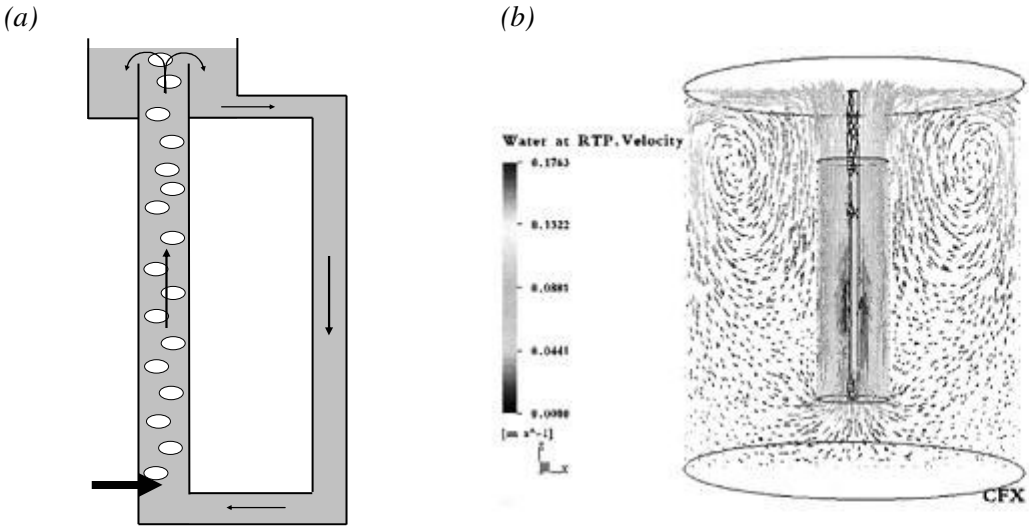

Figure 7.4: (a) - Air lift reactor with external downcomer, (b) - CFD result from Vesikar and Al-Dahhan.

Air lift reactors form another class of gravity driven bubbly flows. Here, the reactor consists of a loop: i.e. two vertical sections connected at top and bottom. One of the vertical sections is gassed (see Figure 7.4(a)). This gas is taken of at the top, thereby creating a density difference

between the gassed part (the riser) and the un-gassed part (the down-comer). Gravity will induce a circulation of the liquid phase, with up flow in the riser and down flow in the down-comer. These reactors can also be modelled via CFD. The flow is usually much more organized than in the bubble column: it is predominantly 1-dimensional although flow structures have been reported. A full 3D simulation can capture this best. Moreover, the degassing zone breaks the simple 1D description: this part is essentially multi-dimensional. Several examples can be found in literature.

Vesvikar and Al-Dahhan investigated the flow in an anaerobic digester, equipped with an internal draft tube. They used a steady state description and found reasonable agreement for the flow patterns between the CFD results and their experimental data (from CARPT). Nevertheless, the authors conclude, that the CFD simulations were not able to match the experimental data accurately and that different closures are needed.

Cockx et al. 1997 investigated the bubbly flow in an internal air lift. Their reactor is a rectangular box, with a splitter plate in the middle separating the gassed riser from the un-gassed down-comer. A simple 1-dimensional model is presented from which the hydrodynamic parameters, such as the volume fraction and circulation velocity, can be estimated. This model needs to be closed by models for the wall friction. A numerical study of the same device is carried out using the ASTRID code.

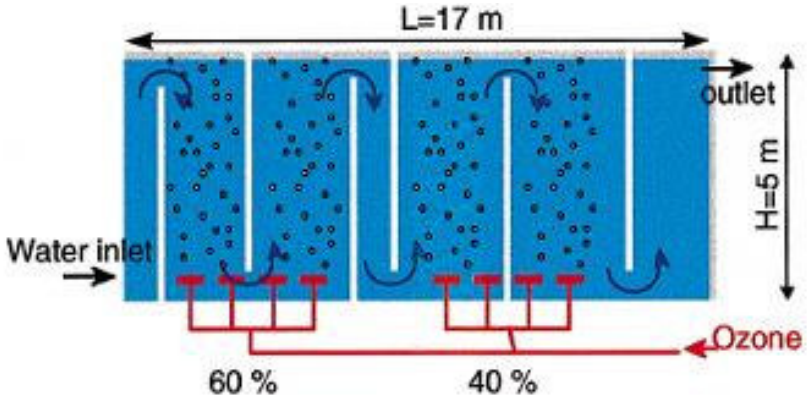

Figure 7.5: Industrial Ozone tower considered by Cockx et al., 1999.

In Cockx et al. 1999, an industrial ozonization tower is investigated using the ASTRID code. Both the hydrodynamics and the mass transfer are studied. The reactor has a volume of 350m^3. Due to this large scale, only the two-fluid approach can be used to study the entire device.

For the mass transfer, an additional set of mass balance equation has to be solved. The concentration c_k is split in an average C_k and its fluctuating part c'_k. The average concentration of the Ozone is governed by the following mass balance:

$$\frac{\partial}{\partial t}\alpha_k C_k + \nabla \cdot \alpha_k C_k \vec{U}_k = \alpha_k S_k - \nabla \cdot \alpha_k \left(\vec{J}_k + \left\langle c'_k \vec{u}'_k \right\rangle \right) + \left\langle c_k m_k \right\rangle + L_k, \quad (196)$$

with S_k reaction term, J_k representing the molecular diffusion (using a Fickian description), m_k the mass transfer between the phases and L_k the interfacial transfer of concentration between the phases. Coalescence and break up are not considered. The turbulence is taken into account via a k-ε model for the liquid phase and Tchen's model for the bubble phase.

The CFD results were compared to RTD measurements using salt injection. The agreement is good. An example of the CFD predictions for the gas phase volume fraction is given in Figure 7.7.

The CFD results were useful for further upgrading of the installation.

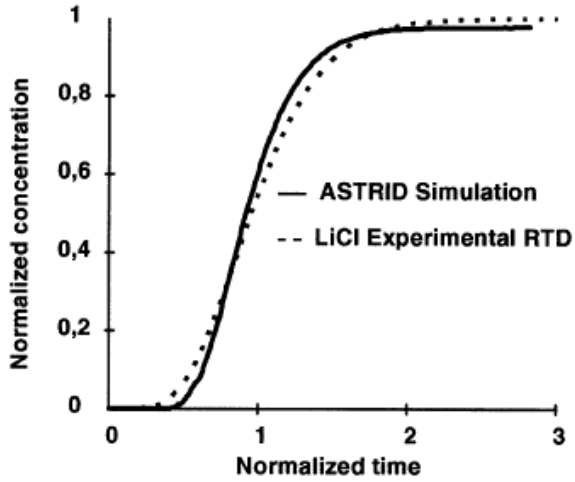

Figure 7.6: RTD curves from experiment and simulation, Cockx et al., 1999.

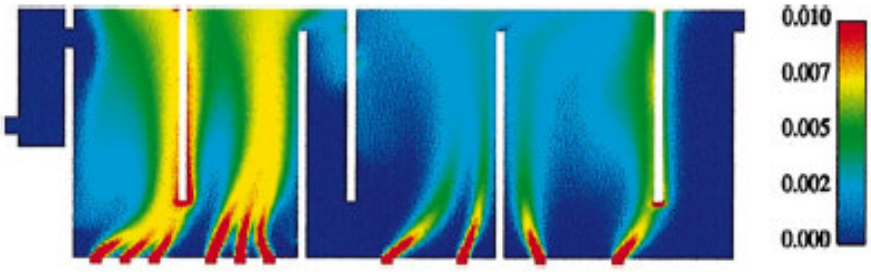

Figure 7.7: Gas phase volume fraction from simulation, Cockx et al., 1999.

Oey et al. 2001 investigated a three-phase flow in an internal air lift (see Figure 7.8). Their two-fluid model used the concept of the drifting velocity. Furthermore, they implemented the added mass force as well as the fluctuating part of that. The turbulence was dealt with via the standard k-ε model, adapted for the effects of the dispersed phase. The simulations were done with the in-house developed 2-D DISSIM code.

A simple mechanical energy balance was employed to estimate the liquid circulation rate for the bubbly flow. A comparison with the CFD simulations gives reasonable results. For the three-phase case, the solid-liquid mixture was treated as a quasi-single phase and the flow in the air lift was simulated using the two-fluid approach. The solids distribution was analyzed using a slip model: rather then solving a separate mass and momentum equation for the solids, the solids distribution was obtained from the solids mass balance. The velocity of the solids is taken as the sum of the liquid velocity, plus a fixed slip velocity and the solids drifting velocity:

$$\frac{\partial}{\partial t}\alpha_3 + \nabla \cdot \alpha_3 \left(\vec{v}_{liq} + \vec{v}_{slip} + \vec{v}_{drift} \right) = 0, \qquad (197)$$

with for the drift velocity a similar formulation as used in two-fluid bubbly flows:

$$\vec{v}_{drift} = -D_{13}^{t} \left[\frac{\nabla \alpha_3}{\alpha_3} - \frac{\nabla (1-\alpha_3)}{1-\alpha_3} \right]. \qquad (198)$$

The diffusion coefficient is modelled according to the theory of Simonin.

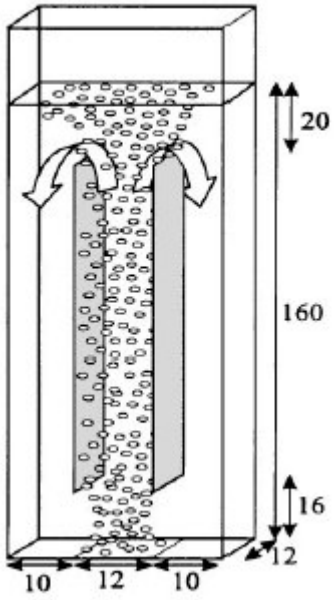

Figure 7.8: Air lift used by Oey et al., 2001. (dimensions in cm).

(a) *(b)*

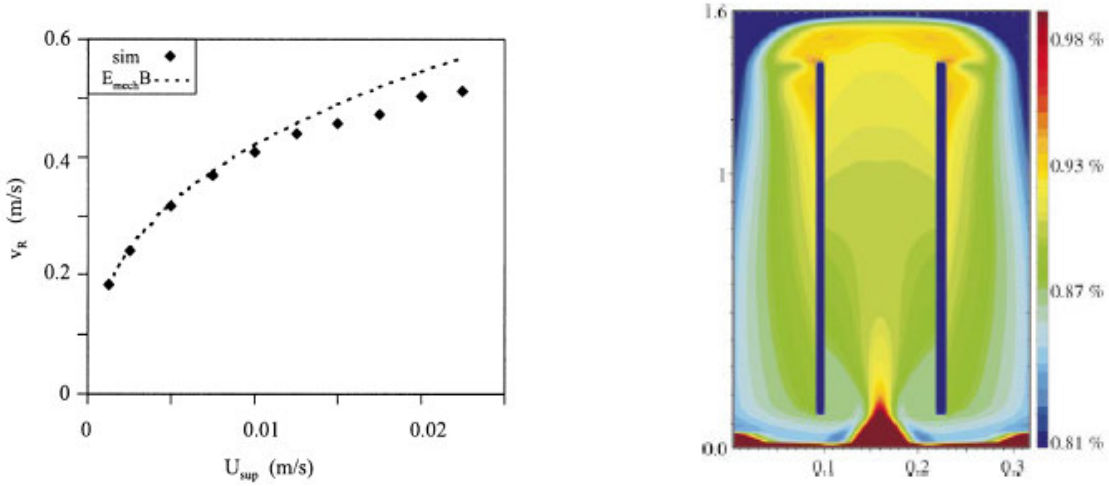

Figure 7.9: (a) - Comparison of CFD and 1D model, Oey et al., 2001, (b) - Solids distribution, Oey et al., 2001.

In the simulations, a steady state is reached with a fraction of the solids entrained in the circulating liquid. A large concentration is found close to the bottom wall. The turbulent

diffusion in the mass balance (the drifting velocity) plays an essential role: if this force is switch of, eventually all particles settle in the corners of the bottom region: no force is present to kick them out as without the effect of turbulence there no fluctuations lift the particles up again. It is concluded that the drifting velocity in the mass balance can mimic these effects.

7.3 Cyclones

Cyclones are used as separation devices. They produce a highly swirling flow that is used to separate components with different density present in a process stream. Applications involve the separation of solid particles from gas streams, separation of droplets from gas streams (demisting), and oil-water separation in so-called hydro-cyclones. Cyclones are low maintenance devices that (usually) do not have moving parts.

Single-phase swirling flows are a true challenge for numerical approaches. They show features very much different from flows without a significant swirl component:

They critically respond to changes in the outlet conditions. For instance, contracting the outlet geometry of a swirl tube with tangential inlet results in strongly increased swirl velocities and significant changes in the axial velocity profiles in the entire swirl tube, not only in the region close to the contraction (Escudier et al 1980).

They show strongly anisotropic turbulence. Strong swirl suppresses fluctuations in the radial direction up to a level where the flow tends to re-laminarisation.

Swirl flows in some cases show low-frequency instabilities; the core of the vortex then slowly precesses around an equilibrium position.

It is has been recognized that k-ε modelling is not capable of resolving the features of strongly swirling flows (Hoekstra et al 1999). The levels of the swirl velocity are too low, and the solid-body-part that is usually present in the tangential velocity profile gets too wide. Since in swirl flows the shape of the axial velocity profile is intimately connected to the axial evolution of the tangential velocity, also axial velocities get poorly predicted. Reynolds stress modelling is required to capture the average velocity field more or less accurately.

With a view to vortex precession, a time-resolved method is necessary to capture this phenomenon. From a practical point of view, capturing vortex precession may not be that essential: the time scales of the precessing motion are usually much larger than the relaxation times of the particles to be separated. From a point of view of experimental validation, capturing vortex precession is very relevant. Precession contributes significantly to (measured) root-mean-square (RMS) levels of velocity fluctuations. Comparing measured and simulated RMS profiles becomes virtually impossible when the former contain precession, and the latter do not. The importance of accurately capturing velocity fluctuation levels (due to turbulence) will be discussed later in this section.

The critical dependence of the entire flow field on the outflow conditions implies that outflow conditions need to be chosen with care. Convective conditions are preferred over zero-gradient conditions, and over pressure conditions (unless the outlet condition is chosen at such large distance that swirl has effectively died out at the outlet). The swirl flow's criticality also requires the geometry to be simulated completely. In Figure 7.10 we show deteriorated results for some axial velocity profiles if the dustbin underneath a reverse flow cyclone is not taken into account (to save computer effort) in the simulated flow domain (Derksen, 2003).

Now the multiphase aspects of cyclone simulations are discussed. Specifically gas cyclones are usually operated under relatively low loading conditions so that an Euler-Lagrange approach is very well feasible. Furthermore, one-way coupling approaches are often applied:

non-colliding point-particles that move under the influence of inertia, drag and gravity (due to the high density ratio other forces are of secondary relevance) are tracked through the Eulerian field. If the Eulerian field is the result of a RANS simulation, a random walk model needs to be used for dispersing the particles as a result of turbulence. Proper simulation of turbulent dispersion is crucial since the performance of gas cyclone operation expressed in grade efficiency curves (i.e. the fraction of collected particles as a function of particle size at specific cyclone operation conditions) is the result of an interplay between particles (or droplets for the matter) being driven towards the outer wall by centrifugal forces, and being dispersed by the action of turbulence.

In the context of a RANS-based simulation, turbulent particle dispersion is fully modelled by a random walk driven by (inevitably) simplifying concepts of the temporal and spatial behaviour of turbulence. In order to rely less on this relatively speculative modelling of particle dispersion, LES of cyclonic flow has been attempted (Slack et al 2000; Derksen & Van den Akker 2000). In an LES the grid-scale fluctuations are explicitly resolved. With sufficient resolution the fluid flow fluctuations that are felt by the particles are largely captured, and particle motion can be calculated realistically. An additional advantage of doing LES (being inherently three-dimensional and time dependent) is that vortex core precession is explicitly resolved, making a critical assessment of the numerical results with experimental data possible.

One-way coupled Euler-Lagrange simulations essentially assume zero mass-loading of the cyclone. Experimental work (Hoffmann et al 1991) has shown, however, that pressure drop and collection efficiency clearly are functions of mass-loading (with significant effects at mass-loading as low as 0.01). These effects can be mimicked by feeding back to the fluid the fluid-to-particle force, via e.g. a particle-source-in-cell (PSIC) approach. To reach practically relevant mass-loadings with relatively modest amounts of particles, the multiplication factors for the particle-to-fluid forces must be chosen large (typically 10^5 and up) which makes the physical realism of such an approach questionable.

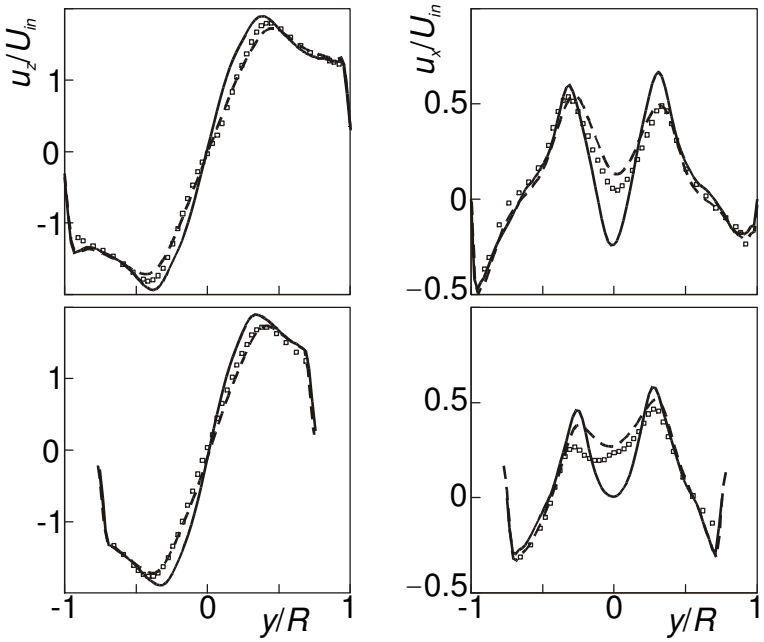

Figure 7.10: LES predictions of velocity profiles (left: tangential velocity; right: axial velocity) at two axial levels in a Stairmand cyclone (Derksen 2003). Symbols are (LDA) experimental data. Dashed lines are LES predictions with the full cyclone geometry. Drawn lines are LES predictions without taking into account the dustbin in the cyclone geometry.

So far mainly gas cyclones (containing drops and particles) have been discussed. In hydro-cyclones (typically used for oil-water separation) modelling attempts are scarcer, likely due to the complexity of the system. Not only are the loadings of the phases much higher, the way they are distributed (drops, layers) is a priori not known (even what the dispersed phase and what the continuous phase is may vary with location in the cyclone). This makes realistic simulations of hydro-cyclones operating under practical conditions a still open challenge.

7.4 Stirred tanks

Quite a few intricate modelling issues come together when considering the turbulent multi-phase flow in a stirred tank: a complex geometrical layout with partly static and partly moving boundaries, turbulence modelling of highly off-equilibrium turbulence, and interaction between the multiple phases.

Multiphase stirred tanks come in various flavours. Some basic operations are: solids suspension, gas dispersion, dispersing immiscible liquids, and blending miscible liquids (the latter hardly being multiphase). Typical examples of solids suspensions in mixing tanks are found in crystallization (where the solids phase is formed in a supersaturated liquor during the process), and in catalytic reactors where the catalyst is dispersed in the agitated liquid and stirring keeps it suspended and stimulates mass transfer. Gassed stirred tanks are extensively used in biological reactors. Bioreactors often also involve solid particles making the agitated system three-phase. In suspension polymerization the starting point is a dispersion of immiscible liquids that is agitated to form drops that during the process are transformed into polymer (solid) particles.

Commercial CFD vendors have strongly invested in serving the needs of mixing simulations. With respect to impeller modelling they offer sliding mesh (SM) capabilities where the flow domain is divided in a static part containing the static boundaries, and a rotating part containing the revolving impeller. At the interface between the two domains the continuity and momentum equations are communicated thereby taking into account the additional terms that are contained in the rotating reference frame. In principle the choice of the size and location of the two domains should not matter for the result of the simulation. In practice it does. This sensitivity and its extent should be checked.

In order to reduce computational cost, steady-state approaches have been proposed. In the multiple reference frame (MRF) approach, a steady-state solution is sought for both the flow in the static domain, and the rotating domain. The “art” of the method lies in the coupling between the rotating and static domain. Since they rotate with respect to one another, no circumferential flow gradients are allowed on the interface between the two domains. As a result, the interface needs to be “far away” from the impeller (there usually are strong circumferential gradients close to the impeller due to a discrete number of blades), and from the tank wall (that usually contains baffles to prevent rotation of the tank content as a whole and therefore also has circumferential gradients). For stirred tank layouts with a strong interaction of the impeller and the (baffled or otherwise structured) outer wall MRF-type approaches are therefore less suitable.

The turbulent flow in mixing tanks is of a swirling nature, although usually baffles are placed at the perimeter of the tank to prevent solid-body-like rotation of the fluid, and to enhance mixing. Consequently, Reynolds stress modelling is to be preferred over k-ε modelling. Also large-eddy simulations (LES) of the flow in mixing tank have been performed.

RANS-based approaches (either based on SM or MRF treatment of the impeller) are able to quite accurately capture the time-averaged flow in the tank. Usually, however, they significantly under-predict the turbulence levels (in terms of the turbulent kinetic energy). In

this respect, LES does a much better job (Yeoh et al 2005, Hartmann et al 2004). Since dispersion is one of the key issues in mixing tank flows, and turbulence is largely responsible for dispersion, good predictions of the turbulence levels are essential for realistic modelling of processes in mixing tanks.

Industrial multiphase systems usually have high dispersed phase hold-up's. In this respect the Euler-Euler approach seems the obvious choice. This choice, however, needs closer inspection in the light of other complicating factors present in stirred tank flow. The disperse phase usually has a broad size distribution due to the inhomogeneous turbulence in the tank. This very much complicates an Euler-Euler approach since in principle it requires the solution of the three-dimensional momentum equations for every size class separately making it very expensive. LES would be highly desirable with a view of better capturing turbulence levels. Euler-Euler LES, however, are not widely available (in commercial software) and form a research field in themselves. Euler-Lagrange approaches can deal fairly easily with the aspect of a size distribution and are well connected to LES (see section 4.? of this guide). They are limited, however, to dilute systems.

From the above the impression may arise that turbulent, multiphase flow simulations in mixing tanks are beyond the reach of present day numerical methods. In a general sense this is true. For specific cases, for specific aspects, and for answering specific questions simulations of these complex systems have shown useful in process design and scale-up, and have successfully been able to represent accurately experimentally observed phenomena.

7.5 Fluidized bed

This section describes numerical simulations of fluidized systems. The predictions of CFD simulations of bubbling fluidized beds, slugging fluidized beds, and bubble injection into fluidized beds incorporating various models are compared to the ``benchmark'' experimental data of Hilligardt and Werther (1986), Kehoe and Davidson (1971), Darton *et al.* (1977), and Kuipers (1990).

7.5.1 Drag force

Generally, when modelling the momentum transfer between the gas and the particles, the form and skin drag on the particles are combined in one force, the inter-phase drag force. This drag force is typically obtained from pressure drop measurements in fixed, fluidized and settling beds. Although there is a large number of drag force models described in the literature, the most applicable one is the Wen and Yu (1966). Contrary to what many researchers claim, this drag force expression incorporates experimental data over the whole range of solids volume fractions. The drag force is given by

$$\beta = \frac{3}{4} C_D \frac{(1-\alpha_s)\alpha_s \rho_g |\vec{v}_g - \vec{v}_s|}{d_s} (1-\alpha_s)^{-2.65}, \qquad (199)$$

where r_f is the fluid density, v_f and v_p are the gas and particles velocities. α_s is the volume fraction of the particulate phase. The drag coefficient C_d is given by

$$C_D = \begin{cases} \frac{24}{\mathrm{Re}_p (1-\alpha_s)} \left[1 + 0.15((1-\alpha_s)\mathrm{Re}_p)^{0.687} \right] & if \quad (1-\alpha_s)\mathrm{Re}_p < 1000 \\ 0.44 & if \quad (1-\alpha_s)\mathrm{Re}_p \geq 1000. \end{cases} \qquad (200)$$

And the particle Reynolds number is defined as

$$\mathrm{Re}_p = \frac{d_s \rho_g \mid v_g - v_s \mid}{\mu_g}, \qquad (201)$$

where d_s represents the mean diameter of particles. This form of the drag force model will represent the hydrodynamic forces on the particles. It is noted by Wen and Yu (1966) that this model is valid to predict the drag force on fine particles as well.

7.5.2 Kinetic theory of granular flow

The kinetic theory of granular flow is a model to account for the particulate stresses at low and moderate particle solid volume fractions. It has been shown that this approach, in conjunction with a frictional stress model, works well for fluidized bed modelling. Equivalent to the thermodynamic temperature for gases, the granular temperature can be introduced as a measure for the energy of the fluctuating velocity of the particles. The granular temperature is defined as

$$\theta_s = \frac{1}{3} < v_s'^2 >, \qquad (202)$$

where θ_s is the granular temperature, and $\mathbf{v}'$ is the solids fluctuating velocity. The equation of conservation of the solids fluctuating energy can be found in Ding and Gidaspow (1990) :

$$\frac{3}{2}\left[\frac{\partial}{\partial t}\left(\alpha_s \rho_s \theta\right) + \nabla \cdot \left(\alpha_s \rho_s \theta \vec{v}\right)\right] = \left(-\nabla P_s \bar{\bar{I}} + \bar{\bar{\tau}}_s\right) : \nabla \vec{v}_s - \nabla \cdot \left(\kappa_s \nabla \theta\right) - \gamma_s, \qquad (203)$$

where κ_s is the diffusion coefficient, γ_s is the dissipation of fluctuating energy. The dissipation of fluctuating energy is described by Jenkins and Savage (1983):

$$\gamma_s = 3(1-e^2)\alpha_s^2 \rho_s g_0 \theta \left(\frac{4}{d_s}\sqrt{\frac{\theta}{\pi_s}} - \nabla \cdot \vec{v}\right), \qquad (204)$$

where g_0 is the radial distribution function, e is the coefficient of restitution of colliding particles, as a measure for the non-idealness of the particle-collision, and d_s is the particle diameter. The radial distribution function corrects for the chaos assumption which fails at higher solids volume fraction and is typically given by

$$g_0 = \left[1 - \left(\frac{\alpha_s}{\alpha_{s,\max}}\right)^{\frac{1}{3}}\right]^{-1}. \qquad (205)$$

The solids pressure represents the solids phase normal forces due to particle-particle interactions. Its description based on the kinetic theory of granular flow was developed by Jenkins and Savage (1983) and Lun *et al.* (1984). In this approach both the kinetic and the collision influences are taken into account. The kinetic part describes the influence of particle translations, whereas the collision term accounts for the momentum transfer by direct collisions. The solids pressure is derived by Lun *et al.* (1984):

$$P_s = \alpha_s \rho_s \theta \left[1 + 2(1+e) g_0 \alpha_s\right]. \qquad (206)$$

The bulk viscosity is a measure for the resistance of a fluid against compression. It is obvious that the importance of the bulk viscosity depends strongly on the velocity gradients. In a fluidized bed, the bulk viscosity and the shear viscosity are in the same order of magnitude, and thus the bulk viscosity should not be neglected, as is done in simulating Newtonian fluids. The equation of Lun *et al.* (1984) is

$$\lambda_s = \frac{4}{3} \alpha_s^2 \rho_s d_s g_0 (1+e) \sqrt{\frac{\theta}{\pi}}, \qquad (207)$$

where l_s is the bulk viscosity of the solids phase.

Whereas pressure and bulk viscosity describe normal forces, the shear viscosity accounts for the tangential forces. It was shown by Lun et al. (1984) that it is possible to combine different inter-particle forces and to use a momentum balance similar to that of a true continuous fluid. Similar to the solids pressure, a solids phase viscosity can be derived from the kinetic theory. The shear viscosity is built up out of two terms: one term for the dilute region and one term for the dense region. In literature different expressions for the solids shear viscosity can be found. The work of Gidaspow *et al.* (1982) is validated by comparison with measured data:

$$\mu_s = \frac{4}{5} \alpha_s^2 \rho_s d_s g_0 (1+e) \sqrt{\frac{\theta}{\pi}} + \frac{2 \frac{5\sqrt{\pi}}{96} \rho_s d_s \sqrt{\theta}}{(1+e) g_0} \left[1 + \frac{4}{5} g_0 \alpha_s (1+e)\right]^2, \qquad (208)$$

where m_s is the shear viscosity of the solids phase.

7.5.3 Frictional stress

At high solid volume fraction, sustained contacts between particles occur, and the stresses predicted by kinetic theory of granular flow are insufficient. Hence, the additional frictional stresses must be accounted for in the description of the solid-phase stress. Zhang and Rauenzahn (1997) conclude that particle collisions are no longer instantaneous at high solid volume fractions, as is assumed in kinetic theory. Several approaches have been presented in the literature to model the frictional stress, mostly originated from geological research groups. Typically, the frictional stress is written in a Newtonian form and has a deviatoric stress-like contribution, and a normal stress-like contribution. The frictional stress is added to the stress predicted by kinetic theory for $\alpha_s > \alpha_{s,\min}$, where the subscript *min* stands for threshold value,

$$\begin{aligned} p_s &= p_{kinetic} + p_{frictional} \\ \mu_s &= \mu_{kinetic} + \mu_{frictional}. \end{aligned} \qquad (209)$$

Johnson and Jackson (1987) propose a semi-empirical equation for the normal frictional stress,

$$p_{frictional} = Fr \frac{(\alpha_s - \alpha_{s,\min})^{nn}}{(\alpha_{s,\max} - \alpha_s)^{pp}}, \qquad (210)$$

where *Fr, nn*, and *pp* are empirical material constants, and $\alpha_s > \alpha_{s,\min}$, $\alpha_{s,\min}$ being the solid volume fraction when frictional stresses become important. The frictional shear viscosity is then related to the frictional normal stress by the linear law proposed by Coulomb (1776or the

approach proposed by Schaeffer (1987),

$$\mu_{frictoin} = \frac{P_{friction}\sin(\phi)}{\alpha_s\sqrt{\left(\left(\frac{\partial u}{\partial x}-\frac{\partial v}{\partial y}\right)^2+\left(\frac{\partial u}{\partial x}\right)^2+\left(\frac{\partial v}{\partial y}\right)^2+\frac{1}{4}\left(\frac{\partial u}{\partial y}-\frac{\partial v}{\partial x}\right)^2\right)}}, \qquad (211)$$

where ϕ is the angle of internal friction. Values of $\alpha_{s,min}$ are typically in the range *0.55-0.6*. Values for the empirical parameters are dependent of the material properties; some examples are given in Table 7.1.

Table 7.1: Values for the empirical parameters for the frictional model, as suggested by various researchers.

Fr (N/m^2)	nn	pp	$\alpha_{s,min}$	ϕ	d_s (μm)	ρ_s (kg/m^3)	Material	Reference
0.05	2	3	0.5	28	150	2500	Not specified	Ocone et al. (1993)
$3.65\ 10^{-32}$	0	40	-	25	1800	2980	Glass	Johnson and Jackson (1987)
$4.0\ 10^{-32}$	0	40	-	25	1000	1095	Polystyrene	Johnson and Jackson (1987)
0.05	2	5	0.5	28.5	1000	2900	Glass	Johnson et al. (1990)

The test cases described in this paragraph are a freely bubbling fluidized bed, a slugging fluidized bed, and a single bubble injection into a fluidized bed.

The particles in a fluidized bed move due to the action of the fluid through the drag force, and bubbles and complex solids mixing patterns result. Typically, the average solid volume fraction in the bed is fairly large, averaging about 40 percent, whereas in the free-board of the fluidized bed (the top) there are almost no particles.

7.5.4 Simulation set-up

Numerics

Models for the Eulerian-Eulerian governing equations including kinetic theory of granular flow and frictional stresses are available in a number of commercial CFD packages. Some of these packages employ a segregated algorithm, and some employ a partially or fully coupled algorithm. The governing equations are discussed in section 4.4.

Compressibility can be an important effect in fluidized beds, as the pressure drop over the solids phase can increase the density of the gas phase severely. Although a weak-compressible algorithm should suffice for these types of calculations, this is not available in every flow solver.

For dilute flows it can be difficult or impossible to find a grid-independent solution, for dense gas-solid flows this seems not to be a major problem. In fluidized beds, a typical grid spacing of around 1-2 cm in each direction seems to work well.

To ensure correct predictions of average properties, the time-series generated by the simulations should be at least 40 seconds long, and the first 10-20 seconds of this time-series should not be taken into account when determining the average. Unfortunately, for typically sized systems, this leads to enormous computational effort.

Although not often discussed, the air-inlet system of the fluidized bed can have a significant effect on the fluidization behaviour. If this is expected to be the case, there are models which account for this (Johansson 2004, Sasic 2005).

Most simulations of fluidized beds are carried out in two dimensions, although a difference in behaviour has been seen in these two approaches. However, due to the computational effort many types of systems cannot be modelled in three dimensions and a smart choice of two or semi-two dimensions has to be made.

Boundary and initial conditions

The walls of the fluidized bed are treated as no-slip velocity boundary conditions for the fluid phase, and free- or partial-slip velocity boundary conditions are employed for the particle phase. For the granular temperature at a wall, a zero gradient can be assumed, but more complex boundary conditions describing the process of moving particles with the wall and its roughness exist as well (Johnson and Jackson, 1987 or Jenkins, 1992).

The boundary condition at the top of the free-board (fluid phase outlet) is a so-called pressure boundary. The pressure at this boundary is fixed to a reference value, the outlet pressure of the system. Neumann boundary conditions are applied to the gas flow, requiring a fully-developed gas flow. For this, the free-board of the fluidized bed needs to be of sufficient height; this is validated through the simulations. In the free-board, the solid volume fraction is very close to zero and this can lead to unrealistic values for the particle velocity field and poor convergence. For this reason, a solid volume fraction of 10^{-6} is set at the top of the free-board. This way the whole free-board is seeded with a very small number of particles, which gives more realistic results for the particle phase velocity in the free-board, but does not influence the behaviour of the fluidized bed itself.

The bottom of the fluidized bed is made impenetrable for the solid phase by setting the solid-phase axial velocity to zero. For the freely bubbling fluidized bed and the slugging fluidized bed, Dirichlet boundary conditions are employed at the bottom with a uniform gas inlet velocity. To break the symmetry in the case of the bubbling and slugging beds, initially a small jet of gas is specified at the bottom left hand side of the geometry. In the case of the bubble injection, a Dirichlet boundary condition is employed at the bottom of the fluidized bed. The gas inlet velocity is kept at the minimum fluidization velocity, except for a small orifice in the centre of the bed, at which a high inlet velocity is specified. Finally, the solids-phase stresses, as well as the granular temperature, at the top of the fluidized bed are set to zero.

Initially, the bottom part of the fluidized bed is filled with particles at rest with a uniform solid volume fraction. The gas flow in the bed is set to its minimum fluidization velocity. In the freeboard a solid volume fraction of 10^{-6} is set, as explained above. The granular temperature is initially set to 10^{-10} m^2 s^{-2}.

7.5.5 Various test cases and results

With increasing gas velocity above the minimum fluidization velocity, U_{mf}, bubbles are formed as a result of the inherent instability of the gas-solid system. The behaviour of the bubbles significantly affects the flow phenomena in the fluidized bed, e.g. solids mixing, entrainment, and heat and mass transfer. The test cases in this comparative study are used to investigate the capabilities of the closure models and governing equations to predict fluidization behaviour, e.g. bubble behaviour and bed expansion. Simulation results of each test case are compared to generally accepted experimental data and (semi) empirical models. The system properties and computational parameters for each of the test cases are given in Table 7.2.

Table 7.2. System properties and computational parameters.

Parameter	Description	Freely bubbling fluidized bed	Slugging fluidized bed	Bubble injection into fluidized bed
$\rho_s\ (kg/m^3)$	Solid density	2640	2640	2660
$\rho_g\ (kg/m^3)$	Gas density	1.28	1.28	1.28
$\mu_g\ (Pa\ s)$	Gas viscosity	$1.7\ 10^{-5}$	$1.7\ 10^{-5}$	$1.7\ 10^{-5}$
$d_s\ (\mu m)$	Particle diameter	480	480	500
$e(-)$	Coefficient of restitution	0.9	0.9	0.9
$\alpha_{max\ (-)}$	Max. solid volume fraction	0.65	0.65	0.65
$U_{mf}\ (m/s)$	Min fluidization velocity	0.21	0.21	0.25
$D\ (m)$	Inner column diameter	0.5	0.1	0.57
$H\ (m)$	Column height	1.3	1.3	0.75
$H_{mf}\ (m)$	Height at minimum fluidization	0.97	0.97	0.5
$\alpha_{s,mf}\ (-)$	Solids volume fraction at minimum fluidization	0.42	0.42	0.40
$\Delta x\ (mm)$	X grid spacing	7.1	6.7	7.5
$\Delta y\ (mm)$	Y grid spacing	7.6	7.4	12.5

Slugging fluidized beds

In the case of the slugging fluidized beds, coalescing bubbles eventually reach a diameter of 70% or more of the column diameter, resulting from either a large inlet gas velocity or a narrow bed. The operating conditions employed in the simulations correspond to the conditions reported by Kehoe and Davidson (1971), who present a detailed study of slug flow in fluidized beds. The experiments of Kehoe and Davidson (1971) were performed in slugging fluidized beds of 2.5, 5, and 10 cm diameter columns using Geldart B particles from 50 to 300 μm diameter and with superficial gas inlet velocities up to 0.5 m $^{s-1}$ X-ray photography was used to determine the rise velocity of slugs and to determine the bed expansion. Kehoe and Davidson (1971) use their data to validate two different equations for the slug rise velocity, both based on two-phase theory,

$$u_{slug} = U - U_{mf} + \frac{\varphi}{2}\sqrt{gD_T}, \qquad (212)$$

$$u_{slug} = U - U_{mf} + \frac{\varphi}{2}\sqrt{2gD_T}, \qquad (213)$$

where φ is the analytically determined square root of the Froude number of a single rising bubble. The first of these equations is the exact two-phase theory solution, whereas the second is a modification based on the following observations:

1. For fine particles (< 70 μm) the slugs travel symmetrically up in the fluidized bed, so the slug rise velocity is increased by coalescence.

2. For coarser particles (> 70 μm) the slugs tend to move up along the walls, which also increase their velocity.

According to Kehoe and Davidson (1971), these two equations give upper and lower bounds on the slug rise velocity. Furthermore, Kehoe and Davidson (1971) measured the maximum bed expansion, H_{max}, during slug flow. They validated their theoretical analysis which led to the result that

$$\frac{H_{\max} - H_{mf}}{H_{mf}} = \frac{U - U_{mf}}{u_{bub}} \qquad (214)$$

where u_{bub} is the rise velocity of a slug without excess velocity.

In some kinetic theory models, a correlation between the gas phase and particle phase velocity fluctuations, called J_s, is taken into account; this is, however, not an important contribution in dense gas-solid flows. Figure 7.11 shows the predicted maximum bed expansion with increasing gas velocity during the slug flow and the two correlations of Kehoe and Davidson (1971). Figure 7.12 shows the increasing slug rise velocity with increasing gas velocity. The CFD models do a good job at predicting engineering quantities, like bed expansion and bubble sizes.

Bubbling fluidized bed

In the freely bubbling fluidized bed case, the gas flow is distributed across the inlet of the bed. Small bubbles form at the bottom of the fluidized bed which rise, coalesce, and erupt as large bubbles at the bed surface. Hilligardt and Werther (1986) have done many measurements of bubble size and bubble velocity under various conditions using the probe developed by Werther and Molerus (1973) and have correlated their data in the form of the Davidson and Harrison (1963) bubble model. Hilligardt and Werther propose a variant of the Davidson and Harrison (1963) model for predicting the bubble rise velocity as a function of the bubble diameter,

$$u_b = \psi(U - U_{mf}) = \phi\nu\sqrt{g d_b} \qquad (215)$$

where φ is the analytically determined square root of the Froude number of a single rising bubble in an infinitely large homogeneous area. Pyle and Harrison (1967) have determined that φ = 0.48 for a two dimensional geometry, whereas in three dimensions the Davies-Taylor relationship gives φ = 0.71. The symbols ψ and ν, added by Hilligardt and Werther (1986), are empirical coefficients based on their data, which are dependent upon the type of particles and the width and height of the fluidized bed. For the particles and geometry employed in this study, Hilligardt and Werther (1986) propose ψ ~ 0.3 and ν ~ 0.8. Proposals of values for ψ and ν under various fluidization conditions, determined by simulations, are given by van Wachem *et al.* (1998). Figure 7.13(a) shows a snapshot of the solids volume fraction contours; the bubbling behaviour can clearly be observed.

Figure 7.13(b) shows the predicted bubble rise velocity employing different drag models in a freely bubbling fluidized bed, compared to the empirical correlation of Hilligardt and Werther (1986). All of the investigated drag models are in fairly good agreement with the empirical correlation.

Bubble injection

Single jets entering fluidized bed operated at the minimum fluidization velocity through a narrow single orifice provide details of bubble formation and growth. Such experiments were carried out by Kuipers (1990). Kuipers (1990) reported the shape of the injected bubble as well as the quantitative size and growth of the bubble with time using high-speed photography. The superficial gas inlet velocity from the orifice was u = 10 m s^{-1} and the orifice was d = 1.5 10^{-2} m wide.

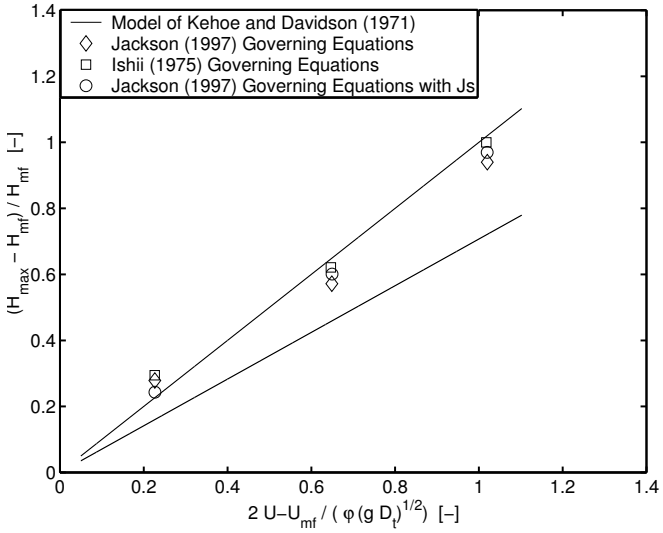

Figure 7.11. Predicted maximum bed expansion of a slugging fluidized bed with an increase in gas velocity. The computational predictions are compared to the two-phase theory as proposed and validated by Kehoe and Davidson (1971).

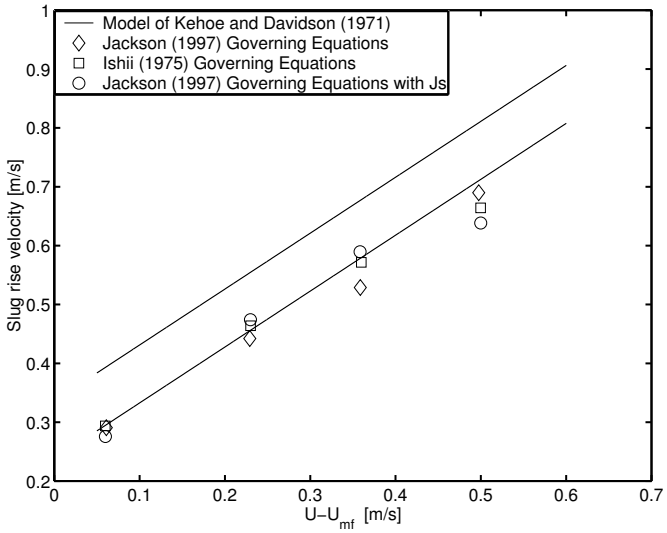

Figure 7.12. Predicted slug rise velocity with increasing gas velocity. The predictions are compared with the two-phase theory as proposed and validated by Kehoe and Davidson (1971).

Figure 7.13(a) shows the quantitative bubble size prediction for a single jet entering a fluidized bed operating at the minimum fluidization velocity on the drag models of Wen and Yu (1966) and Syamlal *et al.* (1993) which are compared to the experimental data of Kuipers (1990). Frictional stresses can increase the total solid-phase stress by orders of magnitude and is an important contributing force in dense gas-solid modelling, although the size of the bubble is not significantly influenced by the frictional stress, as shown in Figure 3. The Wen and Yu (1966) drag model yields better agreement with Kuipers' (1990) findings for both the

bubble

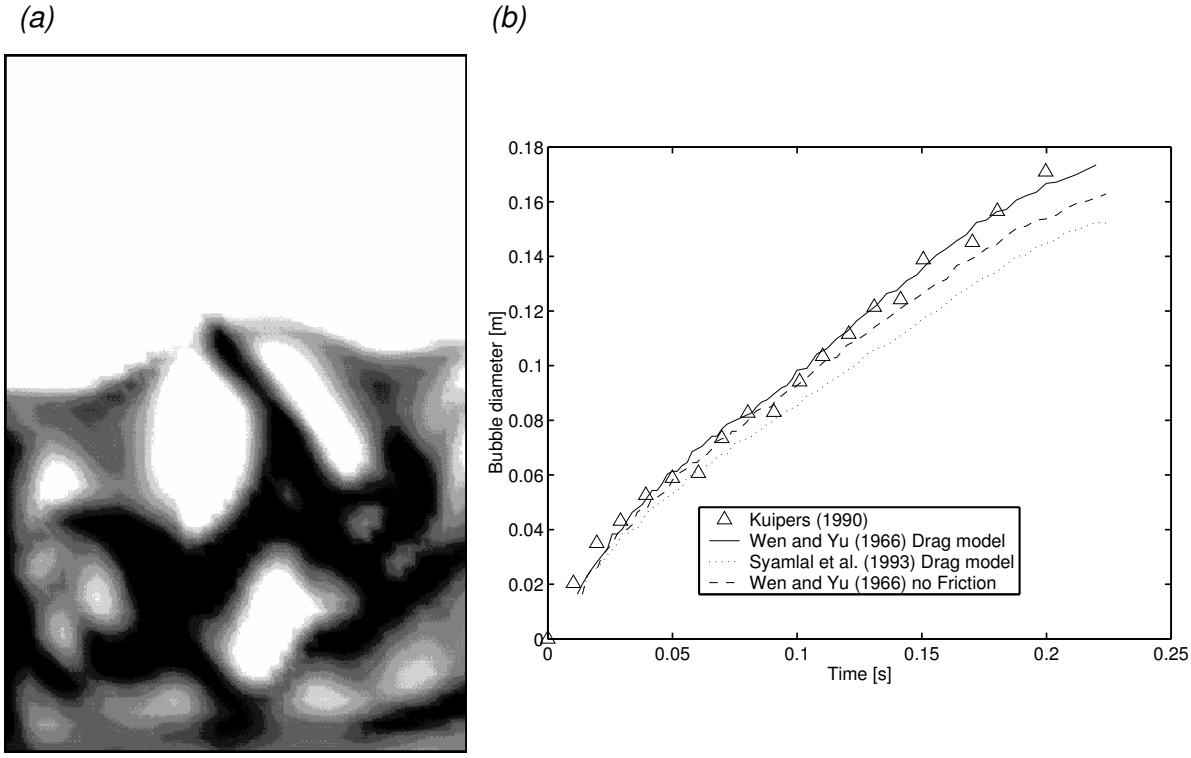

Figure 7.13: (a): A snapshot of the computation of the solids volume fraction profiles of a bubbling fluidized bed; (b): Predicted bubble rise velocity as a function of the bubble diameter at U=0.54 m/sec compared to the experimentally determined correlation of Hilligart and Werther (1986).

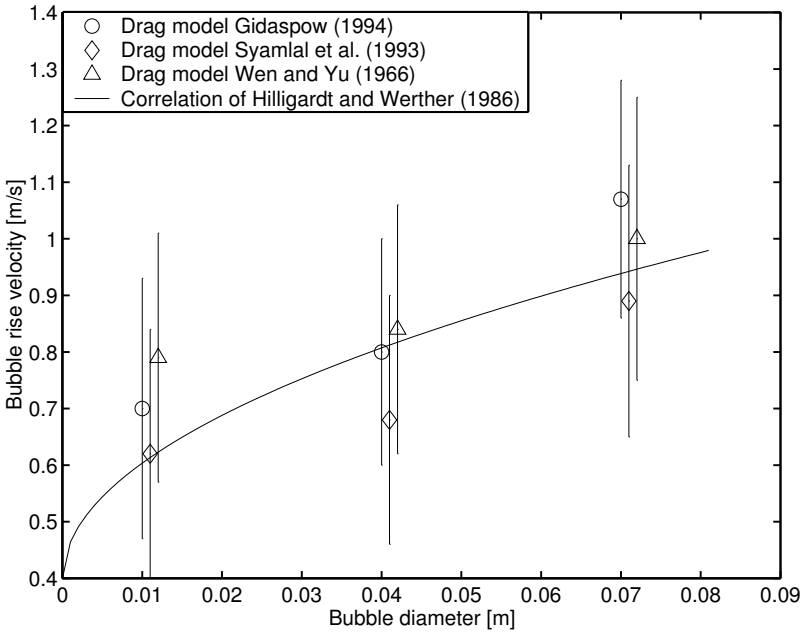

Figure 7.14: Bubble diameter as a function of time for a bubble formed at a single jet of U=10 m/sec. A comparison is made with simulations employing different drag models with the experimental work of Kuipers (1990).

shape and size than the Syamlal *et al.* (1993) drag model. The Syamlal *et al.* (1993) drag model under predicts the bubble size and produces a bubble that is more circular in shape than in the experiments of Kuipers (1990) and in the simulations with the Wen and Yu (1966) drag model.

8 Checklist of Best Practice Advice

- Start your simulation problem with a single-phase flow situation according to ERCOFTAC's Best Practice Guidelines for Industrial Computational Fluid Dynamics, making sure to minimize numerical errors due to solver, grid-size and time steps.
- Search the ERCOFTAC Dispersed Turbulent Two-Phase Flow data base for bench mark cases close to your application (access via http://www.ercoftac.org).
- Establish the requirements for the turbulence model. If dynamic effects are important or you have a strongly swirling flow condition select LES, otherwise RANS could be sufficient.
- Establish the forces acting on the bubbles, drops or particles that are important for your simulation.
- Determine whether you have to simulate a dilute or dense dispersion and select appropriate Euler-Lagrange (Particle Tracking) or Euler-Euler (Two-Fluid) methods.
- Make sure that for increasing particle loading the simulation method selected allows for turbulence modulation (two-way coupling) and particle-particle and particle-wall collisions. For tube geometries the effect of wall roughness on particle dispersion has to be incorporated.
- For the Euler-Euler approach a first try with the mixture model may give a fast guidance for more elaborate calculations.
- In an Euler-Lagrange approach sampling of the eddy lifetime at random from a Poisson distribution based on the integral time scale of turbulence, T_L is most realistic.
- Make sure that after a certain number of Eulerian iterations or after reaching a certain degree of convergence for the fluid flow, the particle tracking is performed again, since the flow field may have changed due to two-way coupling.
- If for your application the 3D distribution of the dispersed phase in your equipment is important select a Multi-Fluid model that enables you to work with a range of size classes that can be monitored separately. The behaviour of particles in a complex wall-bounded turbulent flow field is size dependent, so unwanted local accumulation of particles could be an issue.
- Start by performing the multiphase flow simulations with the selected particle force and turbulence models on geometries close to your target geometry for which validation data are available. This will enable you to assess the proper convergence conditions and it can provide you a guideline on the accuracy that you may expect from your simulations.
- For drop and spray modelling with heat and mass transfer ensure proper transfer of heat and mass with surrounding continuous phase is accounted for.
- Reduce your data such that it enables you to relate the distribution of the dispersed phase in the turbulent flow field as function of the process conditions to measurable design and operational performance data. This can help you to solve potential operational problems of your multiphase flow equipment.

9 Suggestions for future developments

- Since many industrial multiphase flow applications have a dynamic character there is a rising need to use LES as an engineering tool for the turbulence in complex geometries. To make it practically feasible the computing time should be reduced drastically either by more powerful computing facilities or by improved numerical solvers.
- Explore the option to also use LES in Euler/Euler (two-fluid) methods for turbulent dispersed multiphase flows
- Improve the empirical closure relations for the forces acting on bubbles, drops and particles by both improved measurements and DNS computations in the vicinity of particles moving in a turbulent flow field.
- Improve the wall functions used in turbulent dispersed flow calculations by incorporating the effects of the presence of particles.

10 References

Andrews IV, A.T., P.N. Loezos, and S. Sundaresan. 2005. Coarse-Grid Simulation of Gas-Particle Flows in Vertical Risers. & Engineering Chemistry Research 44, (16): 6022-6037.

Bauer, M. and Eigenberger, G., 1999, A concept for multi-phase modeling of bubble columns and loop reactors, *Chem. Eng. Sci.*, 54, 5109-5117.

Bauer, M. and Eigenberger, G., 2001, Multiscale modeling of hydrodynamics, mass transfer and reaction in bubble column reactors, *Chem. Eng. Sci.*, 56, 1067-1074.

Becker, S., Sokolichin, A., and Eigenberger, G., 1994, Gas-liquid flow in bubble columns and loop reactors: part II. Comparison of detailed experiments and flow simulations, *Chem. Eng. Sci.*, 49, 5747-5762.

Beetstra, R., M.A. van der Hoef, and J.A.M. Kuipers. 2006. Drag force from lattice Boltzmann simulations of intermediate Reynolds number flow past mono- and bidisperse arrays of spheres. Submitted to AIChE Journal.

Bel F'dhila, R. and Simonin, O., 1992, Eulerian predictions of a turbulent bubbly flow downstream a sudden pipe expansion, In Sommerfeld, M., ed., *Sixth Workshop on Two-Phase Flow Predictions*, Erlangen, Germany, 264.

Berlemont, A., Chang, Z., and Gouesbet, G. (1990) Lagrangian scheme for particle tracking in non-isotropic turbulence. Ercoftac Bulletin, 36:7.

Biesheuvel, A., and Van Wijngaarden, L., 1984, Two-phase flow equations for a dilute dispersion of gas bubbles in liquid, *J. Fluid Mech.*, 148, 301-318.

Bokkers, G.A. 2005. Multi-level Modeling of the Hydrodynamics in Gas Phase Polymerisation Reactors; PhD thesis University of Twente, Enschede.

Bussman, M., Mostaghimi, J. and Chandra, S. (1999). On a three-dimensional volume tracking model of droplet impact. Phys. Fluids, **11**, 1406-1417.

Campbell, C.S., and C.E. Brennen. 1985. Computer simulations of granular shear flows. Journal of Fluid Mechanics 151: 167-188.

Chang, Y.C., Hou, T.Y., Merriman, B. and Osher, S. (1996). A level set formulation of Eulerian interface capturing methods for incompressible fluid flows, J. Comp. Phys., **124**, 449-464.

Chen, C. and L. -S Fan. (2004). Discrete simulation of gas-liquid bubble columns and gas-liquid-solid fluidized beds. *AIChE Journal 50, (2): 288-301*

Chen, P., Dudukovic, M.P. and Sanyal, J., 2005, Three-dimensional simulation of bubble column flows with bubble coalescence and break up, *AIChE J.*, 51, 696-712.

Clift, R., Grace, J.R. and Weber, M. (1978), Bubbles, Drops and Particles, Academic Press, New York.

Cockx, A., , Do-Quang, Z., Liné, A., and Roustan, M., 1999, Use of computational fluid dynamics for simulating hydrodynamics and mass transfer in industrial ozonization towers, *Chem. Eng. Sci.*, 54, 5085-5090.

Cockx, A., Liné, A., Roustan, M., Do-Quang, Z. and Lazarova, V., 1997, Numerical simulation and physical modeling of the hydrodynamics in an air-lift internal loop reactor, *Chem. Eng. Sci.*, 52, 3787-3793.

Crowe, C., Sommerfeld, M., and Tsuji, A. (1998) Multiphase flows with droplets and particles, CRC Press, Boca Raton.

Crowe, C.T., Troutt, T.R., and Chung, J.N. (1996) Numerical models for two-phase turbulent flows. Ann. Rev. Fluid Mech. 28: 11.

Cundall P.A., and O.D.L. Strack, 1979. A discrete numerical model for granular assemblies. Geotechnique, 29, (1): 47-65.

Darmana, D., N.G. Deen and J.A.M. Kuipers. 2005. Detailed Modeling of Hydrodynamics, Mass transfer and Chemical Reactions in a Bubble Column using a Discrete Bubble Model. Chemical Engineering Science 60, (12): 3383-3404.

Darton, R. C., R. D. Lanauze, J. F. Davidson, and D. Harrison, 1977, Bubble-growth due to coalescence in fluidized-beds. Transactions of the Institution of Chemical Engineers, 55, 274-280.

Delnoij, E., F.A. Lammers, J.A.M. Kuipers and W.P.M. van Swaaij. 1997a. Dynamic simulation of dispersed gas-liquid two-phase flow using a discrete bubble model, Chemical Engineering Science 52, (9): 1429-1458.

Delnoij, E., J.A.M. Kuipers and W.P.M. van Swaaij. 1997c. Dynamic simulation of gas-liquid two-phase flow: effect of column aspect ratio on the flow structure, Chemical Engineering Science 52, (21-22): 3759-3772.

Delnoij, E., J.A.M. Kuipers and W.P.M. van Swaaij. 1999. A three-dimensional CFD model for gas-liquid bubble columns, Chemical Engineering Science 54, 2217-2226.

Delnoij, E., J.A.M.Kuipers and W.P.M. van Swaaij. 1997b. Computational fluid dynamics applied to gas-liquid contactors, Chemical Engineering Science 52, (21-22): 3623-3638.

Derksen, J.J. (2003) Separation performance predictions of a Stairmand high-efficiency cyclone. AIChE J., 49: 1359.

Derksen, J.J., and Van den Akker, H.E.A. (2000) Simulation of vortex core precession in a reverse-flow cyclone. AIChE J., 46: 1317.

Ding, J., & Gidaspow, D. (1990). A Bubbling Fluidization Model Using Kinetic-Theory of Granular Flow. Aiche Journal, 36(4), 523-538

Drew, D.A., 1983, Mathematical modeling of two-phase flow, *Ann. Rev. Fluid Mech.*, 15, 261-291.

Elgobashi, S. (1994) On predicting particle-laden turbulent flows. Appl. Sci. Res., 52: 309.

Elgobashi, S.E., and Truesdell, G.C. (1993) On the two-way interaction between homogeneous turbulence and dispersed solid particles I: Turbulence modification, Physics of Fluids, 5: 1790.

Ergun S., 1952. Fluid Flow through Packed Columns. Chemical Engineering Progress 48, 89-94.

Escudier, M.P., Bornstein, J., and Zehnder, N. (1980) Observations and LDA measurements of confined turbulent vortex flow. J. Fluid Mech., 98: 49.

Esmaeeli, A. and Tryggvason, G. (1998a), Direct numerical simulation of bubble flows. Part I. Low Reynolds number arrays, J. Fluid Mech., **377**, 313-345.

Fedkiw, R. and Osher, S. (2001). Level-set methods: An overview and some recent results, J. Comp. Phys., **169**, 463.

Fu, J., M.J. Adams, G.K. Reynolds, A.D. Salman, and M.J. Hounslow. 2004. Impact deformation and rebound of wet granules. Powder Technology 140, (3): 248-257.

Goldschmidt M.J.V., J.A.M. Kuipers, and W.P.M. van Swaaij. 2001. Hydrodynamic modeling of dense gas-fluidised beds using the kinetic theory of granular flow: effect of coefficient of restitution on bed dynamics. Chemical Engineering Science 56, (2): 571-578.

Goldschmidt, M.J.V., R. Beetstra, and J.A.M. Kuipers. 2002. Hydrodynamic modelling of dense gas-fluidised beds: Comparison of the kinetic theory of granular flow with 3D hard-sphere discrete particle simulations. Chemical Engineering Science 57, (11): 2059-2075.

Gore, R.A., and Crowe, C.T. (1989) Effect of particle size on modulating turbulence intensity. Int. J. Multiphase Flow, 15: 279.

Gosman, A.D., Issa, R.I., Lekakou, C., Looney, M.K. and Politis, S., 1992, Multidimensional modeling of turbulent two-phase flows in stirred vessels, *AIChE J.*, 38, 1946.

Hartmann, H., Derksen, J.J., Montavon, C., Pearson, J., Hamill, I.S., and Van den Akker, H.E.A. (2004) Assessment of large eddy and RANS stirred tank simulations by means of LDA. Chem. Eng. Sc., 59: 2419.

Haworth, D.C., and Pope, S.B. (1987) A generalized Langevin model for turbulent flows. Phys. Fluids, 30: 1026.

He, Y., M. van Sint Annaland, N.G. Deen, and J.A.M. Kuipers. 2006. Gas-solid two-phase turbulent flow in a circulating fluidized bed riser: an experimental and numerical study, Proceedings of the 5th World Congress on Particle Technology, April 23-27, 2006, Orlando, Florida, USA.

Helland, E., R. Occelli and L. Tadrist. 1999. Numerical study of cohesive powders in a dense fluidized bed. Comptes Rendus de l'Academie de Sciences - Serie IIb: Mecanique, Physique, Chimie, Astronomie 327, (14): 1397-1403.

Helland, E., R. Occelli and L. Tadrist. 2000. Numerical study of cluster formation in a gas-particle circulating fluidized bed. Powder Technology 110, (3): 210-221.

Helland, E., R. Occelli and L. Tadrist. 2002. Computational study of fluctuating motions and cluster structures in gas-particle flows. International Journal of Multiphase Flow 28, (2): 199-223.

Helland, E., R. Occelli, and L. Tadrist. 2005. Numerical study of cluster and particle rebound effects in a circulating fluidised bed. Chemical Engineering Science 60, (1): 27-40.

Hill, R.J., D.L. Koch and J.C. Ladd. 2001. Moderate-Reynolds-numbers flows in ordered and random arrays of spheres. Journal of Fluid Mechanics 448: 243-278.

Hilligardt, K. and J. Werther, 1986, Local bubble gas hold-up and expansion of gas/solid fluidized beds. German Chemical Engineering, 9, 215-221.

Hirt, C.W. and Nichols, B.D. (1981). Volume of Fluid (VOF) method for the dynamics of free boundaries, *J. Comp. Phys.* **39**, 201.

Hoekstra, A.J., Derksen, J.J., and Van den Akker, H.E.A. (1999) An experimental and numerical study of turbulent swirling flow in gas cyclones. Chem. Eng. Sc., 54: 2055.

Hoffmann, A.C., Arends, H., and Sie, H. (1991) An experimental investigation elucidating the nature of the effect of solids loading on cyclone performance, Filtration & Separation, 28: 188.

Hoomans, B.P.B., J.A.M. Kuipers, W.J. Briels, and W.P.M. Van Swaaij. 1996. Discrete particle simulation of bubble and slug formation in a two-dimensional gas-fluidised bed: A hard-sphere approach. Chemical Engineering Science 51, (1): 99-118.

Ibsen, C.H. 2002. An Experimental and Computational Study of Gas-Particle Flow in Circulating Fluidised Reactors. PhD thesis , Aalborg University Esbjerg, Denmark.

Ida, M. (2000). An improved unified solver for compressible and incompressible fluids involving free surfaces. Part I. Convection, Computer Physics Communications **132**, 44-65.

Ishii, M., 1975, Thermo-fluid dynamic theory of two-phase flow, Eyrolles, Paris.

Iwadate, M., and M. Horio. 1998. Agglomerating fluidization of wet powders and group C powders: a numerical analysis. In: L.S. Fan, and T. Knowlton Eds., Fluidization IX, Engineering Foundation, Durango, USA. p.293.

Johansson, K. (2004). Fluid Dynamics and Erosion in a Fluidized Bed for Energy Production - A Numerical and Experimental Study, PhD Thesis, Chalmers University of Technology.

Johnson, P. C., & Jackson, R. (1987). Frictional Collisional Constitutive Relations for Antigranulocytes-Materials, with Application to Plane Shearing. Journal of Fluid Mechanics, 176, 67-93.

Kafui, K.D., C. Thornton, and M.J. Adams. 2002. Discrete particle-continuum fluid modelling of gas-solid fluidised beds. Chemical Engineering Science 57, (13): 2395-2410.

Kawaguchi, T., T. Tanaka and Y. Tsuji. 1998. Numerical simulation of two-dimensional fluidized beds using the discrete element method (comparison between the two- and three-dimensional models), Powder Technology 96, (2): 129-138.

Kehoe, P.W.K. and Davidson, J.F. (1971). Continuously slugging fluidised beds. Inst. Chem. Eng. Symp. Ser., 33, 97-116

Kuipers, J.A. (1990). A Two-Fluid Micro Balance Model of Fluidized Beds. PhD Thesis, University of Twente, The Netherlands.

Kuwagi, K., T. Mikami, and M. Horio. 2000. Numerical simulation of metallic solid bridging particles in a fluidized bed at high temperature. Powder Technology 109, (1-3): 27-40.

Ladd, A.J.C. (1994) Numerical simulations of particle suspensions via a discretized Boltzmann equation. Part I: Theoretical Foundation. J. Fluid Mech. 271: 285.

Ladd, A.J.C. (1994a). Numerical simulations of particulate suspensions via a discretised Boltzmann equation. Part 1. Theoretical Foundation, J. Fluid Mech., **271**, 285-309.

Ladd, A.J.C. (1994b). Numerical simulations of particulate suspensions via a discretised Boltzmann equation. Part 2. Numerical Results, J. Fluid Mech., **271**, 311-339.

Langston, P.A., U. Tüzün and D.M. Heyes. 1994. Continuous potential discrete particle simulations of stress and velocity fields in hoppers transition from fluid to granular flow, Chemical Engineering Science 49, (8): 1259-1275.

Li, J., and J.A.M. Kuipers. 2002. Effect of pressure on gas-solid flow behavior in dense gas-fluidized beds: A discrete particle simulation study. Powder Technology 127, (2): 173-184.

Li, J., and J.A.M. Kuipers. 2003. Gas-particle interactions in dense gas-fluidized beds. Chemical Engineering Science 58, (3-6): 711-718.

Li, J., and J.A.M. Kuipers. 2005. On the origin of heterogeneous structure in dense gas-solid flows. Chemical Engineering Science 60, (5): 1251-1265.

Li, Y., G.Q. Yang, J.P. Zhang, and L.-S Fan. 2001. Numerical studies of bubble formation dynamics in gas-liquid-solid fluidization at high pressures. Powder Technology 116, (2-3): 246-260.

Li, Y., J. Zhang, and L.-S Fan. 1999. Numerical simulation of gas-liquid-solid fluidization systems using a combined CFD-VOF-DPM method: Bubble wake behavior. Chemical Engineering Science 54, (21): 5101-5107.

Limtrakul, S., A. Boonsrirat, and T. Vatanatham. 2004. DEM modeling and simulation of a catalytic gas-solid fluidized bed reactor: A spouted bed as a case study. Chemical Engineering Science 59, (22-23): 5225-5231.

Link, J., C. Zeilstra, N. Deen, and H. Kuipers. 2004. Validation of a discrete particle model in a 2D spout-fluid bed using non-intrusive optical measuring techniques. Canadian Journal of Chemical Engineering 82, (1): 30-36.

Link, J.M., L.A. Cuypers, N.G. Deen and J.A.M. Kuipers. 2005. Flow regimes in a spout-fluid bed: a combined experimental and simulation study. Chemical Engineering Science 60, (13): 3425-3442.

Lun C.C.K., 2000. Numerical simulation of dilute turbulent gas-solid flows. International Journal of Multiphase Flow 26: 1707-1736.

Lun, C. K. K., Savage, S. B., Jeffrey, D. J., & Chepurniy, N. (1984). Kinetic theories for granular flow - inelastic particles in Couette-flow and slightly inelastic particles in a general flow field. *Journal of Fluid Mechanics, 140(MAR), 223-256*.

Lun, C. K. K., Savage, S. B., Jeffrey, D. J., & Chepurniy, N. (1984). Kinetic theories for granular flow - inelastic particles in Couette-flow and slightly inelastic particles in a general flowfield. Journal of Fluid Mechanics, 140(MAR), 223-256.

Luo, H. and Svendsen, H.F., 1996, Theoretical model for drop and bubble breakup in turbulent dispersions, *AIChE J*., 42, 1225-1233.

MacInnes, J.M., and Braco, F.V. (1992) Stochastic particle dispersion and the tracer particle limit. Phys. Fluids A 4: 2809.

McNamara, S., and W.R. Young. 1992. Inelastic collapse and clumping in a one-dimensional granular medium. Physics of Fluids, 4, (3): 496-504.

Menter, F. 2002. Best Practice Guidelines for CFD Code Validation for Reactor-Safety Applications, ECORA Cotract No. FIKS-CT-2001-00154, European Commission 5th Euratom Framework Programme 1998-2002.

Mikami, T., H. Kamiya, and M. Horio. 1998. Numerical simulation of cohesive powder behavior in a fluidized bed. Chemical Engineering Science 53, (10): 1927-1940.

Mittal, R. and Iaccarino, G. (2005). Immersed boundary methods, Annu. Rev. Fluid Mech., **37**, 239-61.

Mudde, R.F., and Simonin, O., 1999, Two and three dimensional simulations of a bubble plume using a two-fluid model, *Chem. Eng. Sci.*, 54, 5061-5069.

Noh, W.F. and Woodward, P.R. (1976), SLIC (Simple Line Interface Calculation) method, In : Lecture Notes in Physics, A.I. van de Vooren and P.J. Zandbergen (eds.), 330.

Oey, R.S., Mudde, R.F. and Van den Akker, H.E.A., 2003, Sensitivity study on interfacial closure laws in two-fluid bubbly flow simulations, *AIChE J.*, 49, 1621-1636.

Oey, R.S., Mudde, R.F., Portela, L.M., and Van den Akker, H.E.A., 2001, Simulation of a slurry air lift using a two-fluid model, *Chem. Eng. Sci.*, 56, 673-681.

Ouyang, J., and J. Li. 1999a. Particle-motion-resolved discrete model for simulating gas-solid fluidization. Chemical Engineering Science 54, (13-14): 2077-2083.

Ouyang, J., and J. Li. 1999b. Discrete simulations of heterogeneous structure and dynamic behavior in gas-solid fluidization. Chemical Engineering Science 54, (22): 5427-5440.

Pandit, J.K., X.S. Wang, and M.J. Rhodes. 2005. Study of Geldart's group A behaviour using the discrete element method simulation. Powder Technology 160, (1): 7-14.

Patankar, S.V., 1980, Numerical heat transfer and fluid flow, Hemisphere Publ. Corp.

Peskin, C.S. (1977), Numerical analysis of blood flow in the heart, J. Comp. Phys., **25**, 220-252.

Peskin, C.S. (2002). The immersed boundary method, Acta Numerica, **11**, 479-517.

Pope, S.B. (1994) Lagrangian PDF methods for turbulent flows. Annu. Rev. Fluid Mech., 26: 23.

Popinet, S. and Zaleski, S. (1999). A front-tracking algorithm for accurate representation of surface tension. Int J. Numer. Meth. Fluids, **30**, 775-793.

Prince, M.J. and Blanch, H.W., 1990, Bubble coalescence and break-up in air-sparged bubble columns, *AIChE J.*, 36, 1485-1499.

Pyle, D. L. and D. Harrison, 1967, The rising velocity of bubbles in two-dimensional fluidised beds. Chemical Engineering Science, 22, 531-535.

Ranade, V.V. and Tayalia, Y., 2001, Modeling of fluid dynamics and mixing in shallow bubble column reactors: influence of sparger design, *Chem. Eng. Sci.*, 56, 1667-1675.

Rider, W.J. and Kothe, D.B. (1995). Stretching and tearing interface tracking methods, presented at the 12th AIAA CFD Conference, June 20, 1995, San Diego. Available on World Wide Web at : http://laws.lanl.gov/XHM/personnel/wjr/Web_papers/pubs.html.

Rider, W.J. and Kothe, D.B. (1998). Reconstructing volume tracking, J. Comp. Phys., **141**, 112-152.

Ristow, G.H. 2000. Pattern Formation in Granular Materials. Springer-Verlag, New York.

Rudman, M. (1997). Volume-tracking methods for interfacial flow calculations, Int. J. Num. Methods in Fluids, **24**, 671-691.

Sani, R.L. and Gresho, P.M., 1994, Resume and remarks on the open boundary condition minisymposium, *Int. J. Numer. Meth.*, 18, 983-1008.

Sankaranarayanan, K. and Sundaresan, S. (2002b), Lift force in bubble suspensions, Chem. Eng. Sci. **57**, 3521-3542.

Sankaranarayanan, K., Shah, X., Kevrekidis, I.G. and Sundaresan, S. (2002a), Analysis of drag and added mass forces in bubbly suspensions using an implicit formulation of the lattice Boltzmann method, J. Fluid Mech., **452**, 61-96.

Sanyal, J., Marchisio, D.L., Fox, R.O., and Dhanasekharan, K., 2005, On the comparison between population balance models for CFD simulation of bubble columns, *Ind. Eng. Chem. Res.*, 44,5063-5072.

Sanyal, J., Vasquez, S., Roy, S. and Dudukovic, M.P., 1999, Numerical simulation of gas-liquid dynamics in cylindrical bubble column reactors, *Chem. Eng. Sci.*, 54, 5071-5083.

Sasic, S. (2005). Fluid Dynamics of Fluidized Bed Reactors: Experiments and Simulations with System Interactions. PhD Thesis, Chalmers University of Technology, Sweden.

Sato, Y., Sadatomi, M. and Sekoguchi, K., 1981, Momentum and heat transfer in two-phase bubble flow, *Int. J. Multiphase Flow*, 7, 167.

Savage, S. B. (1983). Granular Flows at High Shear Rates. Theory of Dispersed Multiphase Flow, Proceedings of an Advanced Seminar, Madison, WI, USA (pp. 339-358).

Scardovelli, S. and Zaleski, S. (1999). Direct numerical simulation of free-surface and interfacial flow, Annu. Rev. Fluid Dyn., **31**, 567-603.

Schäfer, J., S. Dippel, D.E. Wolf. 1996. Force schemes in simulations of granular materials, Journal de Physique I 6, (1): 5-20.

Schwarz, M.P. and Turner, W.J., 1988, Applicability of standard k-e turbulence model to gas stirred bath, *Appl. Math. Modeling*, 12, 273-279.

Sethian, J.A. (1996). Level Set Methods, Cambridge U.P., Cambridge, UK.

Simonin, O., 1990, Eulerian formulation for particle dispersion in turbulent two-phase flows, In Sommerfeld, M., ed., *Fifth Workshop on Two-Phase Flow Predictions*, Erlangen, Germany, p.156-166.

Sint Annaland van M., Deen N.G., Kuipers J.A.M. (2005). Numerical simulation of gas bubbles behaviour using a three-dimensional Volume of Fluid method, Chem. Eng. Sci. **60**, 2999-3011.

Slack, M.D., Prasad, R.O., Bakker, A., and Boysan, F. (2000) Advances in cyclone modelling using unstructured grids. Trans IChemE, 78A: 1098.

Sokolichin, A. and Eigenberger, G., 1999, Applicability of the standard k-e turbulence model to the dynamic simulation of bubble columns: Part I. Detailed numerical simulations, *Chem. Eng. Sci.*, 54, 2273.

Sokolichin, A., Eigenberger, G. and Lapin, A., 2004, Simulation of buoyancy driven bubbly flow: established simplifications and open questions, *AIChE J.*, 50, 24-45.

Sokolichin, A., Eigenberger, G., Lapin, A. and Lübbert, A., 1997, Dynamic numerical simulation of gas-liquid two-phase flows: Euler/Euler versus Euler/Lagrange, *Chem. Eng. Sci.*, 52, 611-626.

Sussman, M. and Fatemi, E. (1999). An efficient interface-preserving level set redistancing algorithm and its application to interfacial incompressible fluid flow, SIAM J. Sci. Comp., **20**, 1165-1191.

Sussman, M. and Smereka, P., Axi-symmetric free boundary problems, J. Fluid Mech., **341**, 269-294.

Sussman, M., Almgren, A.S., Bell, J.B., Colella, P., Howell, L.H. and Welcome, M.L. (1999). An adaptive level set approach for incompressible two-phase flows, J. Comp. Phys., **148**, 81-124.

Sussman, M., Smereka, P. and Osher, S. (1994). A level set approach for computing solutions to incompressible two-phase flow, J. Comp. Phys., **114**, 146-159.

Syamlal, M., Rogers, W., & O`Brien, T. J. (1993). MFIX documentation, theory guide. Morgantown, West Virginia, USA.

Tennekes, H., and Lumley, J.L. (1972) A first course in turbulence. The MIT Press, Cambridge.

Thomson, D.J. (1987) Criteria for the selection of stochastic models of particle trajectories in turbulent flows. J. Fluid Mech., 180: 529.

Tomiyama, A., Tamai, H., Zun, I. and Hosokawa, S., 2002, Transverse migration of single bubbles in simple shear flows, *Chem. Eng. Sci.*, 57,1849-1858.

Tsuji, Y., T. Kawaguchi, and T. Tanaka. 1993. Discrete particle simulation of two-dimensional fluidized bed. Powder Technology 77, (1): 79-87.

Uhlmann, M. (2005). An immersed boundary method with direct forcing for the simulation of particulate flows, J. Comp. Phys., **209**, 448-476.

Unverdi, S.O. and Tryggvason, G. (1992). A front-tracking method for viscous, incompressible multi-fluid flows. *J. Comp. Phys.* **100**, 25-37.

Van Baten, J.M., and Krishna, R., 2001, Eulerian simulations for determination of axial dispersion of liquid and gas phases in bubble columns operating in the churn-turbulent regime, *Chem. Eng. Sci.*, 56, 203.

Van den Akker, H.E.A., 1986, Momentum equations in dispersed two-phase flows, Chapter 15, 371-400, Gulf Publishing Company.

Van der Hoef, M.A., M. Van Sint Annaland, and J.A.M. Kuipers. 2005. Computational fluid dynamics for dense gas-solid fluidized beds: A multi-scale modeling strategy. China Particuology 3, (1-2): 69-77.

Van Sint Annaland, M., N.G. Deen, and J.A.M. Kuipers. 2005. Numerical simulation of gas-liquid-solid flows using a combined front tracking and discrete particle method. Chemical Engineering Science 60, (22): 6188-6198.

van Wachem, B. G. M., Schouten, J. C., Krishna, R., & van den Bleek, C. M. (1998). Eulerian Simulations of Bubbling Behaviour in Gas-Solid Fluidised Beds. Computers & Chemical Engineering, 22(1), S299-S306.

Van Wachem, B.G.M., J.C. Schouten, C.M. Van den Bleek, R. Krishna, and J.L. Sinclair. 2001. Comparative analysis of CFD models of dense gas-solid systems. AIChE Journal 47, (5): 1035-1051.

Vesvikar, M.S. and Al-Dahhan, M., 2005, Flow pattern visualization in a mimic anaerobic digester using CFD, Wiley Interscience, www.interscience.wiley.com.

Viollet, P.L. and Simonin, O., 1994, Modeling dispersed two-phase flows: closure, validation and software development, *Appl. Mech. Rev.*, 47, 80.

Vreman, A.W., M. Al-Tarazi, J.A.M. Kuipers, M. van Sint Annaland, and O. Bokhove. 2006. Rapid shallow granular and hydraulic flow through a contraction. Submitted to Journal of Fluid Mechanics.

Walton, O.R. and R.L. Braun. 1986. Viscosity and temperature calculations for assemblies of inelastic frictional disks. Journal of Rheology 30, (5): 949-980.

Welch, J.E., Harlow, F.H., Shannon, J.P. and Daly, B.J. (1965). The MAC method: a computing technique for solving viscous incompressible transient fluid flow problems involving free surfaces. Los Alamos Scientific Laboratory Report LA-3425.

Wen, C. Y., & Yu, Y. H. (1966). Mechanicss of Fluidization. Chemical Engineering Progress Symposium Series, 62, 100-111.

Wen, Y.C. and Yu, Y.H., 1966. Mechanics of Fluidization, Chemical Engineering Progress Symposium Series 62, 100-111.

Werther, J. and O. Molerus, 1973, The local structure of gas fluidized beds - II. The spatial distribution of bubbles. International Journal of Multiphase Flow, 1, 123-138.

Xu, B.H., A.B. Yu, S.J. Chew, and P. Zulli. 2000. Numerical simulation of the gas-solid flow in a bed with lateral gas blasting. Powder Technology 109, (1-3): 13-26.

Xu, B.H., and A.B. Yu. 1997. Numerical simulation of the gas-solid flow in a fluidized bed by combining discrete particle method with computational fluid dynamics. Chemical Engineering Science 52, (16): 2785-2809.

Ye, M., M.A. van der Hoef, and J.A.M. Kuipers. 2004. A numerical study of fluidization behavior of Geldart A particles using a discrete particle model. Powder Technology 139, (2): 129-139.

Ye, M., M.A. van der Hoef, and J.A.M. Kuipers. 2005. The effects of particle and gas properties on the fluidization of Geldart A particles. Chemical Engineering Science 60, (16): 4567-4580.

Yeoh, S.L., Papadakis, G., and Yianneskis, M. (2005) Determination of mixing time and degree of homogeneity in stirred vessels with large eddy simulation. Chem. Eng. Sc., 60: 2293.

Youngs, D.L. (1982). Time-dependent multi-material flow with large fluid distortion, In: *Numerical methods for fluid dynamics*, K.W. Morton and M.J. Bianes (Eds.), Academic Press, New York, 273-285.

Yu, A.B., and B.H. Xu. 2003. Particle-scale modelling of gas-solid flow in fluidisation. Journal of Chemical Technology and Biotechnology 78, (2-3): 111-121.

Zhang, D.Z. and Rauenzahn, R.M. (1997). A viscoelastic model for dense granular flows. J. Rheol., 41, 1275-1298.

Zhang, J., L.-S. Fan, C. Zhu, R. Pfeffer, D. Qi. 1999. Dynamic behavior of collision of elastic spheres in viscous fluids. Powder Technology 106, (1-2): 98-109.

Zhang, J., Y. Li, and L.-S Fan. 2000a. Numerical studies of bubble and particle dynamics in a three-phase fluidized bed at elevated pressures. Powder Technology 112, (1-2): 46-56.

Zhang, J., Y. Li, and L.-S Fan. 2000b. Discrete phase simulation of gas-liquid-solid fluidization systems: Single bubble rising behavior. Powder Technology 113, (3): 310-326.

Zhou, H., G. Flamant, D. Gauthier, and J. Lu. 2004. Numerical simulation of the turbulent gas-particle flow in a fluidized bed by an LES-DPM model. Chemical Engineering Research and Design, 82, (A7): 918-926.

Zhou, Q., and Leschziner, M.A. (1991) A time-correlated stochastic model for particle dispersion in anisotropic turbulence. 8th Symposium on Turbulent Shear Flows, TU Munich, 1: 1031.

Elghobashi (1994) Chapter 2

Basset, A.B. (1888) On the motion of a sphere in a viscous liquid. Phil. Trans. Roy. Soc., Vol. A179, 43-69

Bokkers, G. A., M. Van Sint Annaland, and J. A. M. Kuipers. 2004. Mixing and segregation in a bidisperse gas-solid fluidised bed: A numerical and experimental study. Powder Technology 140, (3): 176-186.

Bokkers, G.A. 2005. Multi-level Modeling of the Hydrodynamics in Gas Phase Polymerisation Reactors; PhD thesis University of Twente, Enschede.

Brereton, G. and Korotney, D. (1991). Coaxial and oblique coalescence of two rising bubbles, AMD- Vol. 119, Dynamics of Bubbles and Vortices Near a Free Surface. ASME.

Darmana, D., N.G. Deen and J.A.M. Kuipers. 2005. Detailed Modeling of Hydrodynamics, Mass transfer and Chemical Reactions in a Bubble Column using a Discrete Bubble Model. Chemical Engineering Science 60, (12): 3383-3404.

Deen, N.G., T. Solberg, and B.H. Hjertager. 2001. Large eddy simulation of the gas-liquid flow in a square cross-sectioned bubble column. Chemical Engineering Science 56, (21-22): 6341-6349.

Delnoij, E., F.A. Lammers, J.A.M. Kuipers and W.P.M. van Swaaij. 1997a. Dynamic simulation of dispersed gas-liquid two-phase flow using a discrete bubble model, Chemical Engineering Science 52, (9): 1429-1458.

Ergun S., 1952. Fluid Flow through Packed Columns. Chemical Engineering Progress 48, 89-94.

Goldschmidt, M.J.V., R. Beetstra, and J.A.M. Kuipers. 2004. Hydrodynamic modelling of dense gas-fluidised beds: Comparison and validation of 3D discrete particle and continuum models. Powder Technology 142, (1): 23-47.

Hill, R.J., D.L. Koch and J.C. Ladd. 2001. Moderate-Reynolds-numbers flows in ordered and random arrays of spheres. Journal of Fluid Mechanics 448: 243-278.

Van der Hoef, M.A., M. Van Sint Annaland, and J.A.M. Kuipers. 2005. Computational fluid dynamics for dense gas-solid fluidized beds: A multi-scale modeling strategy. China Particuology 3, (1-2): 69-77.

Wen, Y.C. and Yu, Y.H., 1966. Mechanics of Fluidization, Chemical Engineering Progress Symposium Series 62, 100-111.

Acknowledgements

This work was carried out with the highly appreciated contributions from Dr. Nico Deen, Prof. Jos Derksen, Dr. Muhamed Hadziabdic, Prof. Hans Kuipers, Dr. Christian Marchioli, Prof. Rob Mudde, Prof. Dirk Roekaerts and Prof. Alfredo Soldati. The contents were critically reviewed by Prof. Charles Hirsch, Dr. Chris Carey and Prof. Mick Casey. The editors express their gratitude to them all. A grant was obtained from The Swedish Industrial Association for Multiphase Flows, SIAMUF. The work was initiated on request of the late Prof. Rolf Karlsson, Vattenfall Utveckling.